

# The Effect of Wing Damage on Aeroelastic Behavior

by

Howard J. Conyers

Department of Mechanical Engineering and Materials Science  
Duke University

Date: \_\_\_\_\_

Approved:

---

Dr. Earl H. Dowell, Co-Chair

---

Dr. Kenneth C. Hall, Co-Chair

---

Dr. John E. Dolbow

---

Dr. Lawrence Virgin

---

Dr. Robert Kielb

---

Dr. Zbigniew J. Kabala

Dissertation submitted in partial fulfillment of the requirements for the degree of  
Doctor of Philosophy in the  
Department of Mechanical Engineering and Materials Science  
in the Graduate School of Duke University  
2009

ABSTRACT  
(Mechanical Engineering)

The Effect of Wing Damage on Aeroelastic Behavior

by

Howard J. Conyers

Department of Mechanical Engineering and Materials Science  
Duke University

Date: \_\_\_\_\_

Approved:

\_\_\_\_\_  
Dr. Earl H. Dowell, Co-Chair

\_\_\_\_\_  
Dr. Kenneth C. Hall, Co-Chair

\_\_\_\_\_  
Dr. John E. Dolbow

\_\_\_\_\_  
Dr. Lawrence Virgin

\_\_\_\_\_  
Dr. Robert Kielb

\_\_\_\_\_  
Dr. Zbigniew J. Kabala

An abstract of a dissertation submitted in partial fulfillment of the requirements for  
the degree of Doctor of Philosophy in the  
Department of Mechanical Engineering and Materials Science  
in the Graduate School of Duke University  
2009

Copyright © 2009 by Howard J. Conyers  
All rights reserved except the rights granted by the  
Creative Commons Attribution-Noncommercial Licence

# Abstract

Theoretical and experimental studies are conducted in the field of aeroelasticity. Specifically, two rectangular and one cropped delta wings with a hole are analyzed in this dissertation for their aeroelastic behavior.

The plate-like wings are modeled using the finite element method for the structural theory. Each wing is assumed to behave as a linearly elastic and isotropic, thin plate. These assumptions are those of small-deflection theory of bending which states that the plane sections initially normal to the midsurface remain plane and normal to that surface after bending. The wings are modeled in low speed flows according to potential flow theory. The potential flow is governed by the aerodynamic potential equation, a linear partial differential equation. The aerodynamic potential equation is solved using a distribution of doublets that relates pressure to downwash in the doublet lattice method. A hole in a wing-like structure is independently investigated theoretically and experimentally for its structural and aerodynamic behavior.

The aeroelastic model couples the structural and aerodynamic models using Lagrange's equations. The flutter boundary is predicted using the V-g method. Linear theoretical models are capable of predicting the critical flutter velocity and frequency as verified by wind tunnel tests. Along with flutter prediction, a brief survey on gust response and the addition of stores (missile or fuel tanks) are examined.

This dissertation is dedicated to my parents Hallie & Harrison Conyers and the late Dr. John Hope Franklin.

# Contents

Abstract	iv
List of Tables	ix
List of Figures	xi
List of Abbreviations and Symbols	xvi
Acknowledgements	xviii
Introduction	1
<b>1 Literature Review</b>	<b>4</b>
<b>2 Structural Dynamics</b>	<b>10</b>
2.1 Finite element modeling . . . . .	16
2.2 Preliminary studies: Validation of ANSYS <sup>TM</sup> . . . . .	18
2.2.1 Experimental setup for preliminary structural investigations . . . . .	21
2.3 Structural dynamics conclusions . . . . .	27
<b>3 Unsteady Aerodynamics</b>	<b>28</b>
3.1 Governing equations . . . . .	28
3.1.1 Aerodynamic potential equation and boundary conditions . . . . .	31
3.1.2 Pressure potential equation and the Kernel's function . . . . .	32
3.2 Doublet lattice method . . . . .	35
3.3 Results for the 2-d doublet lattice method . . . . .	38
3.4 Results for 3-d doublet lattice method . . . . .	39

3.5	Conclusions . . . . .	48
<b>4</b>	<b>Theoretical and Experimental Aerodynamic Studies of a Wing with Hole</b>	<b>50</b>
4.1	Aerodynamical theoretical modeling of a wing with a hole . . . . .	50
4.2	Aerodynamic experimental investigations of a wing with hole . . . . .	53
4.2.1	Experimental apparatus for a wing with hole . . . . .	53
4.2.2	Results from the wind tunnel investigations of wing with hole	54
4.3	Conclusions from the aerodynamic experiment and computation . . .	79
<b>5</b>	<b>Aeroelastic Studies of Wings with Holes, but without Stores</b>	<b>81</b>
5.1	Lagrange's equations and modal methods . . . . .	81
5.1.1	Polynomial curve fitting of the structural mode shape . . . . .	83
5.1.2	Aeroelastic model . . . . .	87
5.2	Cantilevered rectangular aeroelastic models . . . . .	89
5.2.1	Data acquisition for flutter experiments . . . . .	90
5.2.2	Aeroelastic rectangular wing model without a hole . . . . .	91
5.2.3	Aeroelastic rectangular models with a hole . . . . .	98
5.3	Aeroelastic rectangular wing models in a gust flow-field . . . . .	104
5.3.1	Experimental setup for gust generator . . . . .	104
5.3.2	Gust excited nonlinearities for rectangular wings with hole . .	105
5.4	Aeroelastic analysis of cropped delta wing with hole . . . . .	119
5.4.1	Cropped delta wing structure . . . . .	120
5.5	Conclusions from aeroelastic studies . . . . .	122
<b>6</b>	<b>Aeroelastic Studies of Wing-Store Configuration</b>	<b>124</b>
6.1	Modeling the wing-store structure . . . . .	125
6.1.1	Structural verification of wing-store model . . . . .	127
6.2	Slender body aerodynamics . . . . .	132

6.3	Aeroelastic behavior of wing-store combination . . . . .	133
6.3.1	Results from wing-store aeroelastic analysis . . . . .	134
6.4	Conclusions from wing-store analysis and experiment . . . . .	135
<b>7</b>	<b>Summary</b>	<b>136</b>
7.1	Conclusions . . . . .	136
7.2	Future Work . . . . .	137
<b>A</b>	<b>Appendix</b>	<b>140</b>
A.1	Aerodynamics of a wing with a hole . . . . .	140
A.2	Overview of aeroelastic analysis . . . . .	141
A.3	Sample ANSYS™ file . . . . .	144
A.4	The aeroelastic code in MatLab™ . . . . .	146
	<b>Bibliography</b>	<b>159</b>
	<b>Biography</b>	<b>164</b>

# List of Tables

2.1	The first five natural frequencies of the plate in Figure 2.6 with a hole near the root as determined by ANSYS™ and the experiment. The second torsion mode is not excited, see the text for more information regarding “*.” . . . . .	26
2.2	Comparison of experimental and ANSYS™ results of first four natural frequencies(in Hz) of the CDW with a hole of radius 0.0307 m at two x,y locations . . . . .	26
5.1	The first five natural frequencies(in Hz) of the cantilevered plate without a hole. Bend. and Tors. refer to the bending and torsion mode, respectfully. . . . .	91
5.2	The first five natural frequencies(in Hz) of the plate with the hole at the root and tip. Bend. and Tors. refer to the bending and torsion mode . . . . .	100
5.3	Theoretical and experimental flutter velocity and frequencies listed for various hole locations . . . . .	100
5.4	The first ten natural frequencies of the wing with a large hole as determined by ANSYS™ . . . . .	103
5.5	Theoretical flutter velocity and frequency for wing with hole size 25% of the total wing area . . . . .	103
5.6	The first seven natural frequencies as determined by ANSYS™ and the experiment for the cropped delta wing with and without a hole. . . .	121
6.1	Natural frequencies as determined by ANSYS™ and the experiment for the rectangular wing-store model with the hole near the tip. . . .	128
6.2	Natural frequencies as determined by ANSYS™ and the experiment for the rectangular wing-store model with the hole near the root. . . .	130

6.3	Natural frequencies as determined by ANSYS™ and the experiment for the cropped delta wing-store model with a hole. . . . .	132
6.4	Theoretical and experimental flutter velocity and frequencies . . . . .	134
6.5	Theoretical and experimental flutter velocity and frequencies . . . . .	135
6.6	Theoretical and experimental flutter velocity and frequencies . . . . .	135

# List of Figures

2.1	A typical free mesh of a plate with a hole in ANSYS™ with the fully clamped root . . . . .	17
2.2	Clamped rectangular plate having a centralized circular hole studied by Takahashi . . . . .	19
2.3	Plots of nondimensional frequency parameter $\frac{\omega^2 a^4 \rho}{D}$ as a function of hole size for a clamped rectangular plate. $D = Eh^3/12(1 - \nu^2)$ is the flexural rigidity of the plate . . . . .	20
2.4	Closeup view of shaker and accelerometer on model for vibration tests for determining the natural frequencies . . . . .	22
2.5	Equipment setup for vibration tests for determining the natural frequencies for the structural models . . . . .	23
2.6	Two cantilevered plate configurations . . . . .	25
3.1	General grid for the doublet lattice method . . . . .	40
3.2	$C_p$ on airfoil with oscillating flap in incompressible flow, $k=1.0$ . . . .	40
3.3	Plots of lift for $n$ panels on airfoil due to plunging motion as $k$ varies from 0.01 to 2.61 in increments of .1 . . . . .	41
3.4	Plot of lift for $n$ panels on airfoil due to gust response as $k$ varies from 0.01 to 2.61 in increments of 0.1 . . . . .	42
3.5	Coefficient of lift vs number of boxes for a wing $AR=1$ and also wing aspect ratio . . . . .	43
3.6	Geometry with Prandtl Glaurent transformation on swept wing in steady flow( $k=0$ ) . . . . .	44
3.7	Lift distribution on swept wing in Fig. 3.6 in steady flow( $k=0$ ) . . . .	45

3.8	Lift distribution on rectangular wing(AR=3) oscillating in bending mode in compressible( $M = 0.24$ ) and unsteady( $k = 0.47$ ) flow . . . .	47
4.1	SolidWorks™ of wing model with the pressure ports. The chord is 12 inches and span is 9.6 inches. . . . .	55
4.2	The magnitude of the theoretical and experimental $\Delta C_p$ versus chord-wise position, $x/c$ , at $y/s = 0.458$ . $\alpha = 0^\circ$ . . . . .	56
4.3	The magnitude of the theoretical and experimental $\Delta C_p$ versus chord-wise position, $x/c$ , at $y/s = 0.458$ . $\alpha = 2^\circ$ . . . . .	57
4.4	The magnitude of the theoretical and experimental $\Delta C_p$ versus chord-wise position, $x/c$ , at $y/s = 0.458$ . $\alpha = 5^\circ$ . . . . .	58
4.5	The magnitude of the theoretical and experimental $\Delta C_p$ versus chord-wise position, $x/c$ , at $y/s = 0.458$ . $\alpha = 8^\circ$ . . . . .	59
4.6	The magnitude of the theoretical and experimental $\Delta C_p$ versus chord-wise position, $x/c$ , at $y/s = 0.458$ . $\alpha = 10^\circ$ . . . . .	60
4.7	The magnitude of the theoretical and experimental $\Delta C_p$ versus chord-wise position, $x/c$ , at $y/s = 0.125$ . $\alpha = 0^\circ$ . . . . .	61
4.8	The magnitude of the theoretical and experimental $\Delta C_p$ versus chord-wise position, $x/c$ , at $y/s = 0.125$ . $\alpha = 2^\circ$ . . . . .	62
4.9	The magnitude of the theoretical and experimental $\Delta C_p$ versus chord-wise position, $x/c$ , at $y/s = 0.125$ . $\alpha = 5^\circ$ . . . . .	63
4.10	The magnitude of the theoretical and experimental $\Delta C_p$ versus chord-wise position, $x/c$ , at $y/s = 0.125$ . $\alpha = 8^\circ$ . . . . .	65
4.11	The magnitude of the theoretical and experimental $\Delta C_p$ versus chord-wise position, $x/c$ , at $y/s = 0.125$ . $\alpha = 10^\circ$ . . . . .	66
4.12	The magnitude of the theoretical and experimental $\Delta C_p$ versus span-wise position, $y/s$ , at $U_\infty=0$ m/s and $x/c = 0.1625$ . $\alpha = 0^\circ$ . . . . .	67
4.13	The magnitude of the theoretical and experimental $\Delta C_p$ versus span-wise position, $y/s$ , at $x/c = 0.1625$ . $\alpha = 0^\circ$ . . . . .	68
4.14	The magnitude of the theoretical and experimental $\Delta C_p$ versus span-wise position, $y/s$ , at $x/c = 0.1625$ . $\alpha = 2^\circ$ . . . . .	69
4.15	The magnitude of the theoretical and experimental $\Delta C_p$ versus span-wise position, $y/s$ , at $x/c = 0.1625$ . $\alpha = 5^\circ$ . . . . .	70

4.16	The magnitude of the theoretical and experimental $\Delta C_p$ versus spanwise position, $y/s$ , at $x/c = 0.1625$ . $\alpha = 8^\circ$ . . . . .	71
4.17	The magnitude of the theoretical and experimental $\Delta C_p$ versus spanwise position, $y/s$ , at $x/c = 0.1625$ . $\alpha = 10^\circ$ . . . . .	72
4.18	The magnitude of the theoretical and experimental $\Delta C_p$ versus spanwise position, $y/s$ , at $U_\infty = 0m/s$ versus spanwise position at $x/c = 0.4625$ . $\alpha = 0^\circ$ . . . . .	73
4.19	The magnitude of the theoretical and experimental $\Delta C_p$ versus spanwise position, $y/s$ , at $x/c = 0.4625$ . $\alpha = 0^\circ$ . . . . .	74
4.20	The magnitude of the theoretical and experimental $\Delta C_p$ versus spanwise position, $y/s$ , at $x/c = 0.4625$ . $\alpha = 2^\circ$ . . . . .	75
4.21	The magnitude of the theoretical and experimental $\Delta C_p$ versus spanwise position, $y/s$ , at $x/c = 0.4625$ . $\alpha = 5^\circ$ . . . . .	76
4.22	The magnitude of the theoretical and experimental $\Delta C_p$ versus spanwise position, $y/s$ , at $x/c = 0.4625$ . $\alpha = 8^\circ$ . . . . .	77
4.23	The magnitude of the theoretical and experimental $\Delta C_p$ versus spanwise position, $y/s$ , at $x/c = 0.4625$ . $\alpha = 10^\circ$ . . . . .	78
5.1	Comparison of fundamental mode to polynomial fit . . . . .	86
5.2	Damping vs. Flow Velocity for cantilevered rectangular wing without a hole . . . . .	93
5.3	Frequency vs. Flow Velocity for cantilevered rectangular wing without a hole . . . . .	94
5.4	Frequency vs. Damping for cantilevered rectangular wing without a hole . . . . .	95
5.5	FFT analysis of flutter acceleration response measured on the trailing edge for a cantilevered rectangular wing without a hole . . . . .	96
5.6	Correlation of Frequency vs Velocity between theory and experiment for the first torsional mode for the cantilevered rectangular wing without a hole . . . . .	97
5.7	Dimensional drawing of rectangular wing with hole near root . . . . .	98
5.8	Dimensional drawing of rectangular wing with hole near tip . . . . .	99

5.9	Clamped rectangular wing having a hole 25% of the total wing area at a distance of $\delta=0.020$ m, from root to the base of the rectangular hole . . . . .	102
5.10	LCO amplitudes and frequency vs flow velocity for Model A with hole near root( $\delta_1=0.057$ m) . . . . .	107
5.11	Plots of time series and FFT's of gust dominated motion for Model A with hole near root( $\delta_1=0.057$ m) for $U=24.80$ m/s and $\omega_g=13.02$ Hz	108
5.12	Plots of time series and FFT's of chaotic motion for Model A with hole near root( $\delta_1=0.057$ m) for $U=24.80$ m/s and $\omega_g=10.94$ Hz . . .	109
5.13	Plots of time series and FFT's of chaotic motion for Model A with hole near root( $\delta_1=0.057$ m) for $U=24.80$ m/s and $\omega_g=5.77$ Hz . . .	110
5.14	Plots of time series and FFT's of chaotic motion for Model B with hole near tip( $\delta_2=0.152$ m) for $U=24.85$ m/s and $\omega_g=10.95$ Hz . . . .	111
5.15	Plots of time series and FFT's of chaotic motion for Model B with hole near tip( $\delta_2=0.152$ m) for $U=24.85$ m/s and $\omega_g=5.69$ Hz . . . .	112
5.16	Plots of time series and FFT's of chaotic motion for Model B with hole near tip( $\delta_2=0.152$ m) for $U=24.80$ m/s and $\omega_g=3.04$ Hz . . . .	113
5.17	Plots of time series and FFT's of chaotic motion for Model B with hole near tip( $\delta_2=0.152$ m) for $U=24.80$ m/s and $\omega_g=6.04$ Hz . . . .	114
5.18	Plots of time series and FFT's of chaotic motion for Model B with hole near tip( $\delta_2=0.152$ m) for $U=24.80$ m/s and $\omega_g=9.02$ Hz . . . .	115
5.19	Plots of time series and FFT's of chaotic motion for Model B with hole near tip( $\delta_2=0.152$ m) for $U=26.52$ m/s and $\omega_g=3.04$ Hz . . . .	116
5.20	Plots of time series and FFT's of chaotic motion for Model B with hole near tip( $\delta_2=0.152$ m) for $U=26.52$ m/s and $\omega_g=6.04$ Hz . . . .	117
5.21	Plots of time series and FFT's of chaotic motion for Model B with hole near tip( $\delta_2=0.152$ m) for $U=26.52$ m/s and $\omega_g=9.02$ Hz . . . .	118
5.22	Nondimensional representation of the cropped delta wing . . . . .	121
6.1	Physical dimensions of store in the aeroelastic models . . . . .	125
6.2	The experimental and theoretical representation of the wing-store model . . . . .	126
6.3	Cantilevered rectangular wing-store model with hole near tip . . . . .	129

6.4	Cantilevered rectangular wing-store model with hole near root . . . .	131
A.1	Flowchart of flutter code . . . . .	142
A.2	Flowchart of flutter code with an emphasis on the aeroelastic portion	143

# List of Abbreviations and Symbols

$\gamma_{xz}, \gamma_{yz}$	vertical shear strains
$\epsilon_x, \epsilon_y, \epsilon_z$	normal strains in the x, y, and z directions
$\sigma_z$	normal stress
$\gamma_{xy}$	shear strain in the xy plane
$\tau_{xy}$	shear stress in the xy plane
$\nu$	Poisson's ratio
$G$	shear modulus
$E$	modulus of elasticity
$\delta$	virtual operator
$U$	strain energy
$W$	external work
$\Phi$	surface tractions or velocity potential
$\rho$	air density
$\rho_s$	structure density
$d$	displacement for nodal degrees of freedom
$N$	shape functions
$r^{int}, r^{ext}$	internal and external loads
$I, J, K, L$	motion nodes
$s, t$	local coordinates
$B$	strain displacement matrix

$[m], [k]$	mass and stiffness matrix, respectively
$\lambda$	eigenvalue
$\omega$	circular frequency
$\nabla$	del operator
$\mathbf{n}$	unit normal
F	boundary of wing
$\eta$	out of plane structural deformations
$U_\infty$	free stream velocity
$w/U_\infty$	nondimensional wash
$\bar{w}$	complex amplitude of nondimensional downwash
$\bar{p}$	complex lifting pressure coefficient
$\alpha$	angle of attack
K	complex acceleration potential kernel
b	semichord
$k = \omega b/U_\infty$	nondimensional frequency
$\bar{p} = p/((1/2)\rho U_\infty^2)$	coefficient of pressure
M	Mach number
$q_i$	generalized coordinates
$Q_i$	generalized forces
$\omega_g$	gust frequency
$\omega_f$	flutter frequency
$R_{x_{chord}} = U_\infty x_{chord}/\nu$	chord based Reynolds number
RSC	Rotating slotted cylinder

# Acknowledgements

First of all, I want to thank God for allowing me to navigate through the PhD process. I wish to express my sincere gratitude to my advisers, Dr. Earl Dowell and Dr. Kenneth Hall. Without your supervision and guidance, I would not have been able to matriculate through this humbling process.

Dr. Dowell, thank you for showing a genuine interest in me from the beginning. I can remember my first visit like yesterday, when you requested to see a list of textbooks used at my undergraduate institution. Dr. Hall, it has been a pleasure to work with you as a co-chair for my dissertation research. Your computational expertise and knowledge were invaluable in thoroughly understanding the doublet lattice method. It has been a honor and privilege to work with you both and I am forever grateful for your time.

Along with my advisers, I would like to thank my committee members Drs. John Dolbow, Lawrence Virgin, Robert Kielb, and Zbigniew Kabala for their comments and suggestions. I would be remiss if I did not thank Dr. Deman Tang, Dr. Edward Shaughnessy, Justin Jaworski, Chad Custer, John Goodfellow, Kathy Parrish, and Ivan Wang.

I would like to thank my parents Harrison and Hallie Conyers, my brother Harrison Jr, and my girlfriend Kathryn Jackson for their support. I would like to thank Dr. John Hope Franklin for sharing his time and wisdom. The MEMS department at Duke, I will forever be indebted to you for the financial support.

# Introduction

Aeroelasticity is the study of phenomena arise due to the interaction among aerodynamic, inertial, and elastic forces[1, 2]. Aeroelasticity is of primary interest in aeronautics and space engineering but it is of growing interest in civil and naval engineering applications [1]. The earliest known aeroelastic problems occurred in the early 1900's [2]. The problems in aeroelasticity were of major concern after World War II since aircraft design advanced rapidly as militaries around the world were trying to gain an advantage over one another [2]. Today, as military and civilian aircraft are constantly pushing the flight envelope, more aeroelastic issues are uncovered. An area in aeroelasticity with sparse information is the impact of damage on aeroelastic phenomena. In 2009, two commercial planes have crashed, one due to bird strike and the other due to icing. Although the exact cause has not been determined on each crash, bird strike [3] and icing [4] have been studied by aeroelasticians to the determined aeroelastic response due to damage on lifting surfaces. In this dissertation, the aeroelastic effects of a wing with a hole caused by missile or bird damage will be explored by theory and experiment to assess the structural dynamics, the unsteady aerodynamics, and the aeroelastic response. The ultimate goal of this dissertation is to show that aeroelastic theoretical models can be created that correlate well with experimental wind tunnel models for damaged wings.

The inertial and elastic forces are found from modeling the wing structural behavior. The structural theory used in this dissertation is the finite element method.

ANSYS™, a commercial finite element software, uses the Rayleigh-Ritz Method to determine the structural behavior of the wing. The wing is assumed to behave as a thin, elastic plate. Calculations performed using the finite element method correlate well with experimental models for a wing of uniform thickness that behaves as a thin, elastic isotropic plate.

The aerodynamic theory used in this dissertation is developed according to potential flow theory for unsteady compressible potential flow. The governing equation for incompressible steady potential flow is Laplace's Equation, a linear partial differential equation. In previous works by Attar, Tang, et. al[5, 6, 7, 8], Laplace's equation has been solved using a distribution of vortices in the vortex lattice method. In this dissertation, doublets replace the vortices in the doublet lattice method as developed by Albano and Rodden in the 1960's to solve the aerodynamic potential equation[9]. The aerodynamic potential equation governs unsteady compressible potential flow. The aerodynamic modeling of a wing with a hole is also explored experimentally to validate the theory.

The aeroelastic studies are conducted using the equations of motion derived from Lagrange's equations. Lagrange's equations describe complex dynamical systems in a relatively simple manner and couple the structural forces with the aerodynamics forces. The computational meshes used to calculate the structural behavior and the aerodynamic loadings are different; the matching of the structural and aerodynamic geometry can be achieved by various techniques. Here, a least square polynomial curve fitting technique is applied to the natural modes from the finite element model to determine the coefficients for a higher order polynomial to represent the deflection anywhere on the wing in a given mode,  $z = f(x, y)$ . Using the coefficients for the polynomial, the structural computational mesh can be matched to the aerodynamic mesh. Computing the aerodynamic forces requires knowing the wing's downwash. The wing's downwash has contributions from the deflection and from the slope of the

deflection of the wing. These contributions are calculated using the natural modes of the structure. The local structural slope term in the downwash is determined by analytically evaluating the polynomial equation for the deflection at any point location,  $x, y$ . After the aeroelastic equations have been formulated with Lagrange's equation, flutter calculations are done using the V-g method which is widely accepted in practice.

Aeroelastic studies are conducted on two primary configurations with holes in this dissertation, a low aspect ratio rectangular wing and a cropped delta wing. The rectangular wing has been designed and tested with different size holes in more than one location. Using the insight gained from the rectangular wing, only one configuration for the cropped delta wing with a hole is analyzed.

# 1

## Literature Review

Limited work has been done over the years on the effect of ballistic damage on aeroelastic response of lifting surfaces. A comprehensive study that investigates the major areas of aeroelasticity on battle damaged wings, experimentally and theoretically, has yet to appear in the unclassified literature. For many years a fighter aircraft, the F-16, with its cropped delta wing configuration has exhibited various aeroelastic characteristics that has peaked the interest of researchers. However, what is less investigated in the literature, but important, is the impact a damaged wing has on aeroelastic response including the effects of hole location, size of hole, and gust excitation. The purpose of this dissertation is to understand how damaged wings may respond aeroelastically using theory and then validating those findings in wind tunnel testing.

Flutter and limit cycle oscillations(LCO) are two aeroelastic phenomena that have been studied for many years on undamaged wings in various flow regimes. Flutter is usually investigated first because it is predicted using linear methods, whereas LCO prediction requires the use of nonlinear methods. Tang, Dowell, and Hall examined LCO on a cantilevered wing in subsonic flow using a nonlinear aeroelastic model [10].

One source of LCO on the F-16 and other high performance aircraft is the addition of stores. Stores are missiles, fuel tanks, and nacelles. Experimentally, flutter and LCO have been previously studied for a delta wing with stores by Dowell et. al [5, 6, 7, 8, 11, 12] and a cropped delta wing without stores by Gordnier [13]. Denegri and colleagues have measured flutter and LCO on various editions of the actual F-16 aircraft during flight tests for different external store configurations [14, 15, 16]. The configuration of stores change depending on the mission flown by the fighter craft and therefore in turn changes the onset of LCO. The stores typically (but not always) cause LCO to occur at lower flow velocities than for a wing without stores. Denegri and et. al have reported that linear aeroelastic models are capable of determining the flutter boundary and the onset of LCO except for the LCO amplitude [14, 15, 17, 16]. The onset of flutter on actual F-16's have been predicted using linear models [14, 15] and neural networks [17, 18]. Store connections to the wing can also trigger LCO, as reported in freeplay studies [11, 12]. As the research of LCO and flutter increased, Bunton and Denegri attempted to clear up the terminology in the aeroleastic community [15].

In earlier aeroelastic studies, Tang, Attar, and Dowell used nonlinear von Karman Plate Theory for the structural modeling of a delta wing [7]. Later, Attar, Dowell, and White used finite elements to model the structure of the delta wing [5] and the correlation between theory and experiment for aeroelastic studies was improved. In Attar [5] et. al the structural modeling was done using ANSYS™, a commercial finite element code [5]. The ANSYS™ software uses the Rayleigh Ritz Method to formulate the equations of motion. As a result of the work by Attar et. al, ANSYS™ was identified as a possible tool for modeling damage as a hole in a plate-like structure for this dissertation. Leissa reported in the late 1960's that Takahashi determined the natural frequencies of a clamped or simply supported plate on all edges with a cutout or hole [19]. Leissa's report on Takahashi's findings is an early structural example where theory is compared to experiment for a plate with hole. ANSYS™ is used to

verify Takahashi's results in part to determine if it is suitable to determine a wing with a hole. Takahashi used a Rayleigh Ritz method for the theoretical modeling, but it is slightly different in development than ANSYS™.

Ballistic damage changes the structural mass and stiffness, and the aerodynamic forces associated with a lifting surface, therefore changing its aeroelastic response. The first and most comprehensive study on the impact of ballistic damage on aeroelastic response was conducted by Biot and Arnold in 1950 [20] as reported by Dr. Ronald Stearman [21]. Dr. Stearman led a group of researchers at the University of Texas-Austin about 30 years later into this relatively untouched field. Besides what is initially reported by Stearman, little is known about the lost report by Biot and Arnold. According to Stearman, Biot and Arnold report that the flutter speed can increase due to asymmetrical damage in some instances [21]. Biot and Arnold also reported a structural failure is normally due to a loss of stiffness which will occur before aeroelastic instabilities. As a result, further research in this area was not pursued until Stearman [21] entered the area. Unfortunately, without Stearman's account on the work of Biot and Arnold, their contributions to the field of damaged induced flutter would be totally lost.

The majority of the published materials from Stearman's group focused on the instrumentation used in signal detection of damaged wings, but there were also a few studies on the aerodynamics of through-hole type damage. David Scott did a master's thesis in 1979 at the University of Texas-Austin under Stearman that looked at potential flow modeling of a through-hole type damage in a lifting surface utilizing the National Aeronautics and Space Administration(NASA) trisomic kernel function method[22]. Scott examined the aerodynamic change associated with a hole size of approximately 1% of the total wing area and noted that the NASA trisomic kernel function could not handle the aerodynamics associated with hole damage with great confidence. Scott recommended using the doublet lattice method for modeling such

a problem, since it will provide more insight of the near-field effects of a hole[22]. Scott master's thesis is perhaps the only theoretical investigation of aerodynamic modeling of a wing with hole. Subsequent studies only measured the aerodynamic loadings on the damaged wings during wind tunnel testing, without any theoretical computations to compare. This dissertation will evaluate the effectiveness of theory to model the flow over an experimental model for a wing with hole.

In 1980, Stearman found increased levels of localized drag due to damage [23, 21]. He discovered drag as a potential source of drag divergence, another aeroelastic phenomenon, in maneuvering flight conditions [23, 21]. In a non-maneuvering flight condition, parametric and combination resonances can also occur on a wing structure. Chen and Spearman reported in 1982 that damaged lifting surfaces found free from flutter and divergence are susceptible to resonance phenomenon caused by periodic air loads [21]. Further, the resonance phenomenon can promote lifting surface failure even when the structural damage is minimal. Broadly related to this problem is the addition of ice on a wing which causes periodic air loading. Kruger, Endruhan, and Stearman considered iced accumulation while looking at the galloping problem [4]. During the same era, NASA published some experimental findings on the aerodynamic effect of hole location caused by ballistic damage during certain flight conditions and its effect on aircraft and pilot survival [24]. NASA reported that damaging the major parts of the horizontal or vertical tail will likely cause catastrophic damage at some speeds [24]. Further, NASA stated that the removal of one panel on a wing will not likely cause the loss of the airplane or the pilot from an aerodynamic point of view [24].

The Australian Department of Defense realized the importance of understanding the changing aerodynamics due to damage in 1998 [25] in conducting its own literature survey on the subject. The literature found by Erm [25] was scarce. The majority of the works found by Erm reported data from wind tunnel explorations

due to control surface damage.

Broadly related were experimental investigations that evaluated the effect of ballistic damage on the aerodynamics of helicopter rotor airfoils [26], the effect of the shape of the hole used to simulate damage [27], as well as the crack-induced effects on aeroelasticity of unswept composite wings [28]. Robinson and Leishman explored the effect of various shape holes on helicopter rotor airfoils in 1998 and observed how little the aerodynamics forces changed at low angles of attack until the stall angle of attack was approached [26]. In 2007, Render and et. al did an extensive experimental investigation of an airfoil to determine if a circular shaped hole could reasonably simulate the aerodynamics of a star shaped hole which is a more realistic description of battle damage [27]. Render showed that variations in the geometric details of the hole area did little to change the aerodynamic loadings [27]. Also in 2007, Wang and Inman investigated the fracture of composite wings used on unmanned aerial vehicles, i.e. the Predator, because many surface cracks were forming near the wing root [28]. Similar to the findings of Biot and Arnold [20], Wang and Inman noted that the flutter or divergence speed is more sensitive to the stiffness changes than to the crack itself. The monitoring of a crack could be vital to the assessment of aeroelastic stability of the wing in structural health monitoring, especially in a case where the flutter speed has not yet dropped.

Still, little published literature is available on damaged, aeroelastic lifting surfaces such as the rectangular wing or cropped delta wing. Therefore the methods often used for determining the aeroelastic characteristics on undamaged wings will be used as a guide for solving the damaged wing problem with modifications. Previous work by Dowell, Attar, Tang, and et. al have used the vortex lattice method for calculating the aerodynamic loading in their aeroelastic analyses [5, 6, 7, 8, 10]. However, for the damaged wing the doublet lattice method by Rodden and Albano[29] is more suitable for determining loads on surfaces with holes than the vortex lattice method based

upon its formulation. Further, the doublet lattice method is the industry standard for determining the aerodynamic loading for flutter clearance when using classical linear aerodynamic models [30].

## 2

# Structural Dynamics

The lifting surface(fixed wing) in this dissertation is modeled as a thin, elastic plate. An elastic plate is a structure with infinite degrees of freedom, where these degrees of freedom are the displacements at every material point. Therefore the motion is characterized by partial differential equations(PDE). Partial differential equations are difficult to solve exactly except for the simplest of problems. The stress or displacement fields that solve the PDE and satisfy the boundary conditions exactly are nearly impossible to find. Another approach to solving the problem numerically is to use functionals. “A functional is an integral expression that implicitly contains the differential equations that describe the problem” according to Cook [31]. In this work, the Rayleigh-Ritz Method is applied to a functional that describes the model, thereby replacing the differential equations. Once the Rayleigh-Ritz Method is applied to the functional, it no longer contains integrals. The “transformed” functional is simply a function with a *finite* number of degrees of freedom. The Rayleigh-Ritz Method solves a similar problem with algebraic equations with a finite number of degrees of freedom instead of differential equations. Functionals are available for a potential energy expression in structural mechanics, acoustic modes in cavities, and

heat conduction. The Rayleigh-Ritz solution is rarely exact but it is more accurate as the degrees of freedom are increased. Today, the Rayleigh-Ritz Method is often the basis for the finite element method. The finite element method is applied using ANSYS™, the commercial finite element software.

The plate-like structure is assumed to be linearly elastic and isotropic. Ugral states these assumptions are categorized as the small-deflection theory of bending, classical theory, or the Kirchoff hypothesis [32]. According to this theory, the “plane sections initially normal to the midsurface remain plane and normal to that surface after bending [32].” Therefore, the vertical shear strains  $\gamma_{xz}$  and  $\gamma_{yz}$  are negligible.

$$\epsilon_x = \frac{1}{E} [\sigma_x - \nu(\sigma_y)] \quad (2.1)$$

$$\epsilon_y = \frac{1}{E} [\sigma_y - \nu(\sigma_x)] \quad (2.2)$$

$$\gamma_{xy} = \frac{\tau_{xy}}{G} \quad (2.3)$$

$$G = \frac{E}{2(1 + \nu)} \quad (2.4)$$

Here  $\epsilon_x$  and  $\epsilon_y$  are the normal strains in the x and y directions, respectively,  $\gamma_{xy}$  is the shear strain in the xy plane,  $\sigma_x$  and  $\sigma_y$  are the normal stresses in the x and y direction,  $\tau_{xy}$  is shear stress in the xy plane,  $\nu$  is Poisson’s ratio for the material, E is the Modulus of Elasticity, and G is the Shear Modulus.

The finite element method uses the Principle of Virtual Work to derive the structural model. The Principle of Virtual Work states that the change of the strain energy

due to the virtual displacement is equal to the change in external virtual work due to applied forces such as body loads, inertial forces, and surface tractions [32].

$$\delta U = \delta W \quad (2.5)$$

$$\delta U = \int \{\delta\epsilon\}^T \{\sigma\} dV \quad (2.6)$$

$$\delta W = \int (\{\delta u\}^T \{F\} + \{\delta u\}^T \rho \{\ddot{u}\})dV + \int \{\delta u\}^T \{\Phi\} dS \quad (2.7)$$

$$\{u\} = [N] \{d\}, \{\ddot{u}\} = [N] \{\ddot{d}\} \quad (2.8)$$

The above equations represent the Principle of Virtual Work on the element level used in the finite element method, where  $\delta$  is the virtual operator,  $U$  is the strain energy,  $W$  is the external work,  $\{u\}$  is the displacement vector,  $F$  is the body forces vector,  $\Phi$  is the matrix of surface tractions, and  $\rho$  is the density. The displacement vector( $u$ ) is composed of nodal displacement( $d$ ), and shape functions( $N$ ). The nodal displacement is the nodal degree of freedom. The shape function is a function of position.

In ANSYS<sup>TM</sup>, the shape functions vary with the type of element model used. Element SHELL63 is a 4-node quadrilateral shell element used extensively to model the uniform plate used for the lifting surface. Element SHELL63 assumes there is no buckling and that the structure does not change shape except for rigid body motion. SHELL63 can translate and rotate in the x, y, and z directions and axes, respectively, therefore exhibiting 6 degrees of freedom at each node as defined by the

ANSYS™ User Manual [33]. The shape functions for the inplane motions in the x and y directions are represented in Eqns. 2.9 and 2.10.

$$u = \frac{1}{4}(u_I(1-s)(1-t) + u_J(1+s)(1-t) + u_K(1+s)(1+t) + u_L(1-s)(1+t)) + u_1(1-s^2) + u_2(1-t^2) \quad (2.9)$$

$$v = \frac{1}{4}(v_I(1-s)(1-t) + v_J(1+s)(1-t) + v_K(1+s)(1+t) + v_L(1-s)(1+t)) + v_1(1-s^2) + v_2(1-t^2) \quad (2.10)$$

$$w \text{ Uses four overlaid triangles as a part of Discrete Kirchoff Elements} \quad (2.11)$$

where the subscripts  $I$ ,  $J$ ,  $K$ , and  $L$  refer to the motion at the node and the numerical subscripts refer to the extra shape functions. “The local coordinates  $s$  and  $t$  go from -1.0 on one side of the element to 1.0 on the other side in the x and y direction respectively, and are not necessarily orthogonal to one another [33].”

The shape function in Eqn. 2.11 for the out of plane motion in the z-direction that is of particular interest is not explicitly explained in the ANSYS™ code documentation [33]. The z-direction shape functions for the triangles are modeled using a Discrete Kirchoff Element (DKT). The critical part of the DKT element is the idea that there is zero transverse shear strain at specific points. For the formal development of the DKT, see Cook [31].

Combining Eqns. 2.5-2.8, the following expressions are derived

$$\begin{aligned} \{\delta d\}^T & \left[ \int [B]^T \{\sigma\} dV - \int [N]^T \{F\} dV - \int [N]^T \rho [N] dV \{\ddot{d}\} - \int [N]^T \Phi dS \right] \\ & = 0 \end{aligned} \tag{2.12}$$

$$[m] \{\ddot{d}\} + \{r^{int}\} = \{r^{ext}\} \tag{2.13}$$

$$[m] = \int [N]^T \rho [N] dV \tag{2.14}$$

$$\{r^{int}\} = \int [B]^T \{\sigma\} dV \tag{2.15}$$

$$\{r^{ext}\} = \int [N]^T \{F\} dV + \int [N]^T \Phi dS \tag{2.16}$$

where  $\{\delta d\}^T$  is a function of time and is arbitrary. Therefore time can be factored out in solving the problem. Also,  $\{r^{int}\}$  is the internal load vector,  $\{r^{ext}\}$  is the external load vector, and  $[B]$  is the strain-displacement matrix. The external loadings are neglected for understanding the structural model. However, the external loadings in this dissertation are due to the aerodynamic forces developed later.

Since the plate material is linear and elastic, the internal load vector is used to find the stiffness matrix,  $[k]$ . In linear, elastic materials the stress-displacement behavior is defined as  $\{\sigma\} = [E][B]\{d\}$ . This property allows the internal load vector to be

redefined as  $\{r^{int}\} = [k] \{d\}$ . Through the combinations of these expressions, the stiffness matrix is defined and then the dynamic equations are defined in the usual form below.

$$[k] = \int [B]^T [E] [B] dV \quad (2.17)$$

$$[m] \{\ddot{d}\} + [k] \{d\} = \{r^{ext}\} \quad (2.18)$$

These second order, ordinary differential equations (ODEs) in time are coupled. The ODEs are coupled since the nodal displacement vector ( $\{d\}$ ) is a function of space and time. Solving Eqn. 2.18 can be achieved using various numerical methods. Equation 2.18 is solved in the absence of external loading ( $r^{ext} = 0$ ) and by assuming the structure undergoes harmonic motion. Every degree of freedom moves in phase with all other degrees of freedom, so  $\{d\} = \{\bar{d}\} \sin(\omega t)$  and  $\{\ddot{d}\} = -\omega^2 \{\bar{d}\} \sin(\omega t)$ . The nodal degrees of freedom vibration amplitudes and the circular frequency in radians per second are represented by  $\{\bar{d}\}$  and  $\omega$ , respectively. Using the fact that each degree of freedom undergoes harmonic motion, the Classical Eigenvalue Problem can be written as:

$$([k] - \lambda [m]) \{\bar{d}\} = \{0\}, \lambda = \omega^2 \quad (2.19)$$

$$\det([k] - \lambda [m]) \quad (2.20)$$

where  $\lambda$  is the eigenvalue. The non trivial solutions are of interest in this research. For the nontrivial solution, there is an eigen vector for every eigenvector. In structural dynamics the eigenvalue and eigenvector are typically called the natural frequency and natural mode, respectively.

## 2.1 Finite element modeling

The previous section addresses the theoretical basis for the finite element model in this dissertation. The lifting surfaces in this dissertation are cantilevered thin, elastic plates. The structure is modeled using SHELL63, a 4-node shell element. The thickness of the shell is uniform. The hole in the structure is made by subtracting the area of the hole at a specific location from the area of the wing. The geometry is meshed after defining the shape of the hole area removed. Meshing the plate-like structure with a free mesh is sufficient in the finite element analysis instead of doing a mapped mesh. The cantilever boundary condition for the plate is enforced by stating that no displacement or rotation occurs where the plate is clamped. A representative free mesh with the clamped root (represented by 3 triangles) for the plate with a hole is displayed in Figure 2.1. The discretization requires using on average 1000 elements to achieve converge results. In extracting the natural modes for the wing without any stores, the Subspace Algorithm is used to solve the eigenvalue problem because it is accurate and computationally efficient. The Block Lanczos Method and the Subspace method are used to solve the classical eigenvalue problem in ANSYS™ to extract the structural modes and natural frequencies. For additional information, see the ANSYS™ User manual [33].

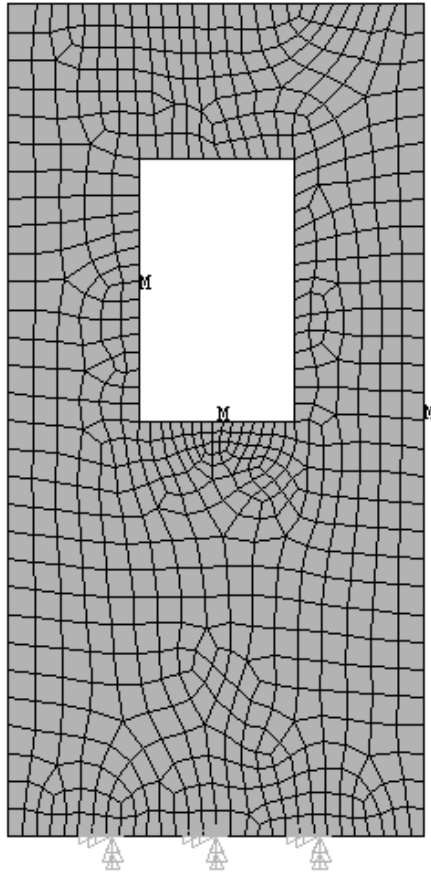


FIGURE 2.1: A typical free mesh of a plate with a hole in ANSYS™ with the fully clamped root

## 2.2 Preliminary studies: Validation of ANSYS™

The effectiveness of the finite element method(FEM) for a steel rectangular plate clamped on all four sides, see Fig. 2.2, is tested against the experimental and theoretical results found by Takahashi for the parameters  $a/b = 4/8$  with  $\nu=0.3$ . The steel plate analyzed in the ANSYS™ has the following material properties: a thickness of 0.003175 m, a density of 7870 kg/m<sup>3</sup>, a modulus of elasticity of 205e9 N/m<sup>2</sup>, and a Poisson's ratio of 0.30. These material properties are generic to steel, but they may or may not be same the properties for steel used by Takahashi since they are not stated in the 1960 National Advisory Committee for Aeronautics(NACA is the present day NASA) report by Leissa [19]. The nondimensional frequency as defined by Takahashi avoids the need to specify the material properties. The results shown vary with the hole radius,  $R$ , for a range of the dimensionless quantity  $R/a$ , when  $a$  is known as a side in the rectangular plate in Figure 2.2. Side  $a$  has a fixed length of 0.2032 m. The results produced by ANSYS™ for the fundamental frequency are lower than those of Takahashi as seen in Figure 2.3. Both Takahashi and ANSYS™ use the Rayleigh Ritz Method fundamentally, but there is a slight difference [19, 33]. Takahashi developed a general approach to calculating the natural frequencies based upon the Rayleigh Ritz Method using products of beam functions. However in his numerical calculations he used only a single basis function. It is of course well known according to Meirovitch [34] that the Rayleigh Ritz Method gives values of frequencies that are higher than the true values and the method converges from above to the exact answer as more basis functions are included in the calculations [34]. Therefore it is not surprising that Takahashi's frequencies presented by Leissa in the 1960's are higher than those predicted by the present calculations using ANSYS™.

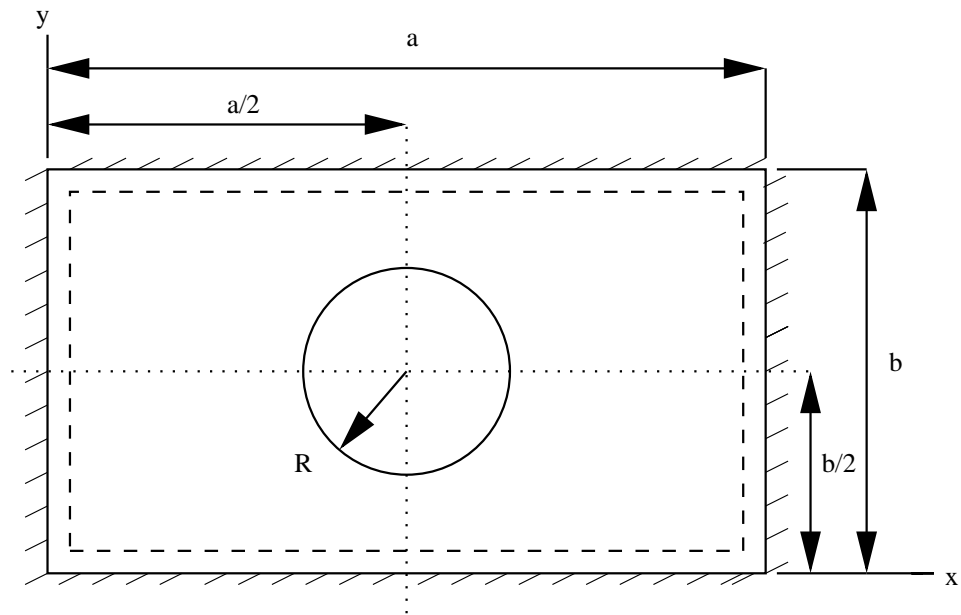
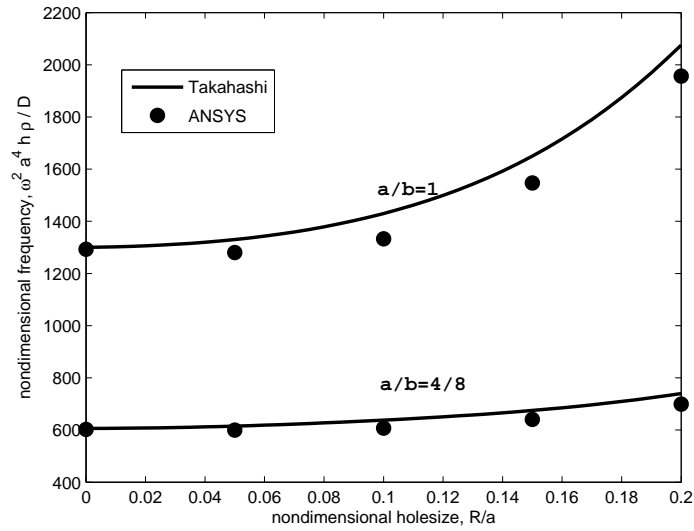
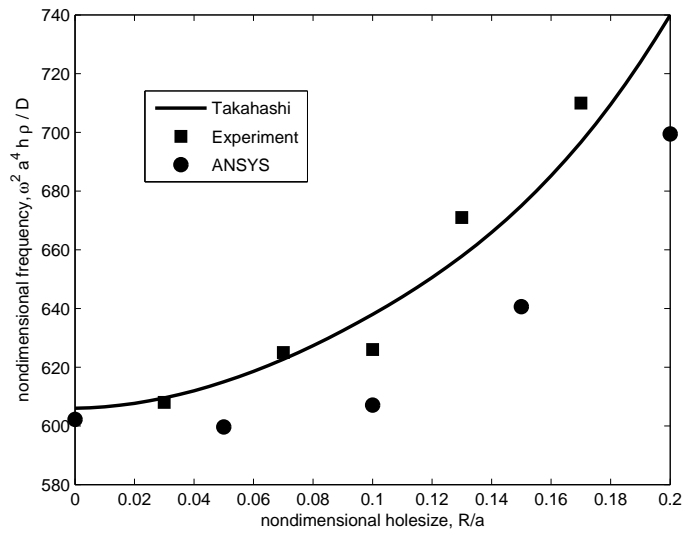


FIGURE 2.2: Clamped rectangular plate having a centralized circular hole studied by Takahashi



(a) Results for Takahashi and ANSYS™ for  $a/b=1/2$  and  $a/b=1$



(b) Results from Takahashi, ANSYS™, and experiment  $a/b=1/2$ ,  $\nu=0.3$

FIGURE 2.3: Plots of nondimensional frequency parameter  $\frac{\omega^2 a^4 \rho}{D}$  as a function of hole size for a clamped rectangular plate.  $D = Eh^3/12(1 - \nu^2)$  is the flexural rigidity of the plate

### *2.2.1 Experimental setup for preliminary structural investigations*

After modeling Takahashi experiment, new experiments were designed and tested. PULSE™ is an advanced software/hardware analyzer platform developed by Brüel & Kjaer designed specifically for noise and vibration analysis [35]. The PULSE™ systems consists of a personal computer(PC) with local area network(LAN) interface, PULSE™ software, Microsoft Windows™ and the B&K 4 Channel PULSE™ 3560-T-C , the front-end data acquisition system as in Figure 2.5. The PULSE™ system is capable of doing analysis in real time, therefore, data can be verified immediately. PULSE™ can do multiple types of analysis at the same time while performing fast fourier transform(FFT), 1/n octave constant percentage bandwidth, or overall analysis on the same or different channels while producing real time results. The PC serves as the analyzer in that it allows measurements to be taken and processed while running the experiment.

The structural behavior predicted by ANSYS™ was evaluated experimentally for various shaped plates. The natural frequencies of the plates were determined by measuring the input force from a electromagnetic actuator(shaker) and the output from an accelerometer. The location of the shaker and accelerometer is placed in various locations during a given experiment to excite all the modes. Sometimes it is hard to excite some modes with one shaker. The most effective location to place the shaker is near the clamped cantilever base as seen in Figure 2.4. Where as the B&K type 4375 accelerometer most effective location is farthest away from the shaker near the tip of the cantilevered plate. The shaker is a Brüel & Kjaer(B&K) 4810 mini-shaker mounted with a Brüel & Kjaer(B&K) 8200 force transducer. The shaker is powered by an external power amplifier. The shaker outputs a pseudorandom signal for most of the vibration tests. A pseudo random signal in PULSE™ reduces the experimental test time, but maintains the required accuracy when using an FFT

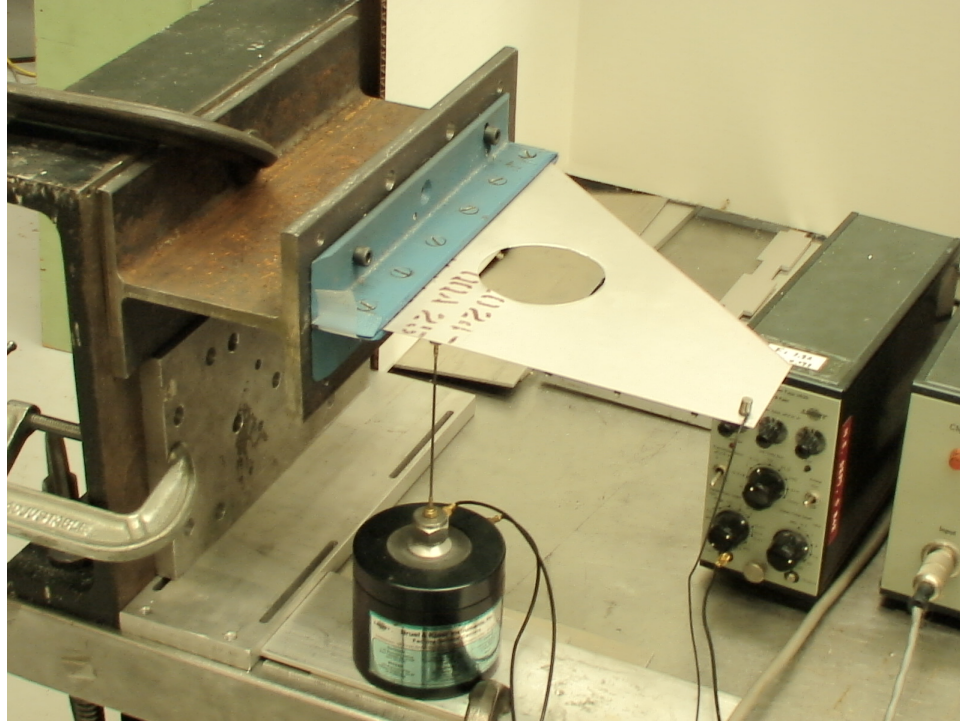


FIGURE 2.4: Closeup view of shaker and accelerometer on model for vibration tests for determining the natural frequencies

averaging analysis to find the natural frequencies instead of with a random, sine, or sine sweep signal. While the pseudo random signal provides good data for the most part, a sine signal is used to hone in on some hard to excite modes. The data is collected and analyzed using PULSE™.

In addition to a vibration test, the structural properties are validated using a hammer test. A Brüel & Kjær (B&K) transducer fitted impact hammer and a B&K type 4375 accelerometer are used in the hammer test. A B&K type 2635 charge amplifier is used to increase the signal from the accelerometer. The transfer function between the accelerometer and hammer is measured using the B&K PULSE™ data acquisition system and software. The hammer test readily determined the first three modes. The higher modes, specifically the fifth mode and higher, were harder to excite with the hammer test since the vibrations damped out fairly quickly after



FIGURE 2.5: Equipment setup for vibration tests for determining the natural frequencies for the structural models

impact.

The first series of tests were conducted on a cantilevered acrylic square plate with a square cutout as seen in Figure 2.6. The acrylic plate is 0.001524 m thick with 0.2032 m sides and a square cutout of 0.0508 m sides. Acrylic has the following material properties: density of  $1190 \text{ kg/m}^3$ , modulus of elasticity of  $3.3\text{e}9 \text{ N/m}^2$  and a Poisson's ratio of 0.40. Overall, the results from the experiment correlate well with the values produced by ANSYS<sup>TM</sup> as seen in Table 2.1. In Table 2.1, the "\*" symbol indicates the torsion mode was not found experimentally. One explanation for not finding the torsion mode is that only one accelerometer and one shaker were used during the experiment. Multiple shakers and accelerometers may have been needed to excite and capture the higher frequency torsion modes.

Follow up investigations were performed on two acrylic cantilevered cropped delta wing models with circular holes since this is the geometry of interest for aeroelastic

studies. The dimensions of both cropped delta wings are as follows: the chord is 0.2032 m(8 in), the span is 0.1800 m(7.088 in), the area is 0.02337 m<sup>2</sup>(36.2339 in<sup>2</sup>), and the thickness is 0.001524 m(0.060 in). In Figure 2.6, the above dimensions can be seen in the nondimensional representation of the cropped delta wing. The difference among the models in Table 2.2 is in the location of hole of radius 0.0307 m. The location of the hole is designated by a coordinate system on the wing with the origin at the root chord at the leading edge, see Fig. 2.2. The results of model 1, with its hole centered at  $x=0.1265$  m and  $y=0.0604$  m near the root, are in Table 2.2. Model 2 results with its hole centered at  $x=0.1629$  m and  $y=0.1202$  m near the tip are also listed in Table 2.2. In both cases the correlation of theory and experiment is good.

During work on the Master's Thesis not shown here[36], aluminum was used as the material for the wing's plate-like structure. Aluminum was problematic since the cutting of the hole introduced a buckling problem. Therefore, for these preliminary structural studies, acrylic was used to avoid the buckling problem created during machining. The results for aluminum were good, but they were improved upon by changing to a new plastic material where buckling was eliminated.

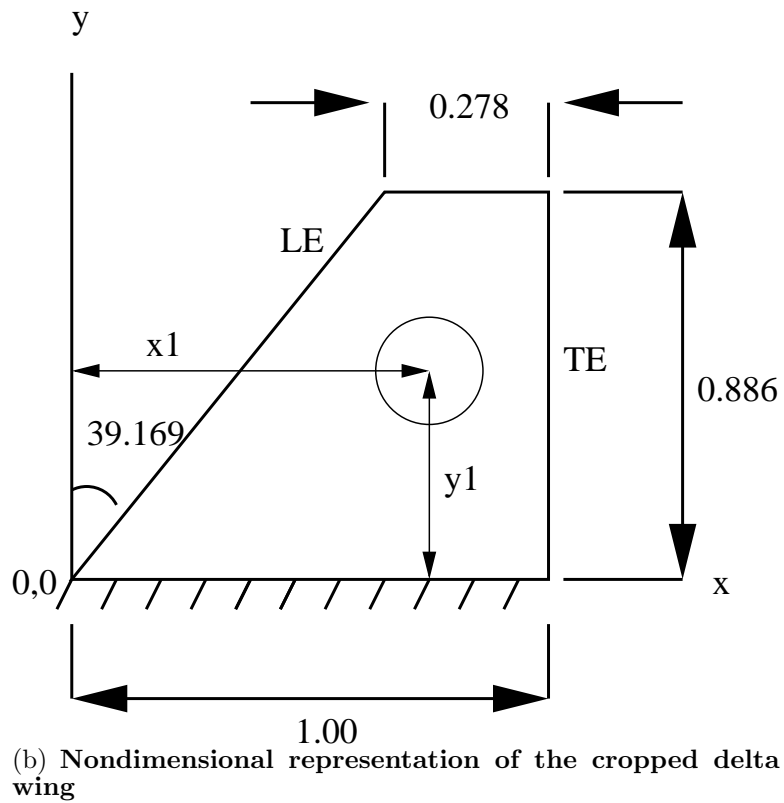
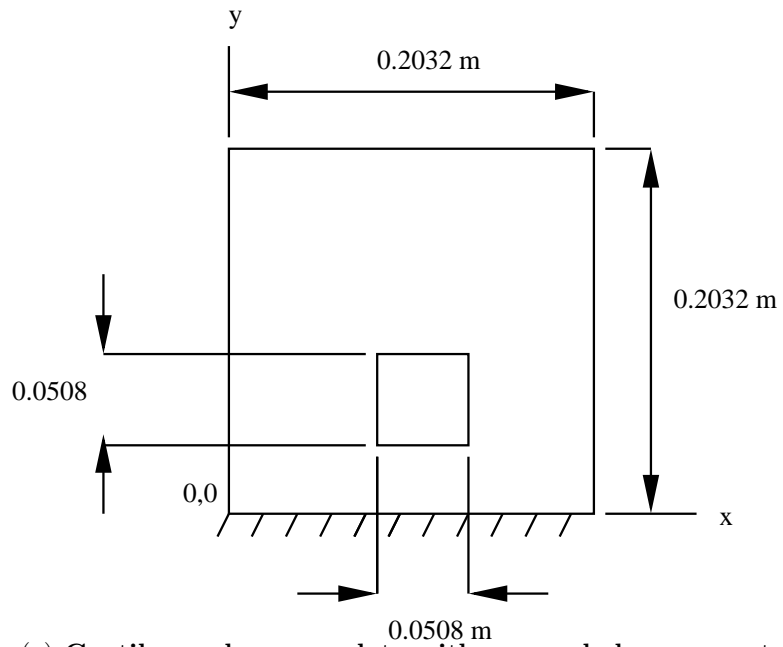


FIGURE 2.6: Two cantilevered plate configurations

### Cantilevered acrylic square plate natural frequencies

		Hole		No hole	
mode no.	mode char.	ANSYS	exp.	ANSYS	exp.
1	Bend	9.387 Hz	9.75 Hz	10.354 Hz	10.75 Hz
2	Tors	24.023	24.25	25.049	24.75
3	Bend	62.240	66.5	63.169	73.75
4	Tors	79.508	*	81.011	*
5		90.567	93.5	91.572	93.00

Table 2.1: The first five natural frequencies of the plate in Figure 2.6 with a hole near the root as determined by ANSYS™ and the experiment. The second torsion mode is not excited, see the text for more information regarding “\*.”

### Cantilevered acrylic CDW natural frequencies

mode no.	mode char.	Model 1		Model 2		no hole
		x,y coordinates		x,y coordinates		
		(0.123 m, 0.060 m)		(0.163 m, 0.120 m)		
		ANSYS	exp.	ANSYS	exp.	ANSYS
1	Bend	15.080 Hz	15.50 Hz	19.253 Hz	19.00 Hz	17.473 Hz
2	Tors	59.018	63.25	58.722	56.00	62.529
3	Bend	89.999	90.75	81.390	88.50	91.271
4	Tors	150.97	154.00	141.13	147.50	156.64

Table 2.2: Comparison of experimental and ANSYS™ results of first four natural frequencies(in Hz) of the CDW with a hole of radius 0.0307 m at two x,y locations

## 2.3 Structural dynamics conclusions

The commercial finite element software, ANSYS<sup>TM</sup>, modeled the clamped rectangular steel plate studied by Takahashi well. ANSYS<sup>TM</sup> is capable of accurately predicting the structural behavior in various shaped cantilevered plates with holes made out of various materials.

Using insight gathered from beam theory, it is suspected that the first few natural frequencies would go down if the hole is near the root. The reason is that “stiffness effects” plays a more dominant role when the hole is near the root. On the contrary, a hole near the tip causes the natural frequencies to go up since “mass” is more dominant. The results presented up to this point validate both scenarios for the lower modes although a plate is being modeled. In addition, it is well known in flutter analysis that the first few structural modes generally dominate the aeroelastic modes for which this work is a basis. As a result, accurately predicting these modes are very important.

In the ANSYS<sup>TM</sup> calculations, various aspects of the modeling were considered to see if more accurate results could be found. The first item changed was the finite element type from SHELL63 to SHELL93. These two shells elements were the most applicable for the analysis of a thin, linear, and elastic plate. The change yielded results that were insignificant. A convergence study was also performed. In performing one part of the convergence study, the mesh was refined. Mesh refinement was carried out initially around the hole since that area is highly sensitive. Further, the other part of the convergence study examined the effects of a triangular element versus a quadrilateral element generated mesh. The results changed very little from this study.

# 3

## Unsteady Aerodynamics

The lifting surface in this dissertation is modeled as a thin wing in an unsteady, subsonic flow field to determine the aerodynamic forces. The fluid flow is modeled as a compressible, inviscid, irrotational potential flow. The doublet lattice method is used to solve the potential flow model numerically.

### 3.1 Governing equations

The governing conservation equations for the fluid are known as Euler's differential equations[30]. The conservation of mass and the conservation of momentum equations are expressed in Eqn. 3.1 and Eqns. 3.2-3.4, respectfully. Equations 3.1-3.4 are valid for all inviscid, Newtonian fluids. The isentropic relation in Eqn. 3.5 closes the system with the conservation of mass and the conservation of momentum. Therefore, the flow field can be fully understood by solving the five equations with five unknowns but this is not trivial [37]. The five unknowns are the state variables for pressure( $p$ ), density( $\rho$ ), and the three components of velocity( $u,v,w$ ). For brevity, the three components of velocity are represented as a vector,  $\vec{q} = \langle u, v, w \rangle$ . Solving the nonlinear partial differential equations(PDEs) in Eqns. 3.1-3.4 can be done using

numerical methods [37].

$$\frac{\partial \rho}{\partial t} + \nabla \cdot (\rho \vec{q}) = 0 \quad (3.1)$$

$$\frac{\partial u}{\partial t} + u \frac{\partial u}{\partial x} + v \frac{\partial u}{\partial y} + w \frac{\partial u}{\partial z} = \frac{-1}{\rho} \frac{\partial p}{\partial x} \quad (3.2)$$

$$\frac{\partial v}{\partial t} + u \frac{\partial v}{\partial x} + v \frac{\partial v}{\partial y} + w \frac{\partial v}{\partial z} = \frac{-1}{\rho} \frac{\partial p}{\partial y} \quad (3.3)$$

$$\frac{\partial w}{\partial t} + u \frac{\partial w}{\partial x} + v \frac{\partial w}{\partial y} + w \frac{\partial w}{\partial z} = \frac{-1}{\rho} \frac{\partial p}{\partial z} \quad (3.4)$$

$$\frac{p}{\rho^\gamma} = \text{constant} \quad (3.5)$$

The flow field is described above using five equations with five unknowns, but it is ultimately desired to have one equation with one unknown. The flow is assumed to be inviscid and irrotational, so the five equations can be reduced to three equations. For irrotational flow, one may show that  $\nabla \times \vec{q} = 0$  is true and thus  $\vec{q} = \nabla \phi$  where  $\phi$  is the scalar velocity potential. The curl of the gradient disappears as the result of Kelvin's Theorem. Kelvin's Theorem states that a flow which is initially irrotational, remains so at all later times in the absence of dissipation by viscosity or shock waves [38]. The use of the velocity potential allows the three momentum equations to be written compactly into one equation.

$$\vec{q} = \nabla \phi = \langle u, v, w \rangle = \hat{i} \frac{\partial \phi}{\partial x} + \hat{j} \frac{\partial \phi}{\partial y} + \hat{k} \frac{\partial \phi}{\partial z} \quad (3.6)$$

The momentum equation relates the pressure( $p$ ) to the velocity potential( $\phi$ ) after being manipulated using vector calculus, Leibnitz' Rule, and the far field assumption. The far field assumption states that far away in the fluid there are no disturbances. As a result, the Unsteady Bernoulli's Equation, Eqn. 3.7, is derived from the momentum equation.

$$\frac{\partial \phi}{\partial t} + \frac{\nabla \phi \cdot \nabla \phi}{2} + \int_{p_\infty}^p \frac{1}{\rho_1} dx = \frac{U_\infty^2}{2} \quad (3.7)$$

Further reduction of three equations into one is achieved by using Leibnitz' Rule, the Unsteady Bernoulli's Equation, and the isentropic relation in the conservation of mass. The resultant nonlinear partial differential equation(PDE) in Eqn. 3.8 has only one unknown, the velocity potential. The speed of sound,  $a$ , arises from the isentropic nature of the fluid that relate density, pressure, temperature and specific heat. Strictly speaking it is an unknown as well. However in classical aerodynamic theory,  $a$  is assumed to be equal to the free stream value,  $a_\infty$ .

$$\nabla^2 \phi - \frac{1}{a^2} \left[ \frac{\partial}{\partial t} (\nabla \phi \cdot \nabla \phi) + \frac{\partial^2 \phi}{\partial t^2} + \left( \frac{\nabla \phi \cdot \nabla \phi}{2} \right) \right] = 0 \quad (3.8)$$

The nonlinear PDE in Eqn. 3.8 is extremely difficult to solve in this form, so it is simplified using small perturbation theory. Small perturbation theory is widely used in acoustics to linearize the governing equations [1]. The nonlinear PDE in Eqn. 3.8 is linearized about a uniform flow field,  $U_\infty$ , in the positive x-direction. The linearization reduces the nonlinear PDE to the classical linear small disturbance velocity potential PDE, Eqn. 3.9. The Mach number is defined as  $M = U_\infty/a_\infty$  and the classical linear small disturbance velocity potential PDE can be rewritten

as the aerodynamic potential equation, Eqn. 3.10. Note, the tilde's are left off for convenience in Eqn. 3.10.

$$a = a_\infty + \tilde{a}, \quad \phi = U_\infty x + \tilde{\phi}$$

$$\nabla^2 \tilde{\phi} - \frac{1}{a_\infty^2} \left[ \frac{\partial^2 \tilde{\phi}}{\partial t^2} + 2U_\infty \frac{\partial^2 \tilde{\phi}}{\partial x \partial t} + U_\infty^2 \frac{\partial^2 \tilde{\phi}}{\partial x^2} \right] = 0 \quad (3.9)$$

$$(1 - M^2) \frac{\partial^2 \phi}{\partial x^2} + \frac{\partial^2 \phi}{\partial y^2} + \frac{\partial^2 \phi}{\partial z^2} - \left( \frac{2U}{a_\infty^2} \right) \frac{\partial^2 \phi}{\partial x \partial t} - \left( \frac{1}{a_\infty^2} \right) \frac{\partial^2 \phi}{\partial t^2} = 0 \quad (3.10)$$

### 3.1.1 Aerodynamic potential equation and boundary conditions

Solving the aerodynamic potential equation requires specifying a frame of reference. For this research, the frame of reference is a fixed body with a moving fluid. A frame of reference fixed with respect to fluid allows a coordinate transformation to change the aerodynamic potential equation to the acoustic potential equation in Eqn. 3.11, also known as the classical wave equation. Insight for a solution is acquired for the closely related aerodynamic potential equation by initially solving the wave equation.

$$\nabla^2 \phi - \frac{1}{a^2} \frac{\partial^2 \phi}{\partial t^2} = 0 \quad (3.11)$$

Solving the aerodynamic potential equation requires knowing the appropriate boundary conditions. The easiest boundary condition to understand occurs at infinity. The wave disturbances caused by the lifting surface's motion propagate outwardly toward infinity and are not reflected back into the system. The other boundary condition, Eqn. 3.12 states the normal velocity of the fluid at the surface equals

the normal velocity of the body. In other words, there is no flow component perpendicular to the surface. For the thin wing in this work,  $F(x, y, z, t) = z - f(x, y, t)$  in Eqn. 3.12 where  $z = 0$  at the surface of the airfoil and  $f(x, y, t)$  refers to the height of the wing surface above the plane. The resulting boundary condition after substituting  $F$  into Eqn. 3.12 is  $\partial f / \partial t + U_\infty \partial f / \partial x = w$  at  $z = 0$ . This boundary condition is useful for solving for the flow over the wing. The structural modes determined in an earlier chapter will be used for the planar wing's deflection to determine the aerodynamic forces in the aeroelastic model.

$$\frac{\partial F}{\partial t} + \vec{q} \cdot \nabla \vec{F} = 0 \tag{3.12}$$

After finding the potential, the flow over the wing can be computed. In brief, one computes the velocity potential to find the doublet, the source sheet, the pressure doublet, and then the doublet sheet [30].

### *3.1.2 Pressure potential equation and the Kernel's function*

Previously the velocity potential( $\phi$ ) is the only unknown in the aerodynamic system. The wing's deformation is the input and the output is pressure after an intermediate step using the velocity potential. The intermediate step is eliminated by introducing the pressure potential and the acceleration potential( $\psi$ ). As a result, the aerodynamic potential equation is transformed into the pressure potential equation. Using the pressure potential to calculate the pressure differential across the surface is beneficial, especially for a wing with a hole.

**Four steps to transform the aerodynamic potential equation into the pressure potential equation**

1. Differentiate the aerodynamic potential equation by  $t$  and  $x$ , separately
2. Multiply the equation differentiated with respect to “t” by  $\rho$
3. Multiply the equation differentiated with respect to “x” by  $\rho U$
4. Add the equations produced in step 2 and 3 to obtain Eqn. 3.13

$$\beta^2 \rho (\phi_t + U \phi_x)_{xx} + \rho (\phi_t + U \phi_x)_{yy} + \rho (\phi_t + U \phi_x)_{zz} - \left[ \frac{2U}{a^2} \rho (\phi_t + U \phi_x)_{xt} \right] - \left[ \frac{1}{a^2} \right] \rho (\phi_t + U \phi_x)_{tt} = 0 \quad (3.13)$$

The linearized Bernoulli's equation states that  $\Delta p = -\rho [\Delta \phi_t + U \Delta \phi_x]$ . After performing the four steps above with some algebraic manipulation the results yield the linearized Bernoulli's equation that is embedded in Eqn. 3.13. In Eqn. 3.13, the effects of compressibility is expressed as  $\beta^2 = (1 - M^2)$ . Rewriting Eqn. 3.13 with the linearized Bernoulli's equation yields the pressure potential equation Eqn. 3.14. The pressure potential equation is mathematically identical to the aerodynamic potential equation [Eqn. 3.10] but the physical meanings are different. The solution is known for aerodynamic potential equation so the solution is known for the pressure potential equation since it is mathematically equivalent.

$$\beta^2 p_{xx} + p_{yy} + p_{zz} - \left[ \frac{2U}{a^2} \right] p_{xt} - \left[ \frac{1}{a^2} \right] p_{tt} = 0 \quad (3.14)$$

Currently, the problem is in the time domain but solving it in the frequency domain yields great computational savings. When going to the frequency domain,

the problem also enters the complex domain. Similarly to solving the aerodynamic potential equation, the pressure potential equation requires finding a pressure doublet which is referred to as the acceleration potential( $\psi$ ). The acceleration potential is defined in Eqn. 3.15 where  $A = A(\omega)$  is the amplitude of the oscillations dependent on frequency at  $(x, y, z)$  due to a single pressure doublet located at  $(\xi, \eta, \zeta)$  at a distance,  $\bar{R}$ .

$$\psi(x, y, z) = A \frac{\partial}{\partial z} \left[ \frac{1}{\bar{R}} e^{\frac{i\omega}{a\beta^2} (M(x-\xi) - \bar{R})} \right] \quad (3.15)$$

$$\bar{R} = [(x - \xi)^2 + \beta^2(y - \eta)^2 + \beta^2(z - \zeta)^2]^{1/2}$$

The acceleration potential is expanded across a continuum in the  $(\xi, \eta, \zeta = 0)$  plane for a rectangular differential area,  $dS = d\xi d\zeta$ , but it can be any shaped area. The integral expression produced in Eqn. 3.16 is singular because of  $\bar{R}$  and to integrate the equation special treatment is needed. The special treatment is to perform another coordinate transformation and take the limit of  $\psi(x, y, z)$  as  $z \rightarrow 0$ . The important result is the expression for the jump in acceleration is  $\Delta\psi(x, y) = 4\pi A$ . Since  $p = \rho_o\psi$  and  $\Delta\psi = 4\pi A$ , then  $\Delta p = 4\pi\rho A$  or  $A = \Delta p/4\pi\rho$ . The sign convention on  $+\Delta p = p_l - p_u$  causes a positive lift if a negative pressure is on the “+z” side of the wing and a positive pressure is on the “-z” side of the wing.

$$\psi(x, y, z) = \beta^2 z \int_S A(\xi, \zeta) \left[ \frac{i\omega}{\bar{R}^2} - \frac{1}{\bar{R}^3} \right] e^{\frac{i\omega}{a\beta^2} (M(x-\xi) - \bar{R})} d\xi d\eta \quad (3.16)$$

In addition, the change of variables from the aerodynamic potential to the pressure potential equation requires the boundary conditions to be updated. Recall, the z-component of velocity is related to the velocity potential where  $\bar{w} = \partial\phi/\partial z$ . The “updated” downwash( $\bar{w}$ ) is computed using the acceleration potential expression Eqn. 3.15 in Eqn. 3.17. It is necessary to use a distribution of doublets in Eqn.

3.16 and it is again necessary when calculating the wash. In essence, calculating the wash in Eqn. 3.18 is the foundation of the doublet lattice method. Often times, the wash is noted as in Eqn. 3.19 where K is referred to as the Kernel [1, 30]. Equation 3.19 is expressed in the literature in several slightly different forms.

$$\phi(x, y, z) = -\frac{1}{U} e^{\frac{-i\omega x}{U}} \int_{-\infty}^x e^{\frac{i\omega\alpha}{U}} \bar{\psi}(\alpha, y, z) d\alpha \quad (3.17)$$

$$\bar{w}(x, y, z) = \frac{-1}{4\pi\rho U} \int \int_S (\Delta\bar{p}) e^{\frac{-i\omega(x-\xi)}{U}} x \frac{\partial^2}{\partial z^2} \left[ \int_{-\infty}^{x-\xi} \frac{1}{R} e^{\frac{i\omega}{U\beta^2}(\lambda-M\bar{R})} d\lambda \right] d\xi d\eta \quad (3.18)$$

$$\bar{w}(x, y, z) = \left[ \frac{-1}{4\pi\rho} \right] \int \int_S \Delta\bar{p} K((x-\xi), (y-\eta), z) d\xi d\eta \quad (3.19)$$

## 3.2 Doublet lattice method

The doublet lattice method(DLM) is a “Kernel” function or integral equation approach that divides the lifting surface into boxes and collocation points[29, 39, 40]. They are used to relate downwash to pressure on harmonically oscillating surfaces in subsonic flows. Essentially, the DLM is a finite element method for solving the integral equation. The DLM governing integral equation is

$$\bar{w}(x, y) = \frac{1}{8\pi} \int \int_s K(x, \xi; y, \eta; \omega, M) \bar{p}(\xi, \eta) d\xi d\eta \quad (3.20)$$

where  $\bar{w}$  is the complex amplitude of nondimensional wash,  $\bar{p}$  is the complex non-dimensional amplitude of the lifting pressure coefficient, and K is the complex acceleration potential kernel for oscillatory, subsonic flow. The kernel has been defined

by Rodemich and Landahl[41] as

$$K = e^{(i\omega x_o/U)}(K_1 T_1 + K_2 T_2)/r_1^2 \quad (3.21)$$

where it is composed of the planar and nonplanar parts in  $K_1$  and  $K_2$ , respectively. In the work here, the  $K_2$  term is neglected since the planar wing is the focus of the work here. Furthermore,  $T_1 = 1$  for a planar wing. Further details on the planar and nonplanar wing can be seen in Albano and Rodden[29] first paper.

$$r_1 = |y_o| \quad (3.22)$$

$$x_o = x - \xi, y_o = y - \eta \quad (3.23)$$

Landahl[41] simplified  $K_1$  in the Kernel function in Eqn. 3.21 to the following form.

$$K_1 = I_1 + [Mr_1/R][e^{-ik_1 u_1}/(1 + u_1^2)^{1/2}] \quad (3.24)$$

$$I_1 = \int_{u_1}^{\infty} \frac{e^{-ik_1 u}}{(1 + u^2)^{3/2}} du \quad (3.25)$$

$$u_1 = (MR - x_o)/\beta^2$$

$$k_1 = \omega r_1/U, \beta = (1 - M^2)^{1/2}, R = (x_o^2 + \beta^2 r_1^2)^{1/2}$$

Evaluating the  $I_1$  integral requires special treatment. Albano and Rodden first used an approximation by Watkins, Runyan, and Cuttingham to evaluate this integral[29]. Improvements on evaluating the integral in Eqn. 3.25 can be seen in more recent works by Rodden and others[29, 39, 40]. Evaluating the  $I_1$  integral is “the heart”

of the DLM. In the original paper, a parabolic approximation was used to calculate  $I_1$ . In 1998, Rodden improved the doublet lattice method by integrating a quartic approximation[40] and it is used here.

Solving Eqn. 3.20 directly for the pressure is difficult, therefore it is computed using a finite element discretization. The DLM method assumes that the lifting surface can be divided into boxes arranged in columns parallel to the free stream with the fold and surface lines coinciding on the box boundaries[29]. On the quarter chord line of each box, a distribution of acceleration potential doublets are uniformly spread of unknown strength[29, 39, 40]. For steady flow, the doublet line segment is the equivalent to a bound horseshoe vortex. Each doublet line segment for “ $n$ ” number of boxes will create a force,  $f_i$ . The relation between the normal wash induced at a point  $(x_i, y_i)$  by  $j$ th doublet line on the surface is determined below after discretization of Eqn. 3.20.

$$w_i(x_i, y_i) = \left( \frac{f_i}{4\pi\rho} U^2 \right) \int_{I_j} K[x_i, y_i; x_j(\mu), y_j(\mu)] d\mu$$

The sum of the normal washes caused by the  $n$  doublet line at point  $(x_i, y_i)$  is the total normal wash.

$$w_i(x_i, y_i) = \sum_{j=1}^n \left( \frac{f_i}{4\pi\rho} U^2 \right) \int_{I_j} K[x_i, y_i; x_j(\mu), y_j(\mu)] d\mu \quad (3.26)$$

The above integrals are singular, so they are evaluated in the “Mangler sense.” For more information on the “Mangler Sense,” see Blisplinghoff, Ashley, and Halfman [2]. The force on the box and therefore the pressure difference across the box is due to force on the doublet line as approximated by  $p_i = \text{force}/\text{box area} = f_i/\Delta x_j \cos \lambda_j$ . The area is approximated for cases where the wing are swept by defining the box

average chord  $\Delta x_j$  and the sweep angle of the doublet line segment,  $\lambda_j$ . Equation 3.26 can be expressed in matrix form in

$$\bar{w}_i = \sum_{j=1}^n D_{ij} \bar{p}_j$$

where

$$D_{ij} = \left( \frac{1}{8\pi} \right) \Delta x_j \cos \lambda_j \int_{I_j} K[x_i, y_i; x_j(\mu), y_j(\mu)] d\mu \quad (3.27)$$

The attractiveness of the DLM is that the force on the box can be calculated without concern to what is occurring in the wake, unlike the vortex lattice method. The standard vortex lattice method (VLM) would have greater difficulty handling the hole. The underlying theory behind the VLM assumes the horseshoe vortices do not stop in the fluid and the presence of the hole would violate this assumption.

### 3.3 Results for the 2-d doublet lattice method

The 2-d equivalent of the doublet lattice method 3-d integral equation, Eqn. 3.20, for planar flow is the Possio's Integral Equation [29, 2]. The incompressible flow kernel for the Possio's Integral with a slight correction from the version found in Bisplinghoff et al. [2] is as follows:

$$K \left( 0, \frac{k(x-\xi)}{b} \right) = \frac{1}{2\pi} \left\{ i e^{-i \frac{k(x-\xi)}{b}} \left[ Ci \left( \left| \frac{k(x-\xi)}{b} \right| \right) + i \left( \frac{\pi}{2} + Si \left( \frac{k(x-\xi)}{b} \right) \right) \right] \right\} \\ - \frac{1}{2\pi} \left\{ \frac{1}{\frac{k(x-\xi)}{b}} \right\}. \quad (3.28)$$

The Cosine and Sine integrals used in the Kernel are defined according to Abramowitz and Stegun[42]. The kernel assumes the sending and receiving points are at the quarter chord and three-quarter chord position, respectfully. The results by Albano and Rodden[29] for an airfoil with oscillating flap were duplicated in Figure 3.2. Furthermore, the results were compared to Theodorsen for a plunging airfoil and Sears for the gust response of an airfoil[2]. For a low nondimensional frequency,  $k$ , only a few panels are needed for good agreement with classical theory as shown in Figures 3.3 and 3.4. As the frequency increases, more panels are needed to obtain good agreement with Theodorsen’s theory as seen in Figures 3.3 and 3.4.

### 3.4 Results for 3-d doublet lattice method

The first results are shown for steady and incompressible flow of a rectangular wing with an aspect ratio=1.0 at one radian angle of attack. Aspect ratio is defined as the span squared divided by the area. The coefficient of lift,  $C_L$ , for a low aspect ratio wing is approximately equal to  $\pi/2$ . A convergence study, in Figure 3.5 shows the DLM result approximates  $\pi/2$  as the box density is increased. The aspect ratio(AR) of each box is also equal to one.

The original DLM works well for a box AR between 1 and 3 since it uses a parabolic approximation to determine the kernel [29]. Outside these limits, the original DLM breaks down. Rodden improved the original DLM results using a quartic approximation to find the kernel [40]. Specifically, computing  $I_1$  in Eqn. 3.25 is improved by Rodden and et. al by switching from a parabolic approximation in 1969 [29] to a quartic approximation in 1998 [40]. Rodden also notes that with the higher order approximation, the limitation of the box aspect ratio can be relaxed to 5 and the divisions in the spanwise direction can be drastically reduced without losing accuracy [40]. As the nondimensional frequency increases, the mesh density must be increased to capture the unsteady effects [40].

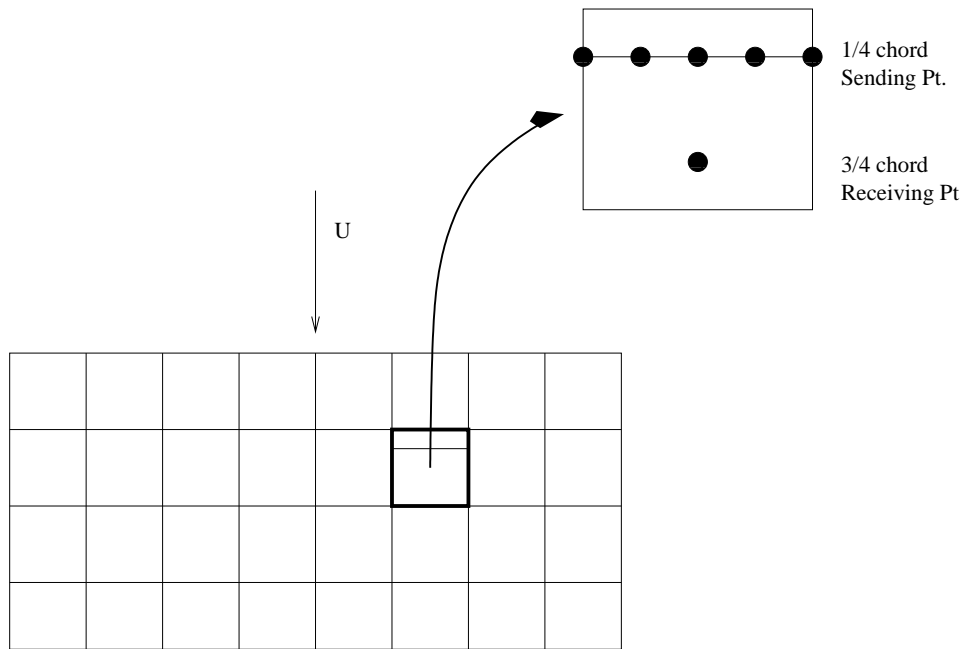


FIGURE 3.1: General grid for the doublet lattice method

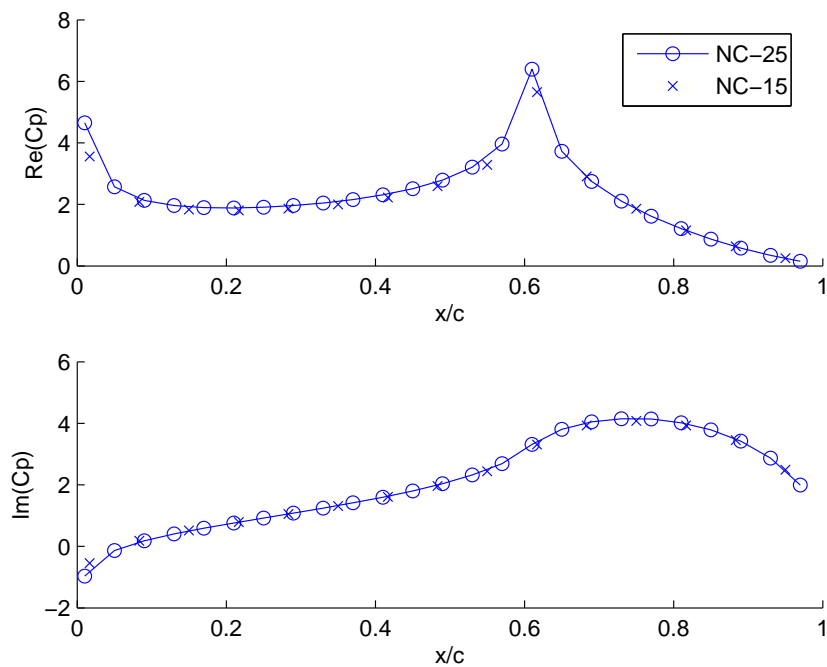
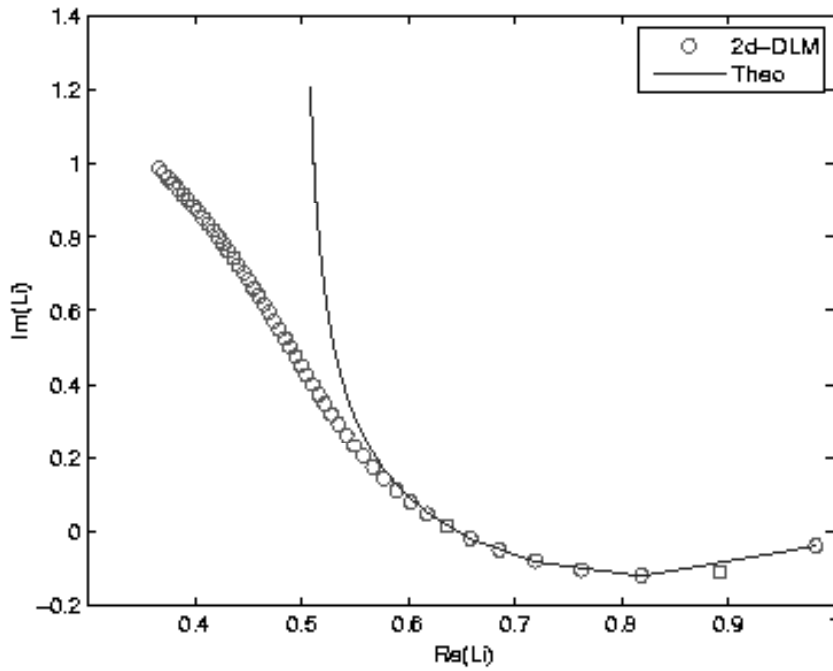
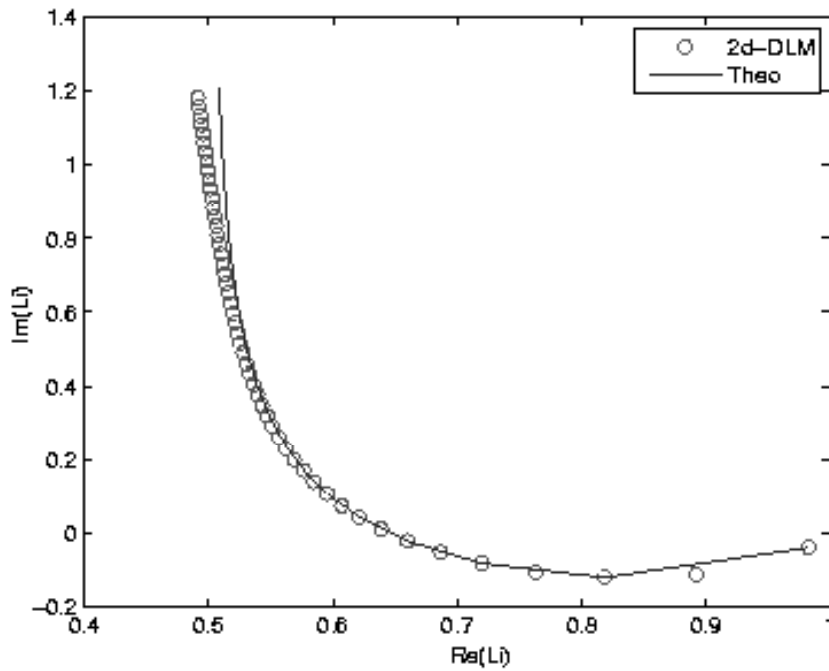


FIGURE 3.2:  $C_p$  on airfoil with oscillating flap in incompressible flow,  $k=1.0$

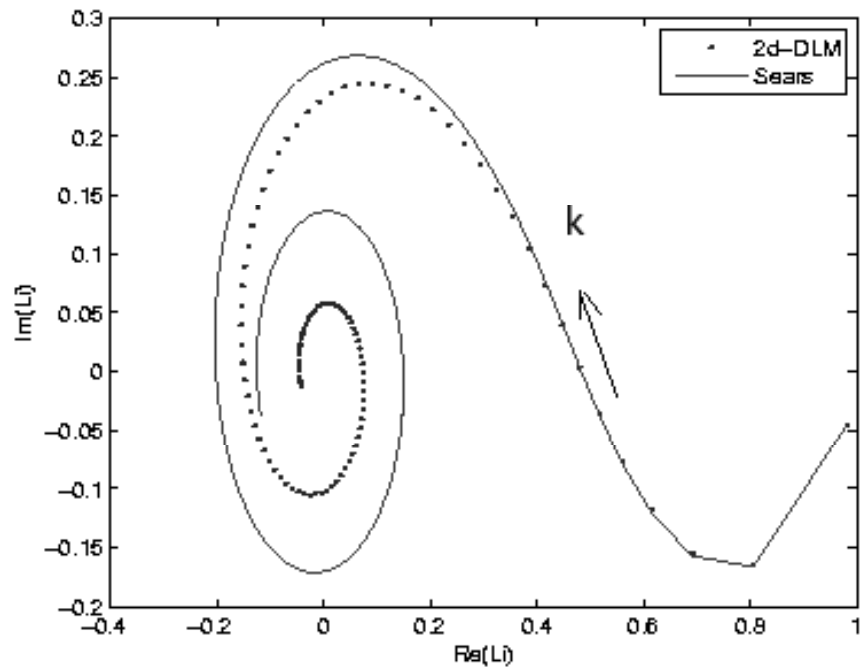


(a) Comparison of doublet lattice to Theodorsen results for  $n=10$  chord-wise divisions

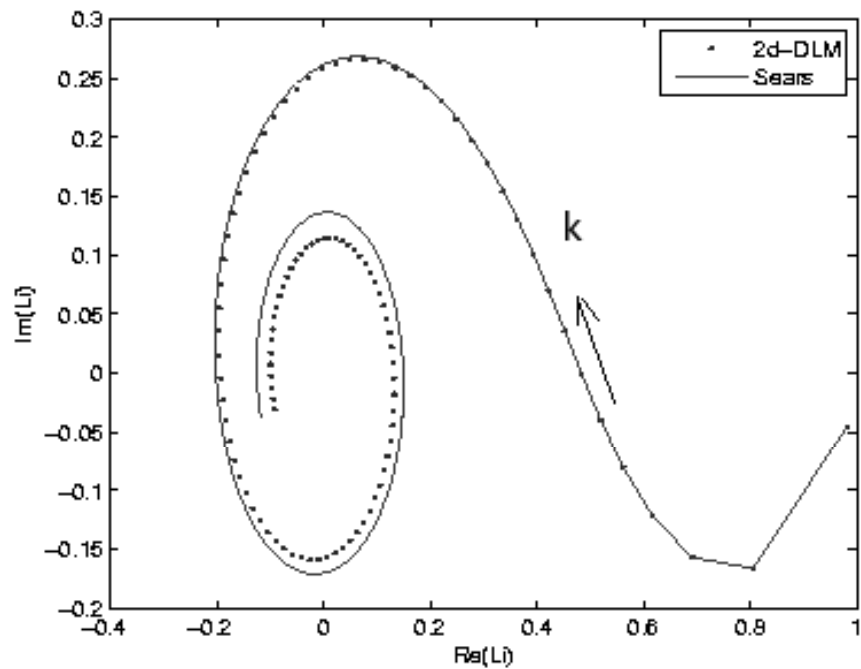


(b) Comparison of doublet lattice to Theodorsen results for  $n=100$  chord-wise divisions on airfoil

FIGURE 3.3: Plots of lift for  $n$  panels on airfoil due to plunging motion as  $k$  varies from 0.01 to 2.61 in increments of .1

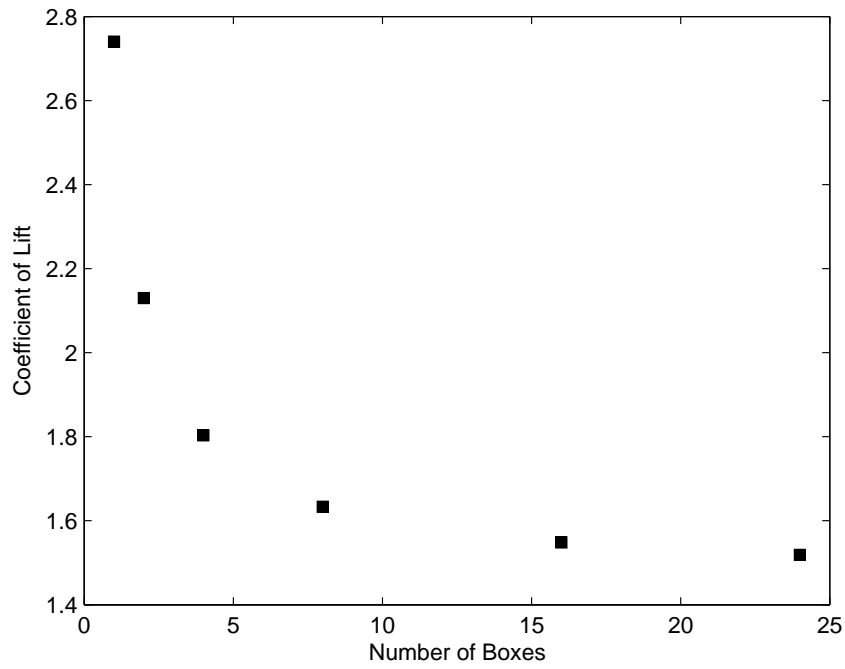


(a) Comparison of doublet lattice to Sears results for  $n=10$  chordwise divisions

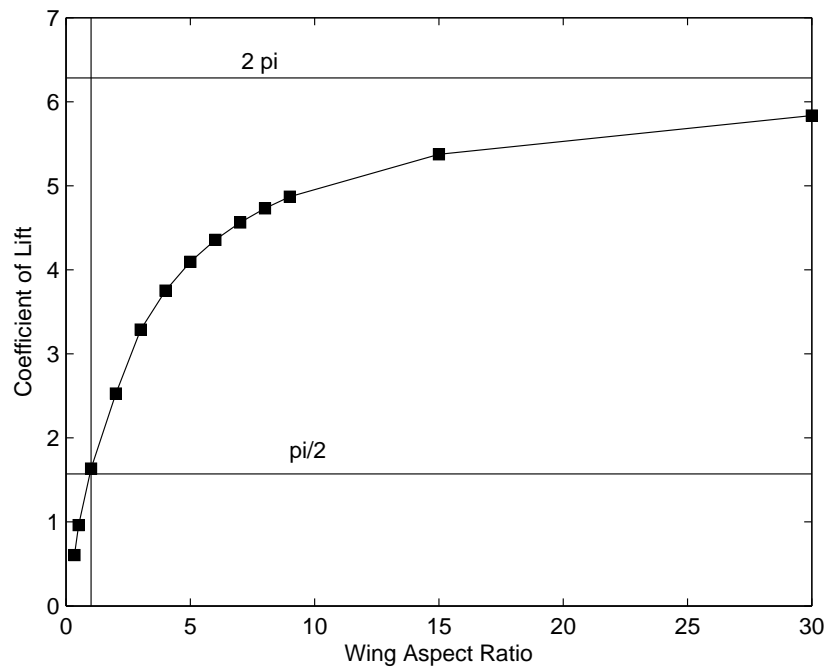


(b) Comparison of doublet lattice to Sears results for  $n=100$  chordwise divisions on airfoil

FIGURE 3.4: Plot of lift for  $n$  panels on airfoil due to gust response as  $k$  varies from 0.01 to 2.61 in increments of 0.1



(a) Coefficient of lift vs number of boxes for wing with AR=1



(b) Coefficient of lift vs wing aspect ratio

FIGURE 3.5: Coefficient of lift vs number of boxes for a wing AR=1 and also wing aspect ratio

For steady flow, the DLM is an approximation in comparison to the vortex lattice method(VLM) which is an exact solution. Therefore, Rodden suggests that the steady portion of the kernel calculated by the DLM should be subtracted and replaced with the VLM [43] contribution [29]. In works by Rodden and et. al [29, 39, 40], the steady portion calculated using the DLM was substituted with the calculations from the vortex lattice method when using either the parabolic or quartic approximation. The quartic approximation without Rodden’s well noted substitution is used in this work in the steady( $k = 0$ ) flow analysis for the wing in the National Advisory Committee for Aeronautics(NACA) RMA51G31 with an aspect ratio=3.0, sweep angle of  $45^\circ$ ,  $M = 0.8$ , and  $\alpha = 4^\circ$  in Fig.3.6 in reproducing the results in Fig. 3.7.

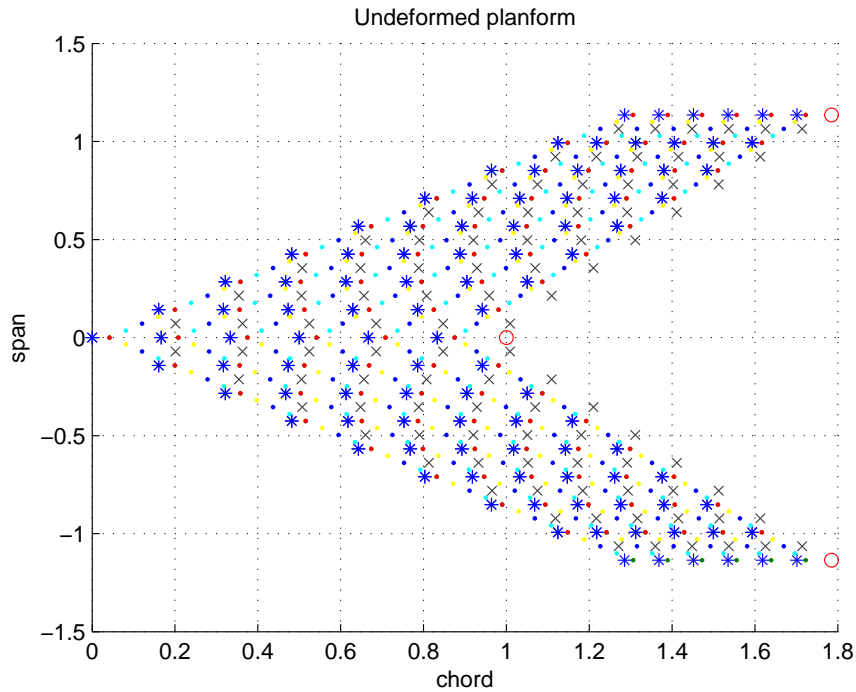
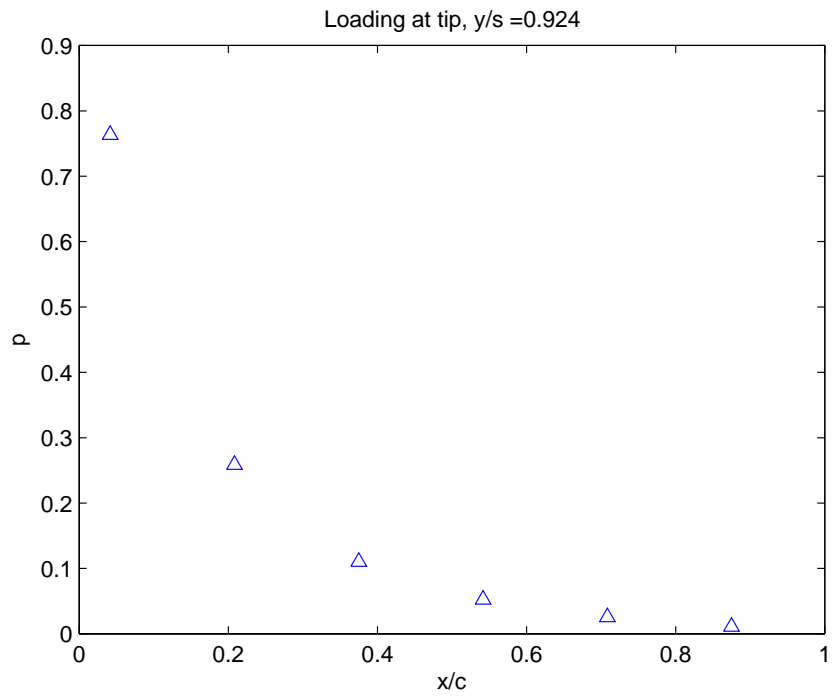
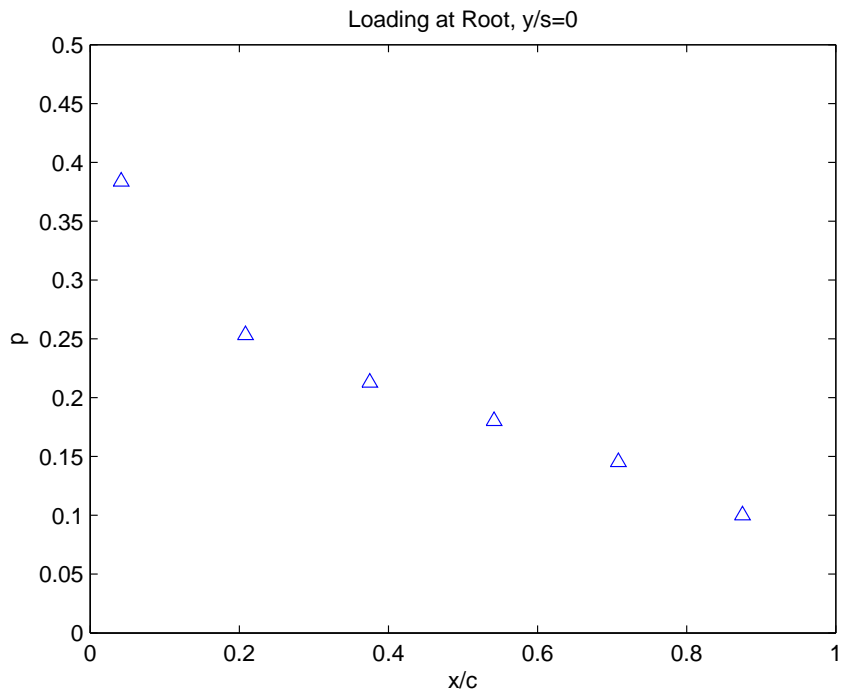


FIGURE 3.6: Geometry with Prandtl Glaurent transformation on swept wing in steady flow( $k=0$ )



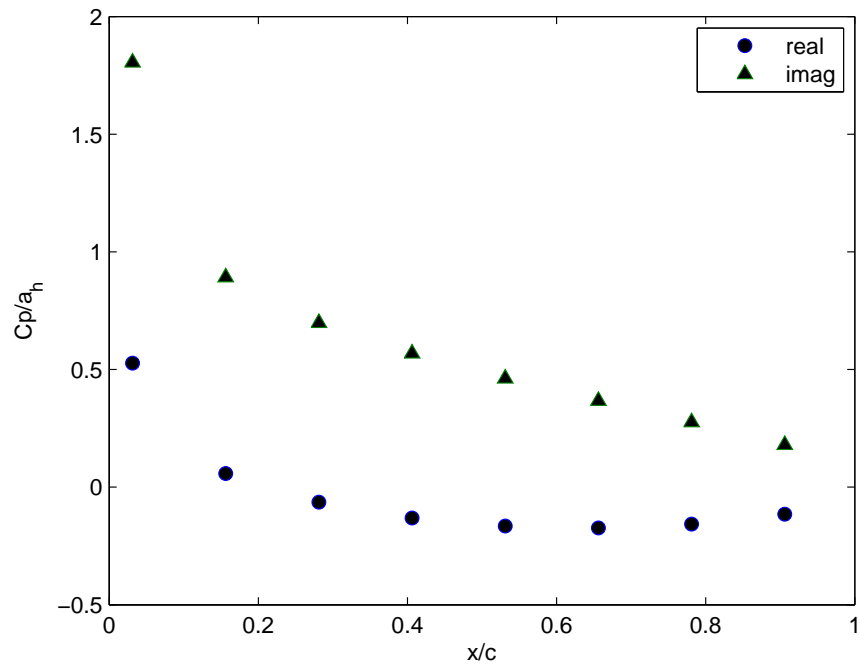
(a) Loading at tip,  $y/s=0.924$



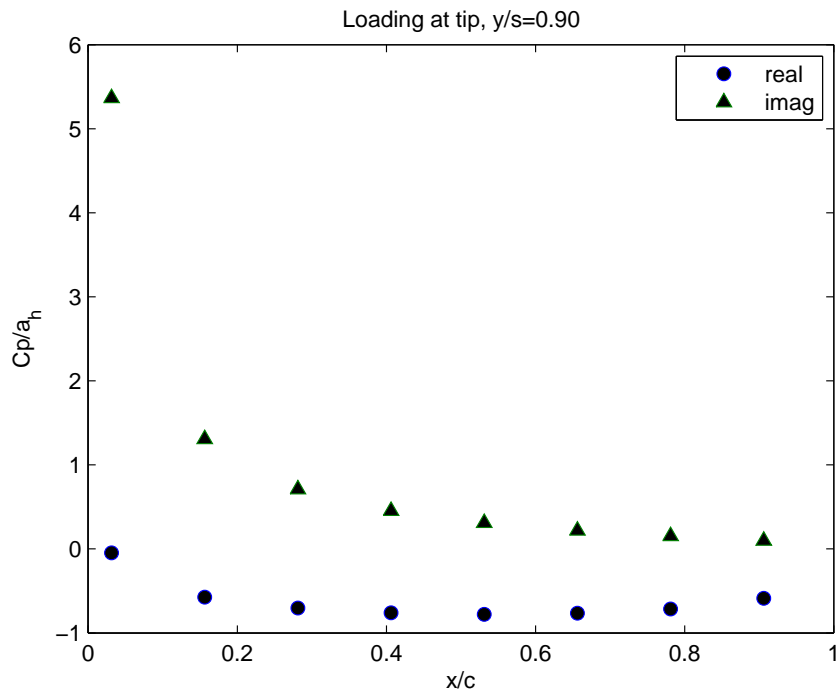
(b) Loading at root,  $y/s=0.0$

FIGURE 3.7: Lift distribution on swept wing in Fig. 3.6 in steady flow ( $k=0$ )

The quartic approximation is used for analyzing a rectangular wing with an aspect ratio equal to 3.0 oscillating in a bending mode described by  $\bar{h} \approx 0.18043|(y/s)| + 1.70255(y/s)^2 - 1.13688|(y/s)^3| + 0.25387(y/s)^4$  and the results are shown in Fig. 3.8. The results in Fig. 3.8 produced using the quartic approximation are identical to the results in Figs. 5 and 7, respectively, from Rodden's paper in 1969 [29] where the substitution with the VLM was used. Reproducing the results of Rodden, is proof that the DLM method is implemented correctly and using the quartic approximation without the substitution is valid.



(a) Loading at root,  $y/s=0.0$



(b) Loading at tip,  $y/s=0.9$

FIGURE 3.8: Lift distribution on rectangular wing ( $AR=3$ ) oscillating in bending mode in compressible ( $M = 0.24$ ) and unsteady ( $k = 0.47$ ) flow

### 3.5 Conclusions

The doublet lattice method is implemented correctly despite not using the recommendation of the original authors Drs. Rodden and Albano to add the steady portion computed using the vortex lattice method after subtracting the computed steady portion by the DLM. The DLM is able to reproduce the classical aerodynamic results according to Sears and Theodorsen for the gust and plunging problem, respectively. One of the important rules of using the doublet lattice method, is in regards to understanding the aspect ratio of each panel. In the original DLM, a parabolic approximation is used to compute  $I_1$  in Eqn. 3.25 and the aspect ratio of each panel is required to be between one and three to yield good results. The improved DLM uses a quartic approximation to compute  $I_1$  in Eqn. 3.25. The aspect ratio of each panel can be relaxed to be between one and five to yield good results. The approximation breaks down as the box becomes larger. However, what is more important here is that the quartic approximation is nearly equal to the vortex lattice method in steady flow. This allows the doublet lattice method to be used exclusively in determining the aerodynamic loading. In addition to reproducing the classical results, the DLM with the quartic approximation reproduces the 3-d results found by Drs. Rodden and Albano in 1969 paper[29].

The doublet lattice method is a powerful tool for calculating the aerodynamic forces in subsonic, unsteady, compressible flow. The doublet lattice method is available in MSC<sup>TM</sup> NASTRAN, a commercial code. The implementation of DLM using code written in house provided a lot of understanding. Understanding every approximation is important, in particular when computing the  $I_1$  in Eqn. 3.25. In using MSC NASTRAN<sup>TM</sup>, a typical user may or may not be fully aware of why their results will not agree close to theory when pursuing the analysis of the wing with hole. For example the steady flow component used in the “box” code probably uses the vortex

lattice method and in the case of a hole the underlying theory for the vortex lattice method would be violated.

# 4

## Theoretical and Experimental Aerodynamic Studies of a Wing with Hole

A novel approach to calculating the aerodynamics of a lifting surface with a hole is explored using the doublet lattice method. Preliminary experimental aerodynamic studies were conducted on a wing with a hole to determine the effectiveness of the doublet lattice method(DLM) in predicting aerodynamic pressure distributions. During those preliminary wind tunnel tests, several anomalies were observed in the test data. Those issues are addressed in a new and improved wind tunnel test model. The major differences in this model and the previous model are (1) the use of curved surfaces on the edges of the hole and (2) the duct work for the pressure lines is now internal to the wing. Further, the apparatus for measuring the pressures was improved.

### 4.1 Aerodynamical theoretical modeling of a wing with a hole

The wing can be divided into a portion with and without a hole. The aerodynamic influence coefficient matrix(AICM) can be partitioned over the wing portion with and with out a hole. The two unknowns in this problem are the pressure jump on

the wing without the hole and the downwash on the wing with the hole. The pressure jump in the hole is of course zero. The downwash on the wing portion without a hole is known. In determining the pressure over the portion of the wing surrounding the hole, all that is needed is to set the pressure to zero in the hole, see Appendix. The downwash and AICM are known, so its simply takes a matrix inversion to determine the unknown pressures.

The pressure jump is proportional to the local doublet strength, so in the hole and the wake, the doublet strength is zero. Modeling wing aerodynamics with a hole required setting the equations of doublets in the hole equal to zero. A “trick” to making these substitutions easier computationally is to set  $\bar{p} = 0$ , since it is the same as not having any elements there at all. Initially, the aerodynamic influence coefficient matrix(AICM) is computed for a wing without a hole using the doublet lattice method. The panels where the holes are located, affects the AICM and the downwash. If the hole is on the  $i^{th}$  panel, then zeros are placed on  $i^{th}$  row except on the diagonal of the AICM. On the diagonal, a one is placed there on the  $i^{th}$  row. Further, to get  $\bar{p} = 0$  in the  $i^{th}$  row of the downwash vector, a zero is placed there. See Eqn. 4.1

$$\bar{w}_i = \sum_{j=1}^n D_{ij} \bar{p}_j$$

$$\begin{pmatrix} w_1 \\ 0 \\ \vdots \\ w_{n-1} \\ w_n \end{pmatrix} = \begin{bmatrix} D_{11} & D_{12} & \cdots & D_{1(n-1)} & D_{1n} \\ 0 & 1 & 0 & 0 & 0 \\ \cdots & \cdots & \cdots & \cdots & \cdots \\ \vdots & \vdots & \vdots & \vdots & \vdots \\ D_{n1} & & \cdots & & D_{nn} \end{bmatrix} \times \begin{pmatrix} p_1 \\ p_2 \\ \vdots \\ p_{n-1} \\ p_n \end{pmatrix} \quad (4.1)$$

The aerodynamics of the hole in the wing has several effects and they depend

on the hole's size and location. Of course, the overall lift on the wing will be decreased with the addition of the hole. If the hole is small, the effects are small and vice versa. From theoretical analysis, only holes larger than 10% of the total wing area have noticeable changes in the aerodynamic forces. A hole placement in the chordwise direction is more important at the leading edge and trailing edge, but less important in the middle portion of the chord. The pressure plotted over the hole in the chordwise direction agrees well with theory in that a square root singularity occurs at the trailing edge of the hole(leading edge of the following wing portion).

Thinking about the aerodynamics in term of vortices temporarily instead of doublets, the trailing vortices coming off the wing portion in front of the hole have an influence on the wing portion behind the hole since it effects the freestream velocity and thus the angle of attack. Investigating the significance of this effect experimentally and theoretically is important to determine if the approximations used are adequate for a rectangular wing before proceeding to aeroelastic studies.

The aerodynamic theory with the imposed “trick” is used to design an experiment tested in the Duke University Low Speed Wind Tunnel. The theory includes using the doublet lattice method and the method of images. The method of images is used to incorporate the effect of the floor since it could not be assumed to be infinitely far away like the other walls of the tunnel. The far field boundary condition used in the developing the theory for DLM would be violated if the method of images is not used. If the remaining walls are assumed to be in close proximity to the wing then each wall would have to be incorporated using the method of images. The image system for a closed rectangular tunnel that represents the Duke wind tunnel would be infinite and image systems of this type are not always valid [44]. Two alternative approaches to account for the wall interferences include using a wall correction factor[38] or to use the nonplanar version of the doublet lattice method [29, 39, 40].

## 4.2 Aerodynamic experimental investigations of a wing with hole

### 4.2.1 *Experimental apparatus for a wing with hole*

The wing model is designed in SolidWorks™ and machined using computer numerical control(CNC) out of two 0.16” aircraft grade aluminum plates. The two halves are designed so the wing is symmetric when assembled. The chord of the wing is 12 inches and the span is 9.6 inches. The pressure on each port is collected using an intricately design configuration of individual tubes. The individual tubes are connected to the upper and lower surface to record the pressure jump(difference) across the surface. The pressure differences across the surface of the wing and the dynamic pressure from the pitot-static tube are measured using a 24-port wafer Scanivalve™ W1266/1P-24T connected to a Validyne™ DP15-24 differential pressure transducer. The results from the pressure transducer are read on a Validyne™ CD23 digital transducer.

The model is securely mounted to a rotary table that is calibrated in degrees, minutes, and seconds. The main reference at zero degrees angle of attack( $\alpha = 0^\circ$ ) is determined experimentally because the pressure difference theoretically equals zero for a symmetric airfoil. After determining  $\alpha = 0^\circ$  the floor is marked at  $\pm 2^\circ$ ,  $\pm 5^\circ$ ,  $\pm 8^\circ$ , and  $\pm 10^\circ$ . At these positions, the rotary table is marked so the experiment could be repeated.

The model is tested in a recirculating wind tunnel which has a cross section measuring 28 inches wide and 21 inches tall. The air density in the wind tunnel is  $1.225 \text{ kg/m}^3$ . The wind tunnel operates during testing in a flow velocity range between 11-13 m/s which corresponds to a dynamic pressure range between 74.11-103.5 Pa for all ports. In order to accurately determine  $\bar{p} = \Delta C_p$ , the dynamic pressure was measured at the beginning and end of each test at every angle of attack, to account for changes in the flow velocity over time as the pressure difference was measured across the surface. The flow velocity changes as time elapse because currently there

is not a feedback mechanism on the wind tunnel's motor to readjust the voltage as the flow velocity increases. Observing the changes in dynamic pressures increases the accuracy of the results when comparing theory to experiment. Further, to verify that the pressure ports are working correctly, the pressure differences are measured at  $U_\infty=0$  m/s to insure the readings are equal to zero or nearly zero. A few ports did not equal zero, and this is an indication that a few ports are working improperly. The ports that are not working properly are indicated by a plus or square symbol.

#### *4.2.2 Results from the wind tunnel investigations of wing with hole*

Linear theory predicts  $\Delta C_p$  for the  $\pm$  of any angle of attack for a symmetric airfoil(2-d) or wing(3-d), should be equal in magnitude and opposite in sign. In Figs. 4.2-4.23, the results are shown in the chordwise and spanwise directions for the model in Fig. 4.1 at  $0^\circ$ ,  $\pm 2^\circ$ ,  $\pm 5^\circ$ ,  $\pm 8^\circ$ , and  $\pm 10^\circ$ . The model is tested with the hole but an insert is installed to establish a baseline for the experiment. The insert used during testing is made out of two pieces of aluminum that are 0.16" thick and designed to fill the hole. The two plates are bolted together to be held in place. Any discontinuous surfaces are removed using plumber's putty.

The results for the aerodynamic pressure distribution along the chord in Figs. 4.2-4.11 are for the model with a hole and also for the model with an insert installed to cover the hole at  $y/s = 0.125$  and  $y/s = 0.458$ . The agreement between theory using the doublet lattice method and the experiments is good for the model with the hole. The agreement between the theory and experiment for the case with an insert installed is not as good aft of the insert in Figs. 4.2-4.11. The results shown in Figs. 4.6 and 4.11, however, suggest that the linear aerodynamic theory as embodied by the doublet lattice method breaks down at the higher angles of attack.

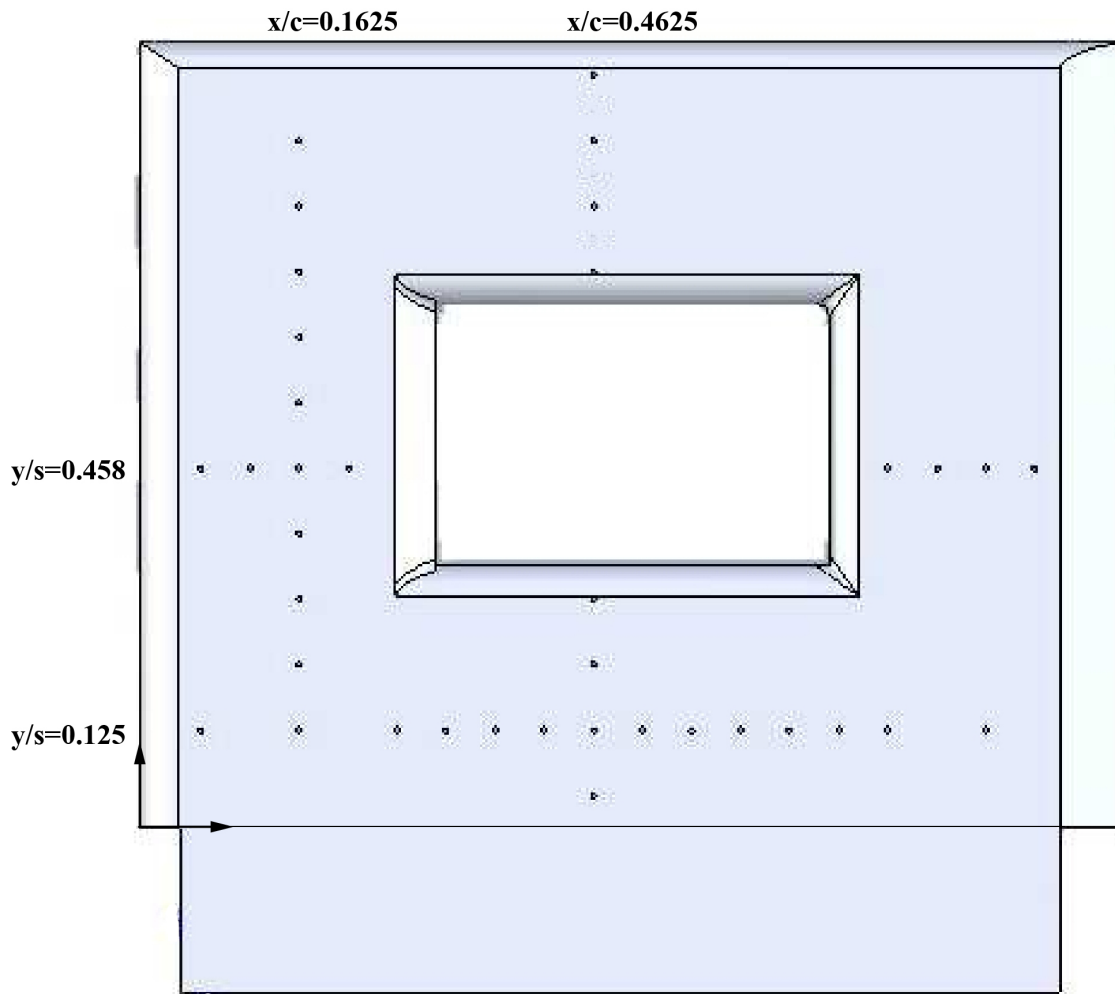
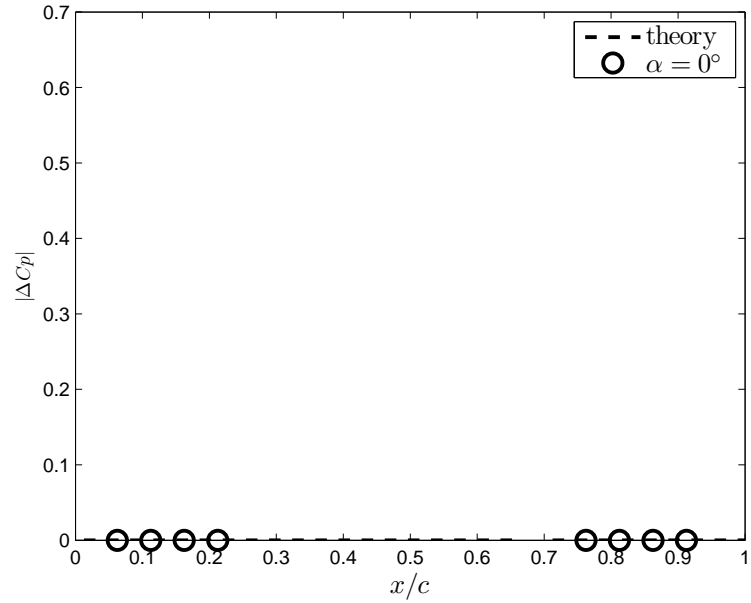
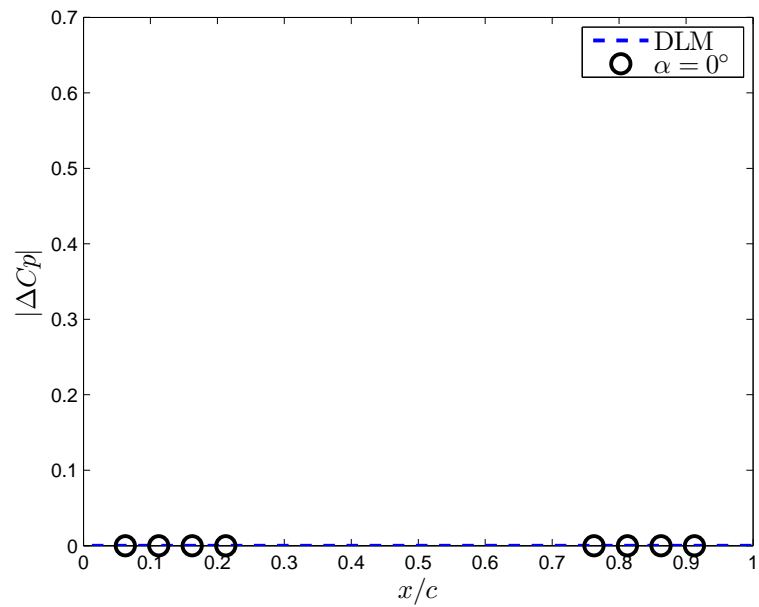


FIGURE 4.1: SolidWorks™ of wing model with the pressure ports. The chord is 12 inches and span is 9.6 inches.

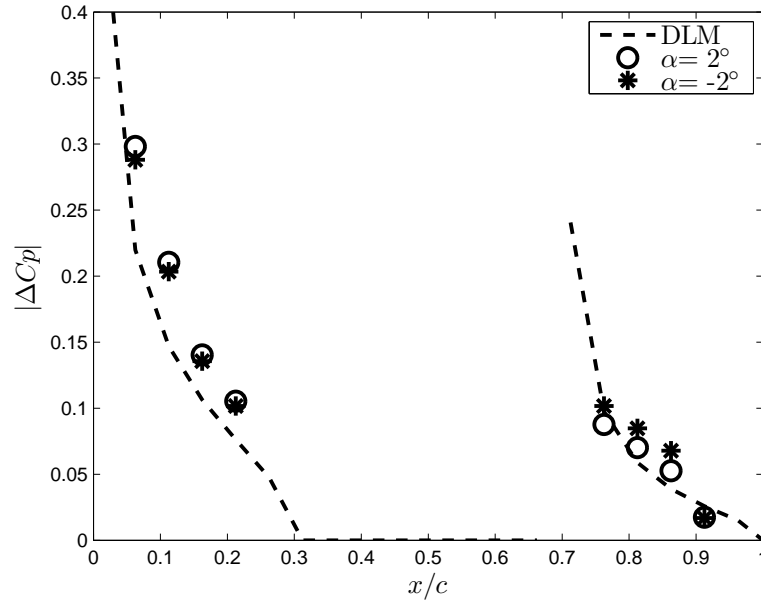


(a)  $y/s=0.458$ ,  $\alpha = 0^\circ$ , hole

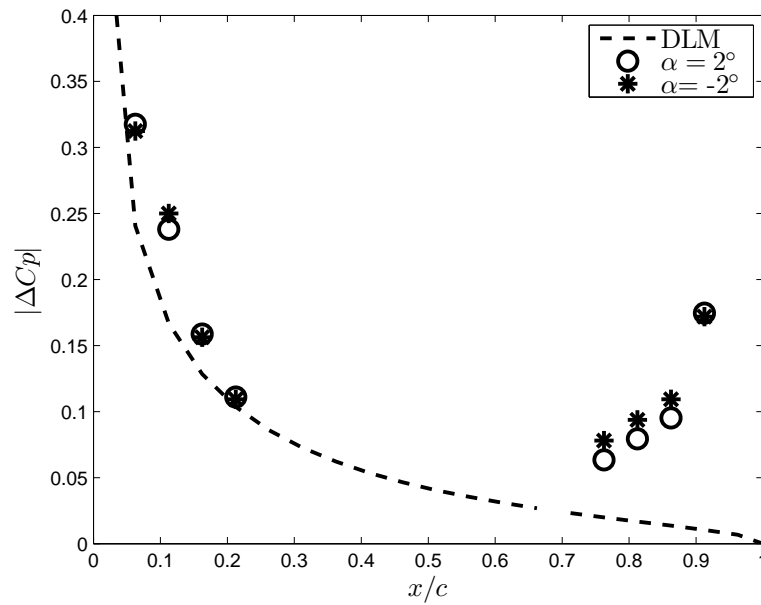


(b)  $y/s=0.458$ ,  $\alpha = 0^\circ$ , insert no. 1

FIGURE 4.2: The magnitude of the theoretical and experimental  $\Delta C_p$  versus chordwise position,  $x/c$ , at  $y/s = 0.458$ .  $\alpha = 0^\circ$ .

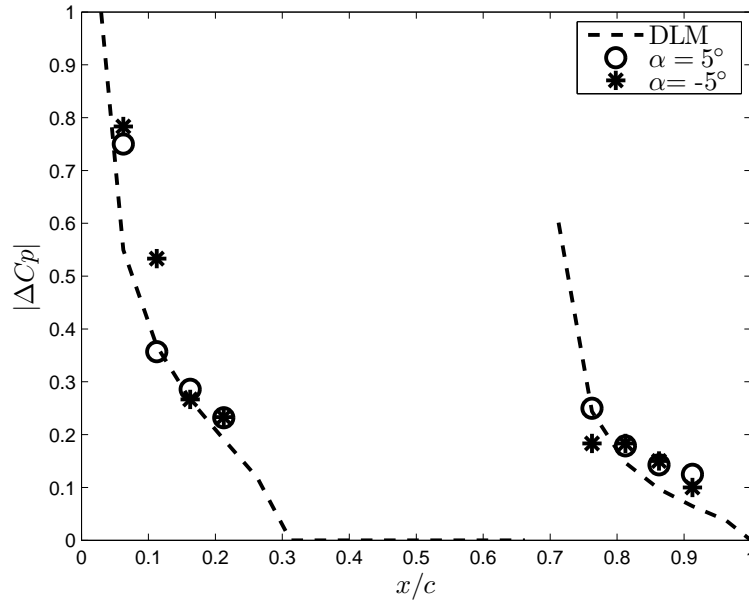


(a)  $y/s=0.458$ ,  $\alpha = 2^\circ$ , hole

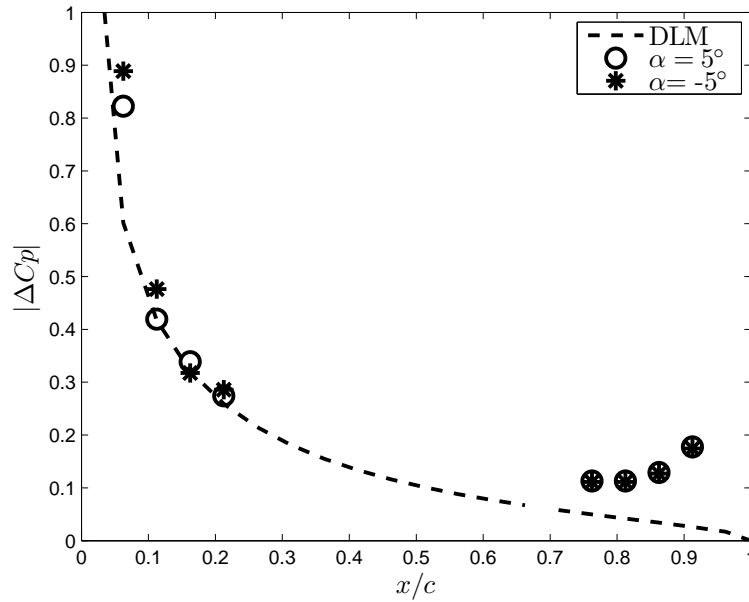


(b)  $y/s=0.458$ ,  $\alpha = 2^\circ$ , insert no. 1

FIGURE 4.3: The magnitude of the theoretical and experimental  $\Delta C_p$  versus chord-wise position,  $x/c$ , at  $y/s = 0.458$ .  $\alpha = 2^\circ$ .

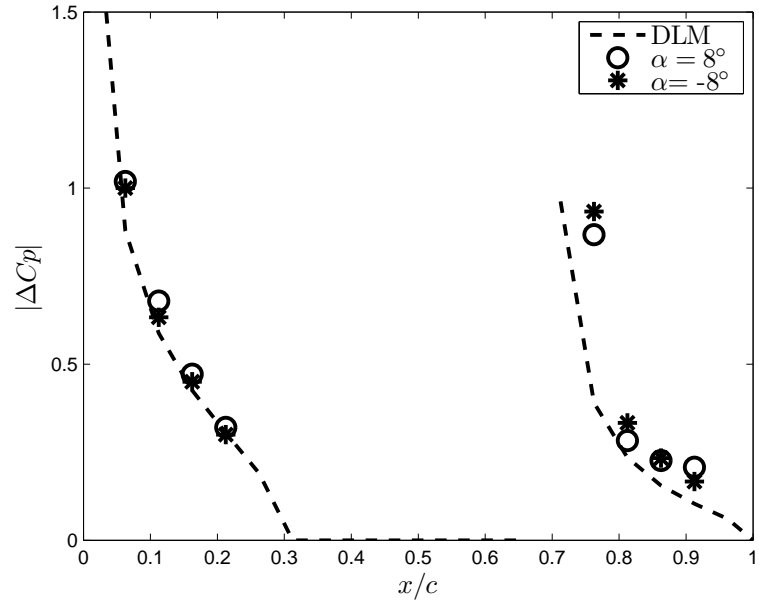


(a)  $y/s=0.458$ ,  $\alpha = 5^\circ$ , hole

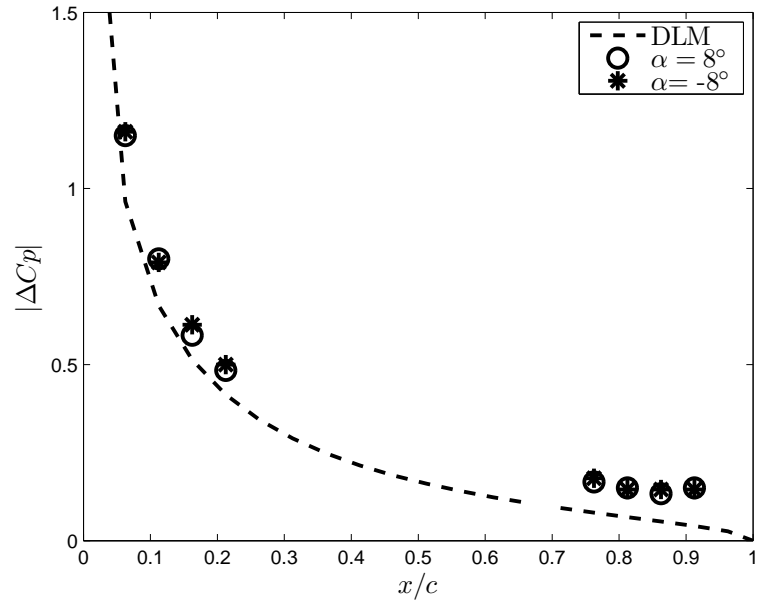


(b)  $y/s=0.458$ ,  $\alpha = 5^\circ$ , insert no. 1

FIGURE 4.4: The magnitude of the theoretical and experimental  $\Delta C_p$  versus chord-wise position,  $x/c$ , at  $y/s = 0.458$ .  $\alpha = 5^\circ$ .

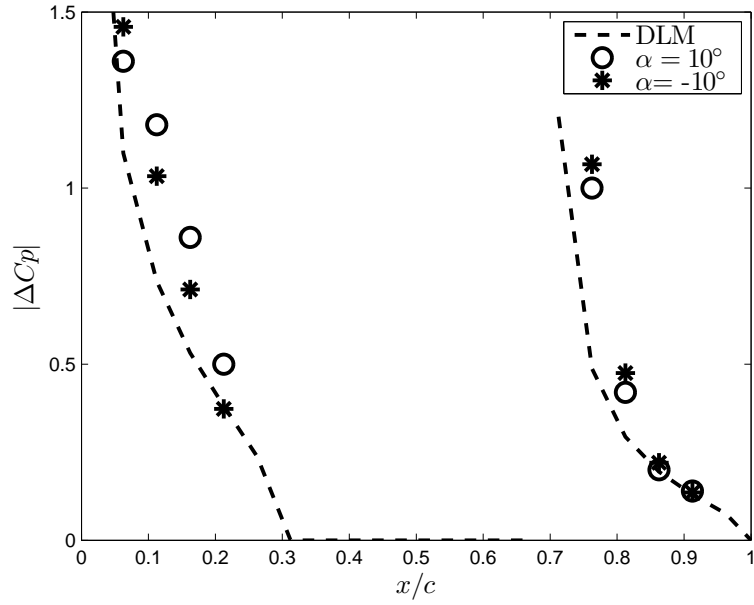


(a)  $y/s=0.458$ ,  $\alpha = 8^\circ$ , hole

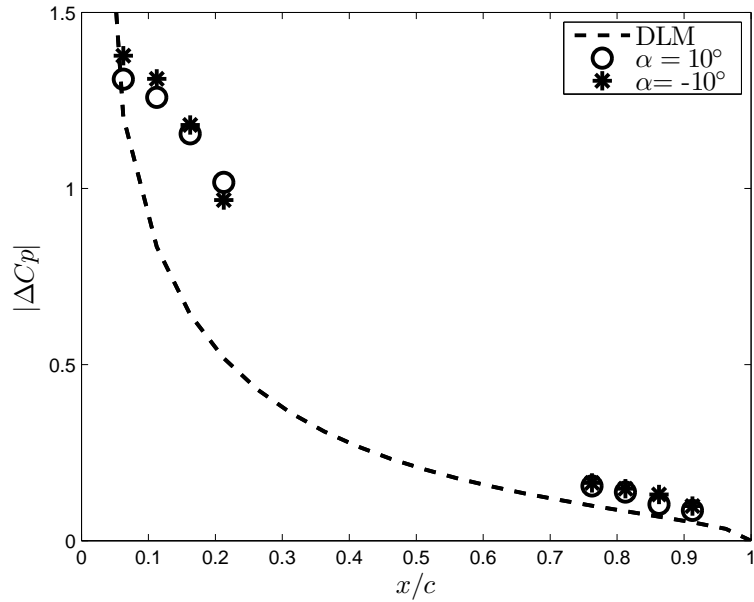


(b)  $y/s=0.458$ ,  $\alpha = 8^\circ$ , insert no. 1

FIGURE 4.5: The magnitude of the theoretical and experimental  $\Delta C_p$  versus chord-wise position,  $x/c$ , at  $y/s = 0.458$ .  $\alpha = 8^\circ$ .

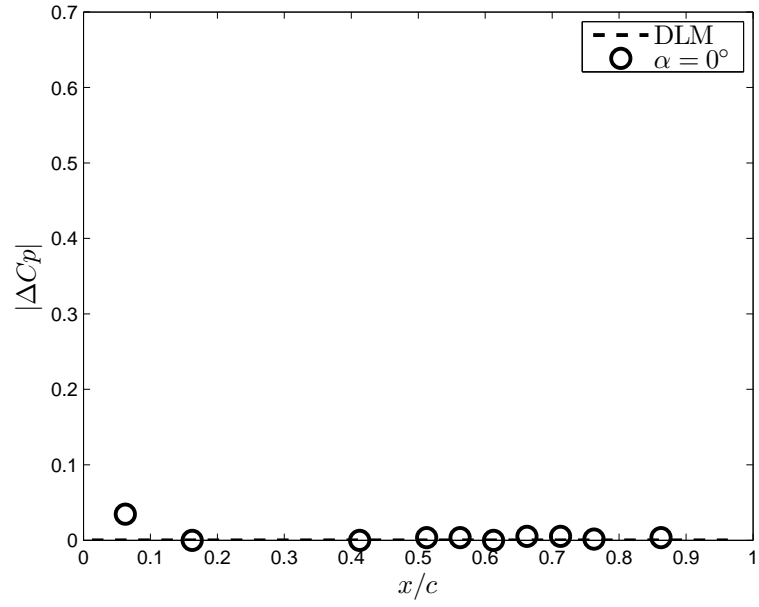


(a)  $y/s=0.458$ ,  $\alpha = 10^\circ$ , hole

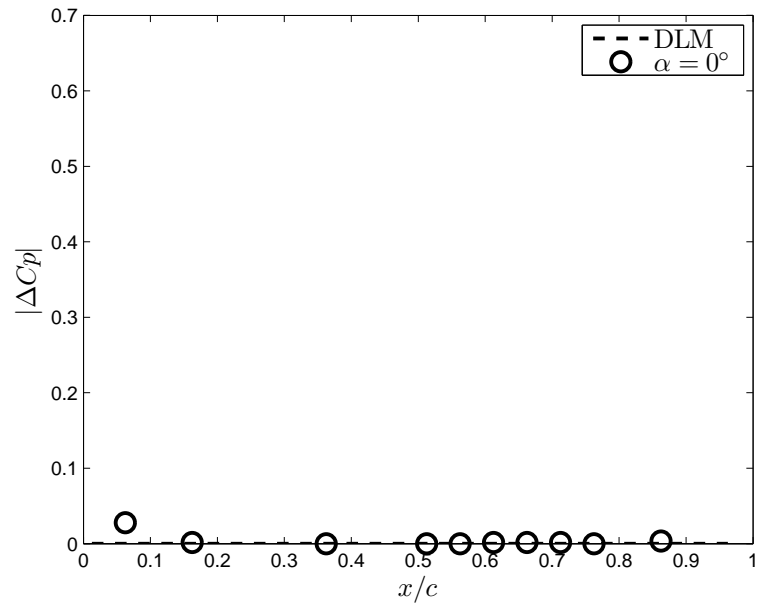


(b)  $y/s=0.458$ ,  $\alpha = 10^\circ$ , insert no. 1

FIGURE 4.6: The magnitude of the theoretical and experimental  $\Delta C_p$  versus chordwise position,  $x/c$ , at  $y/s = 0.458$ .  $\alpha = 10^\circ$ .

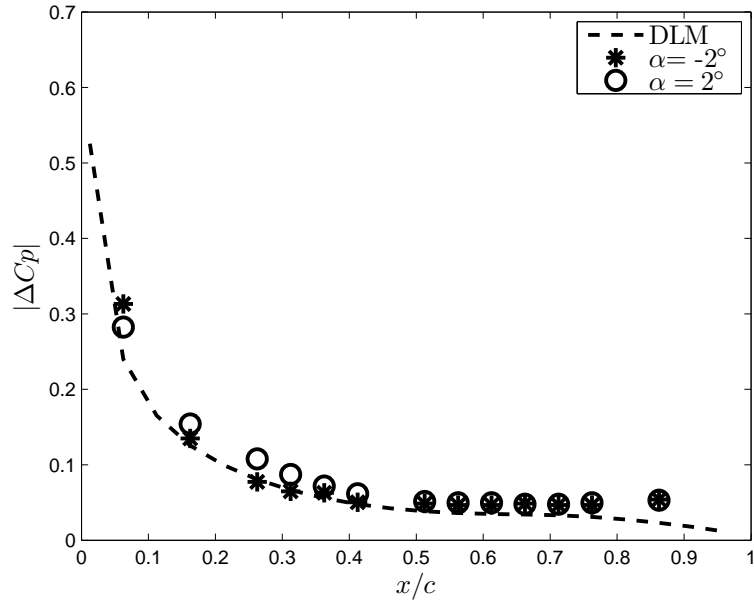


(a)  $y/s=0.125$ ,  $\alpha = 0^\circ$ , hole

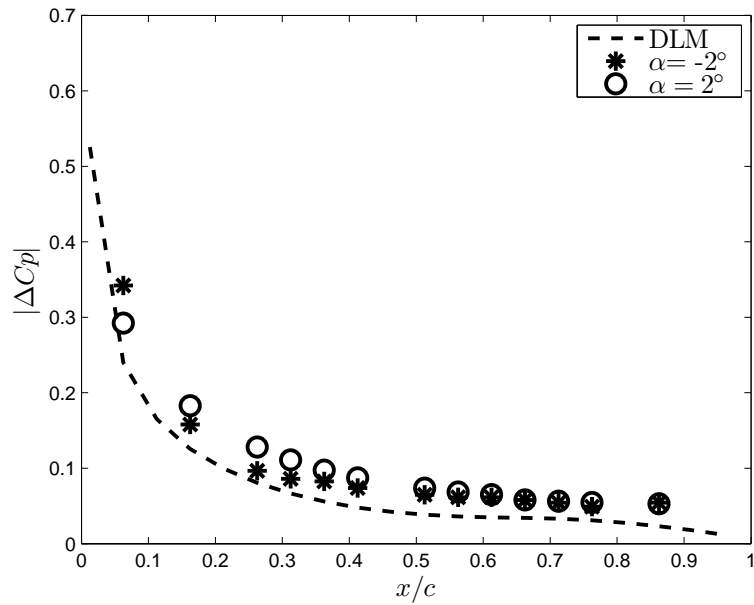


(b)  $y/s=0.125$ ,  $\alpha = 0^\circ$ , insert no. 1

FIGURE 4.7: The magnitude of the theoretical and experimental  $\Delta C_p$  versus chordwise position,  $x/c$ , at  $y/s = 0.125$ .  $\alpha = 0^\circ$ .

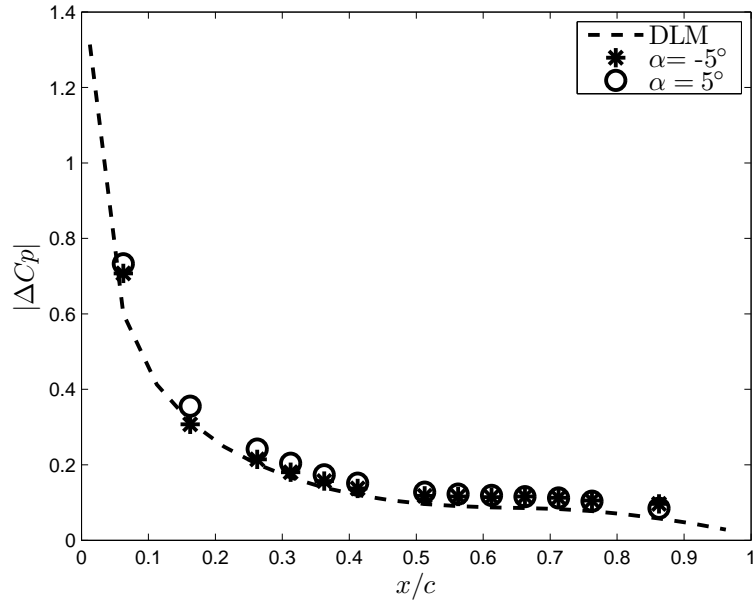


(a)  $y/s=0.125$ ,  $\alpha = 2^\circ$ , hole

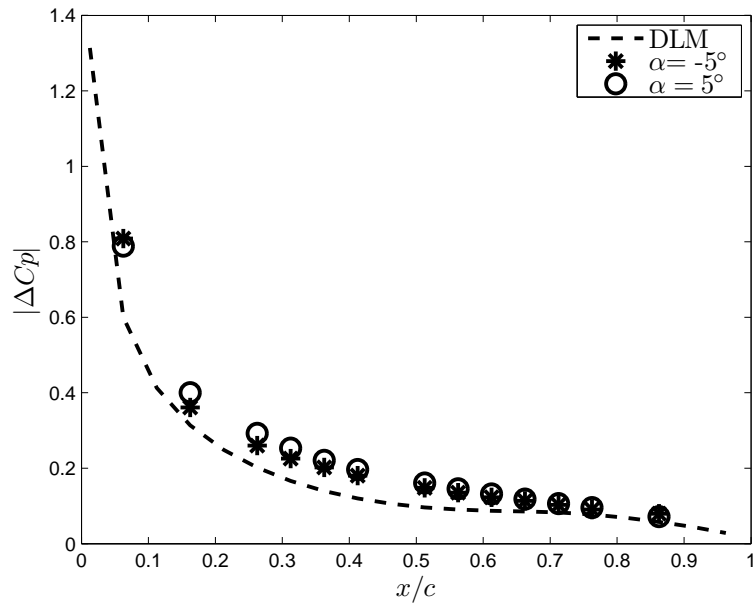


(b)  $y/s=0.125$ ,  $\alpha = 2^\circ$ , insert no. 1

FIGURE 4.8: The magnitude of the theoretical and experimental  $\Delta C_p$  versus chord-wise position,  $x/c$ , at  $y/s = 0.125$ .  $\alpha = 2^\circ$ .



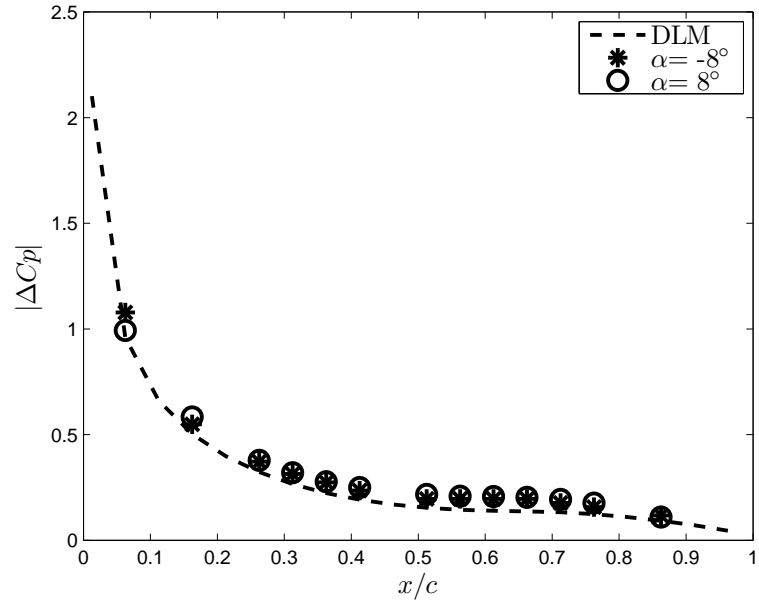
(a)  $y/s=0.125$ ,  $\alpha = 5^\circ$ , hole



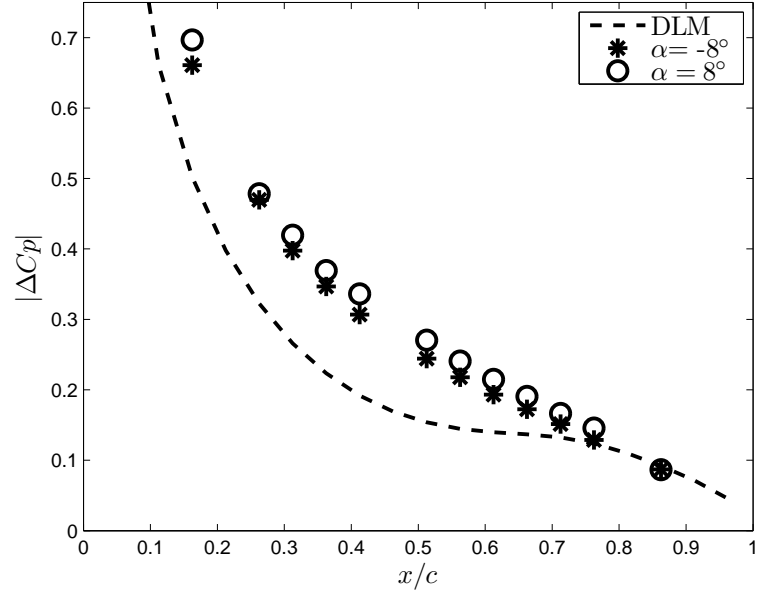
(b)  $y/s=0.125$ ,  $\alpha = 5^\circ$ , insert no. 1

FIGURE 4.9: The magnitude of the theoretical and experimental  $\Delta C_p$  versus chord-wise position,  $x/c$ , at  $y/s = 0.125$ .  $\alpha = 5^\circ$ .

The results for the aerodynamic pressure distribution along the span in Figs. 4.12-4.23 are for the model with a hole and also for the model with an insert installed to cover the hole at  $x/c = 0.1625$  and  $x/c = 0.4625$ . The coefficient of pressures measured along the spanwise direction agree fairly well at  $x/c = 0.1625$  and  $x/c = 0.4625$  except for a few spurious points near the tip as shown in Fig. 4.12. These spurious points are related to issues with the pressure ports. During all tests, the pressure differences were measured at  $U_\infty=0$  m/s to make sure the readings were approximately equal to zero. The spurious points are first noted in Figs. 4.12 and 4.18 by a different symbol, a circle, at  $U_\infty=0$  m/s. In Figs. 4.13-4.17, for pressure readings along the span these same spurious points are clearly seen. At  $x/c = 0.4625$  the theoretical and experimental results correlate reasonably well, but since the pressure differences are so small in this region, it is rather difficult to measure them experimentally.

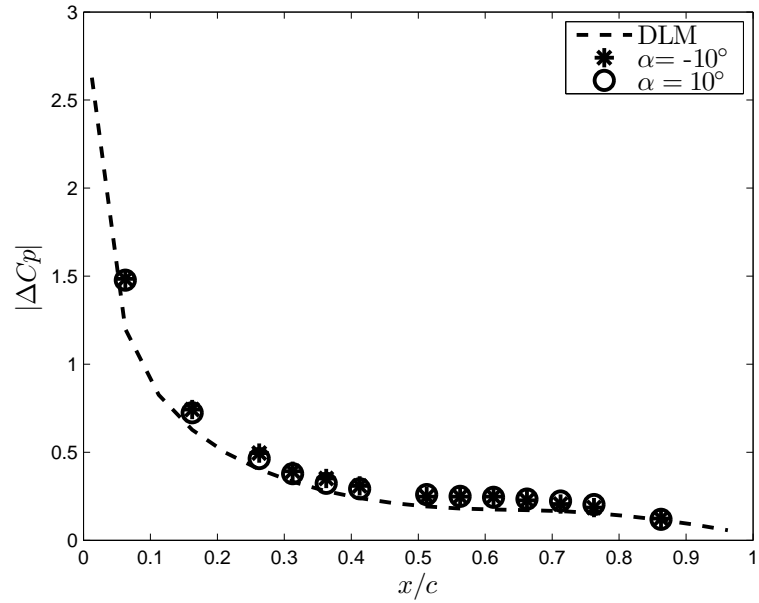


(a)  $y/s=0.125$ ,  $\alpha = 8^\circ$ , hole

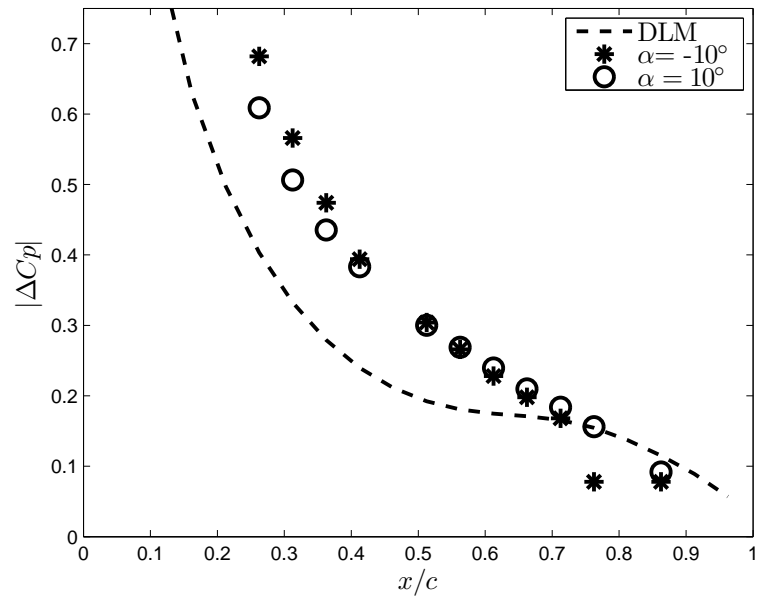


(b)  $y/s=0.125$ ,  $\alpha = 8^\circ$ , insert no. 1

FIGURE 4.10: The magnitude of the theoretical and experimental  $\Delta C_p$  versus chordwise position,  $x/c$ , at  $y/s = 0.125$ .  $\alpha = 8^\circ$ .



(a)  $y/s=0.125$ ,  $\alpha = 10^\circ$ , hole



(b)  $y/s=0.125$ ,  $\alpha = 10^\circ$ , insert no. 1

FIGURE 4.11: The magnitude of the theoretical and experimental  $\Delta C_p$  versus chordwise position,  $x/c$ , at  $y/s = 0.125$ .  $\alpha = 10^\circ$ .

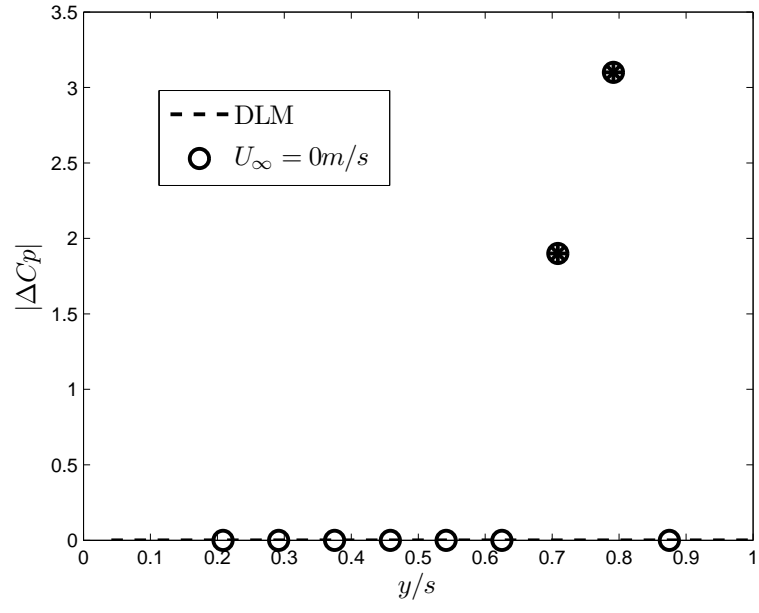
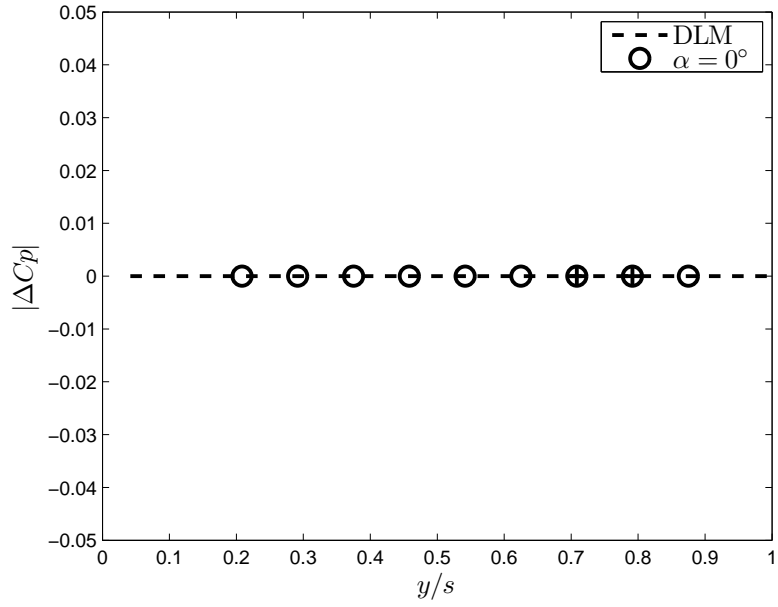
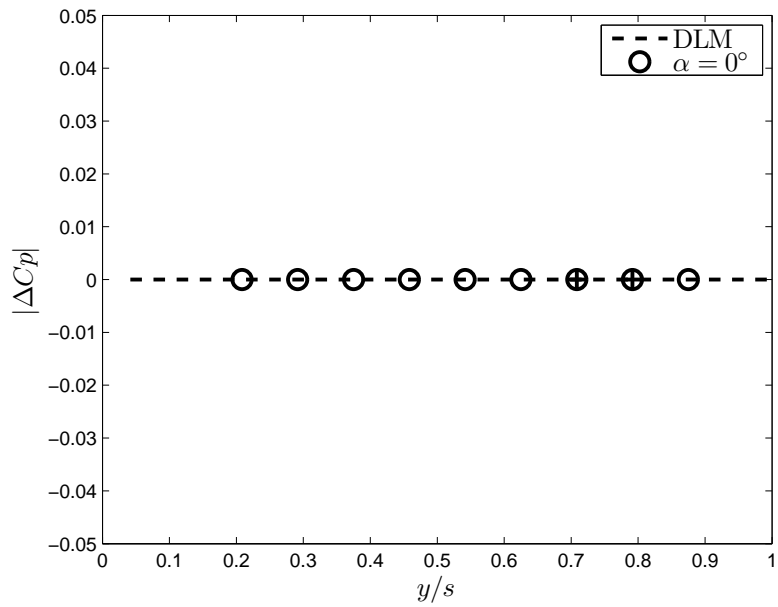


FIGURE 4.12: The magnitude of the theoretical and experimental  $\Delta C_p$  versus spanwise position,  $y/s$ , at  $U_\infty=0$  m/s and  $x/c = 0.1625$ .  $\alpha = 0^\circ$ .

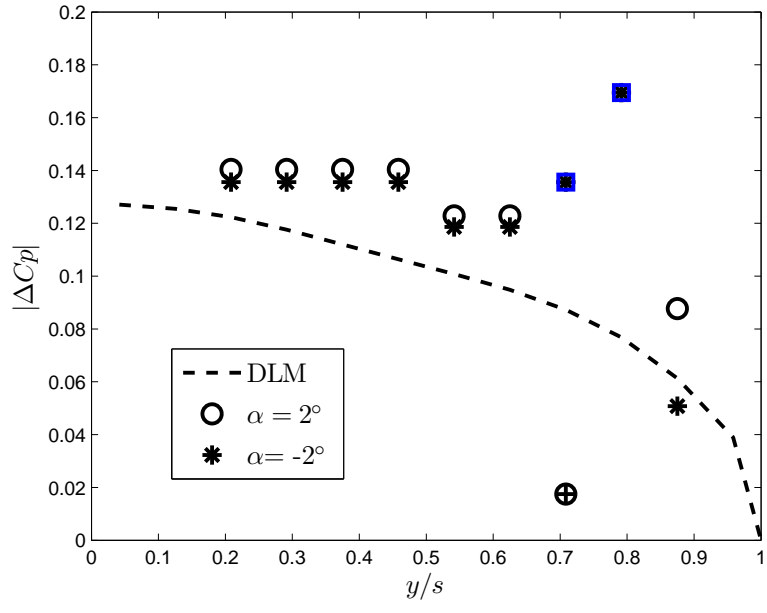


(a)  $x/c=0.1625$ ,  $\alpha = 0^\circ$ , hole

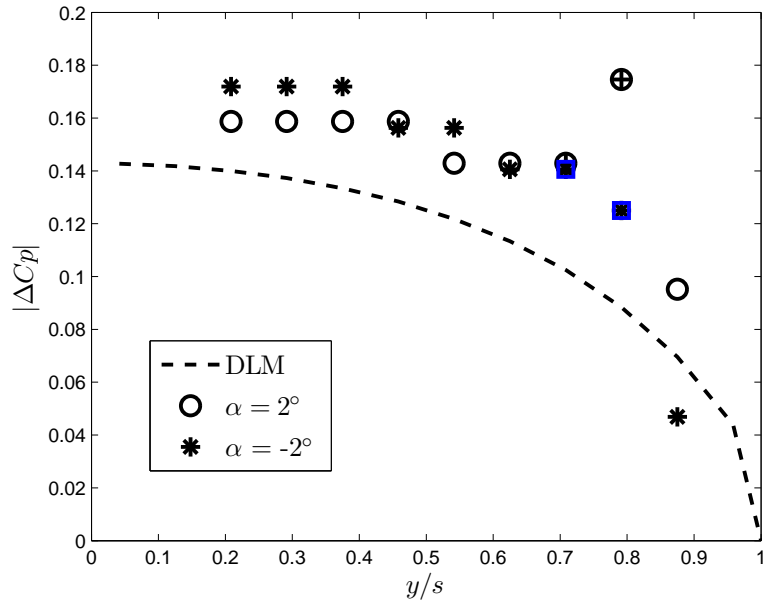


(b)  $x/c=0.1625$ ,  $\alpha = 0^\circ$ , insert no. 1

FIGURE 4.13: The magnitude of the theoretical and experimental  $\Delta C_p$  versus spanwise position,  $y/s$ , at  $x/c = 0.1625$ .  $\alpha = 0^\circ$ .

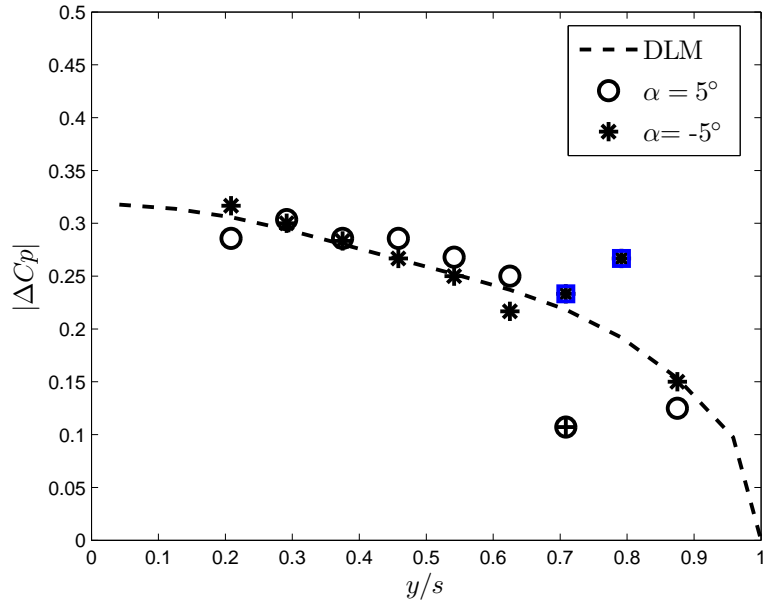


(a)  $x/c=0.1625$ ,  $\alpha = 2^\circ$ , hole

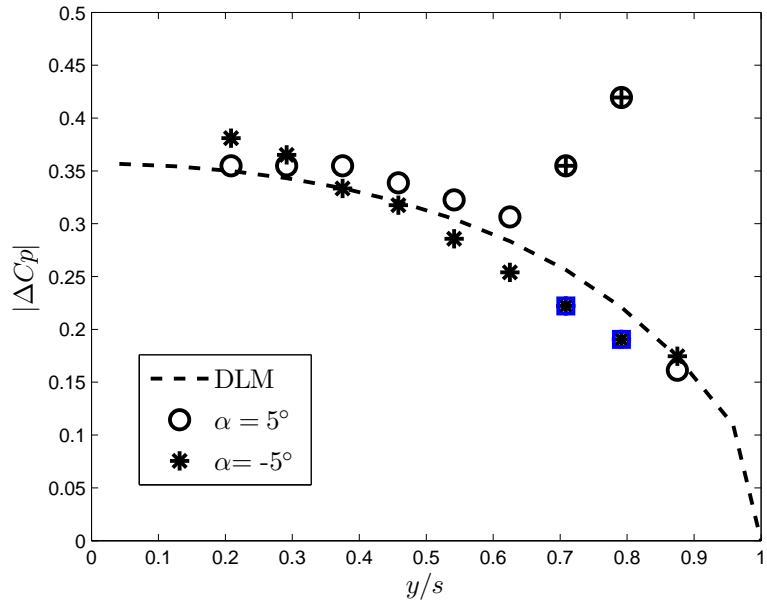


(b)  $x/c=0.1625$ ,  $\alpha = 2^\circ$ , insert no. 1

FIGURE 4.14: The magnitude of the theoretical and experimental  $\Delta C_p$  versus spanwise position,  $y/s$ , at  $x/c = 0.1625$ .  $\alpha = 2^\circ$ .

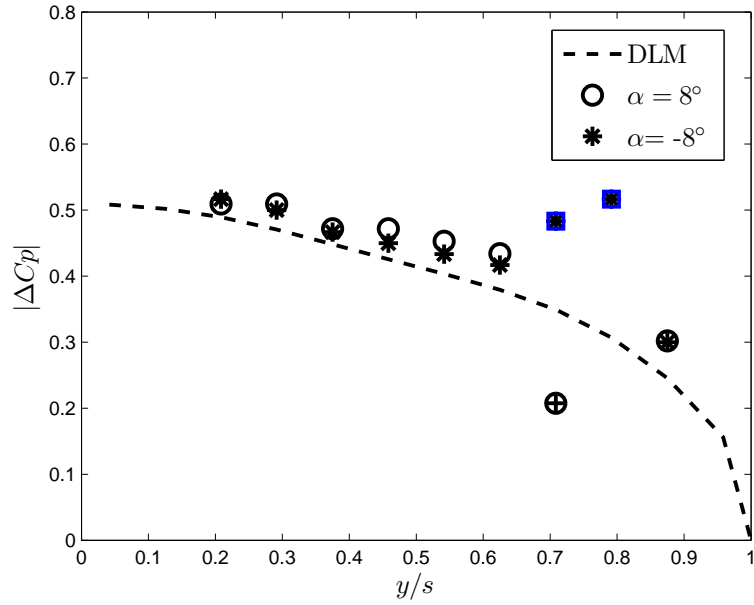


(a)  $x/c=0.1625$ ,  $\alpha = 5^\circ$ , hole

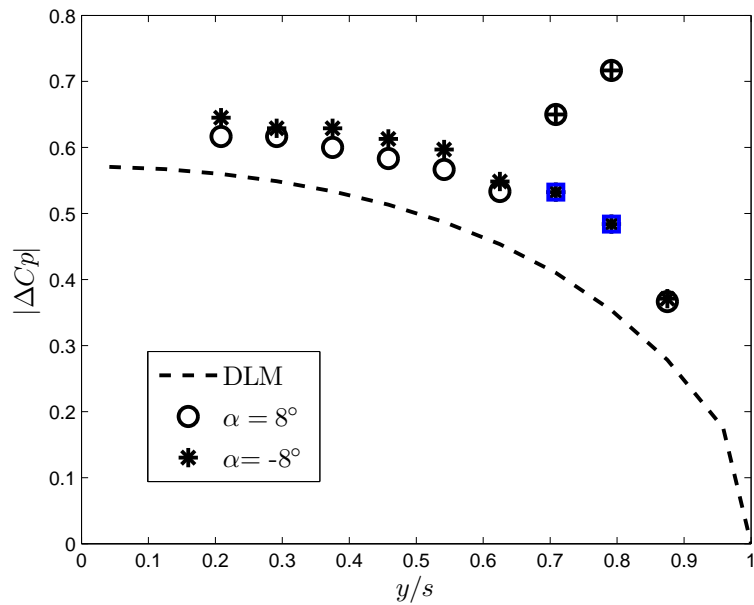


(b)  $x/c=0.1625$ ,  $\alpha = 5^\circ$ , insert no. 1

FIGURE 4.15: The magnitude of the theoretical and experimental  $\Delta C_p$  versus spanwise position,  $y/s$ , at  $x/c = 0.1625$ .  $\alpha = 5^\circ$ .

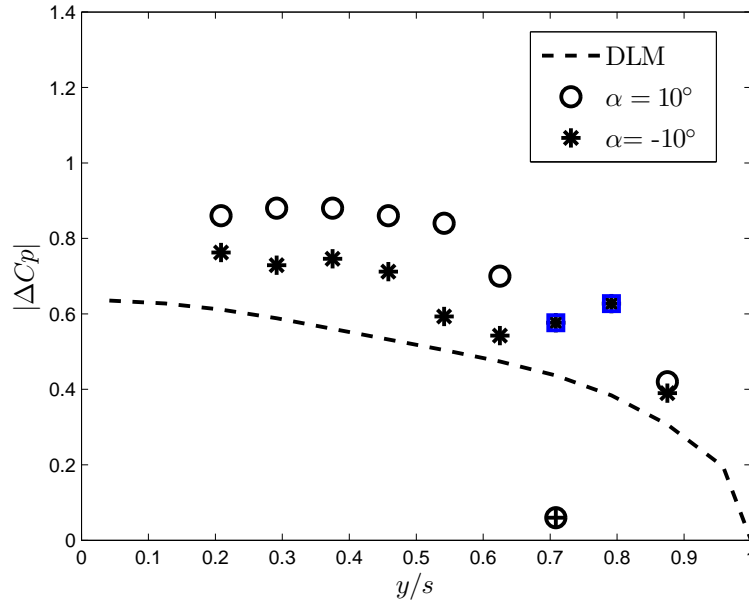


(a)  $x/c=0.1625$ ,  $\alpha = 8^\circ$ , hole

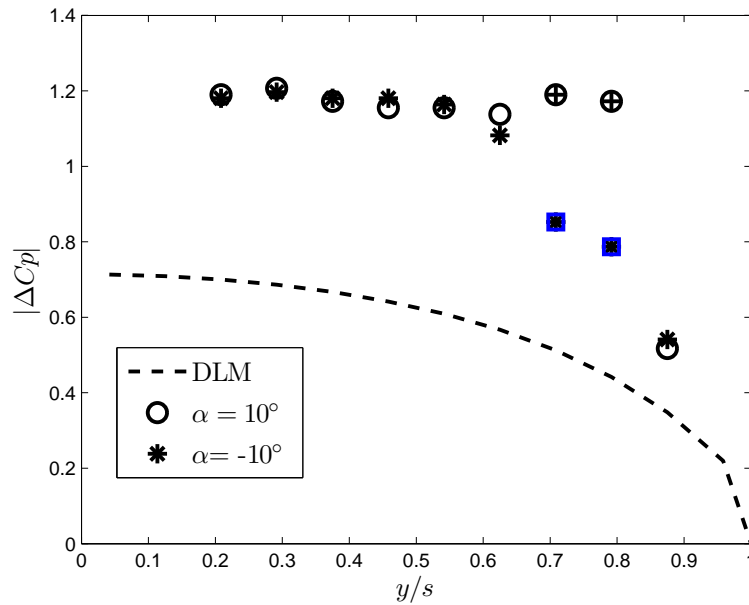


(b)  $x/c=0.1625$ ,  $\alpha = 8^\circ$ , insert no. 1

FIGURE 4.16: The magnitude of the theoretical and experimental  $\Delta C_p$  versus spanwise position,  $y/s$ , at  $x/c = 0.1625$ .  $\alpha = 8^\circ$ .



(a)  $x/c=0.1625$ ,  $\alpha = 10^\circ$ , hole



(b)  $x/c=0.1625$ ,  $\alpha = 10^\circ$ , insert no. 1

FIGURE 4.17: The magnitude of the theoretical and experimental  $\Delta C_p$  versus spanwise position,  $y/s$ , at  $x/c = 0.1625$ .  $\alpha = 10^\circ$ .

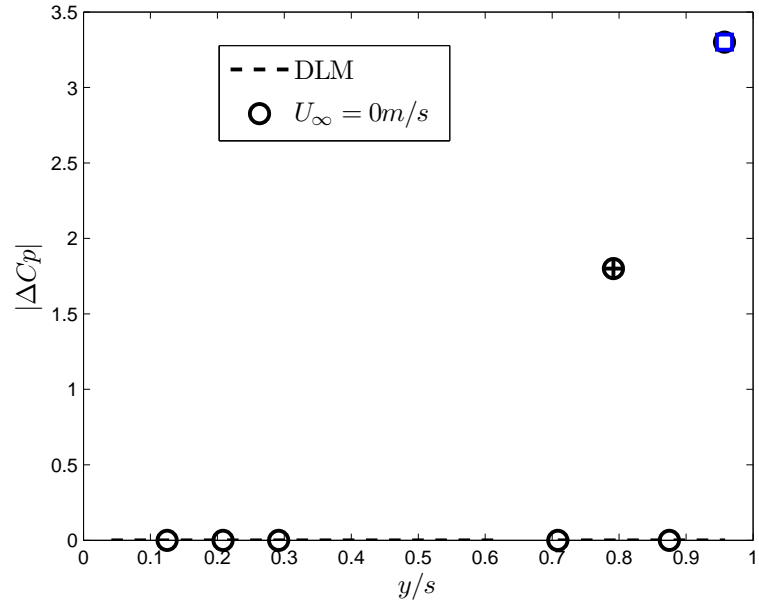
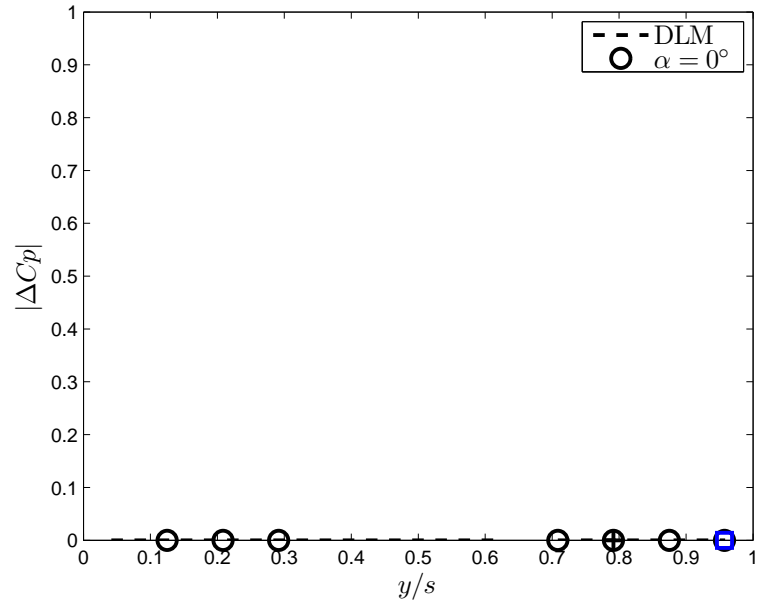
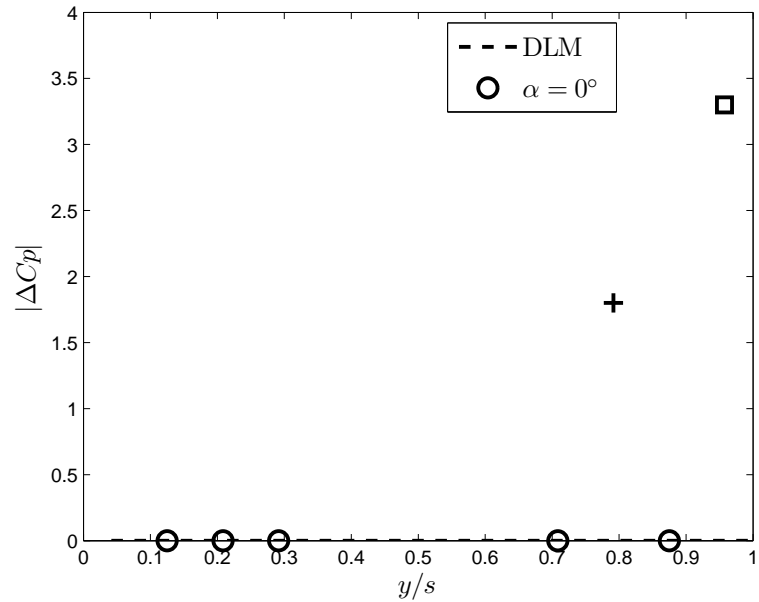


FIGURE 4.18: The magnitude of the theoretical and experimental  $\Delta C_p$  versus spanwise position,  $y/s$ , at  $U_\infty = 0m/s$  versus spanwise position at  $x/c = 0.4625$ .  $\alpha = 0^\circ$ .

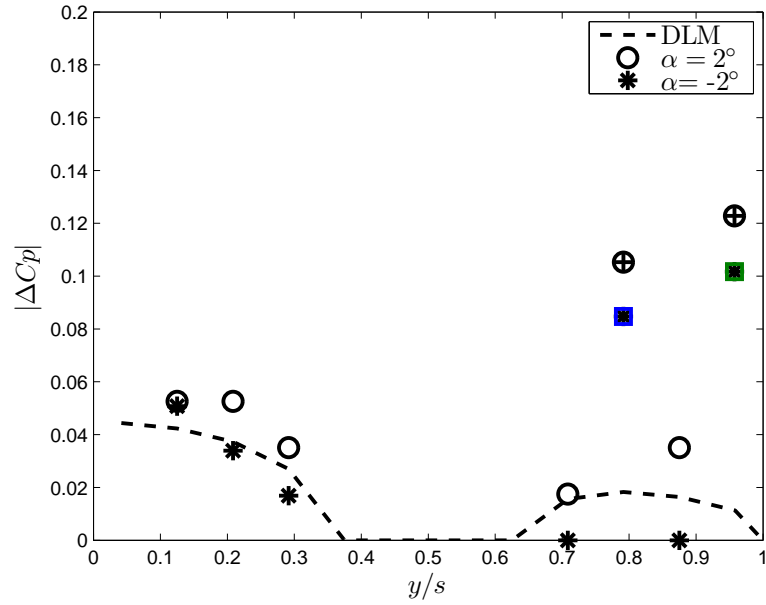


(a)  $x/c=0.4625, \alpha = 0^\circ, \text{hole}$

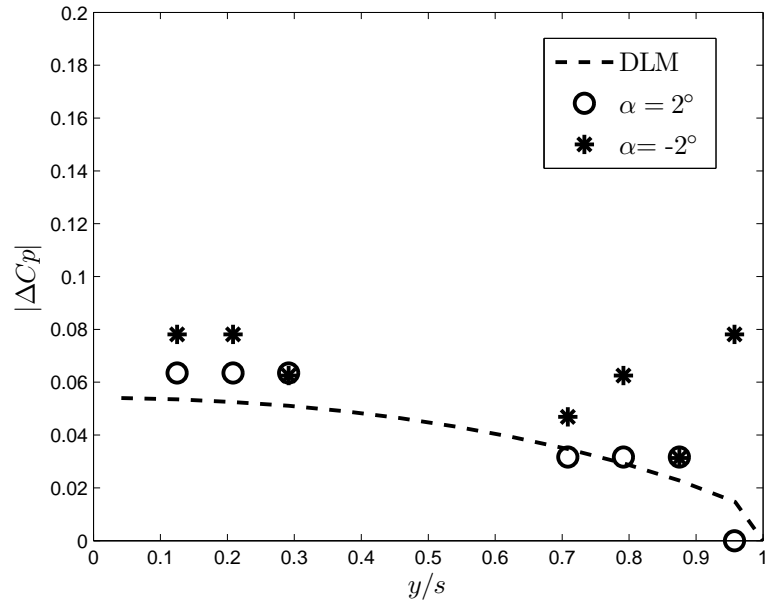


(b)  $x/c=0.4625, \alpha = 0^\circ, \text{insert no. 1}$

FIGURE 4.19: The magnitude of the theoretical and experimental  $\Delta C_p$  versus spanwise position,  $y/s$ , at  $x/c = 0.4625$ .  $\alpha = 0^\circ$ .

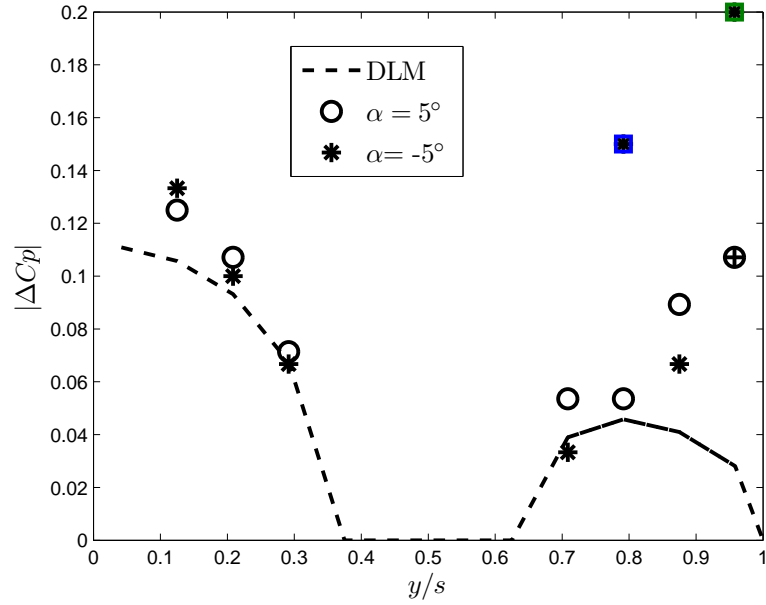


(a)  $x/c=0.4625$ ,  $\alpha = 2^\circ$ , hole

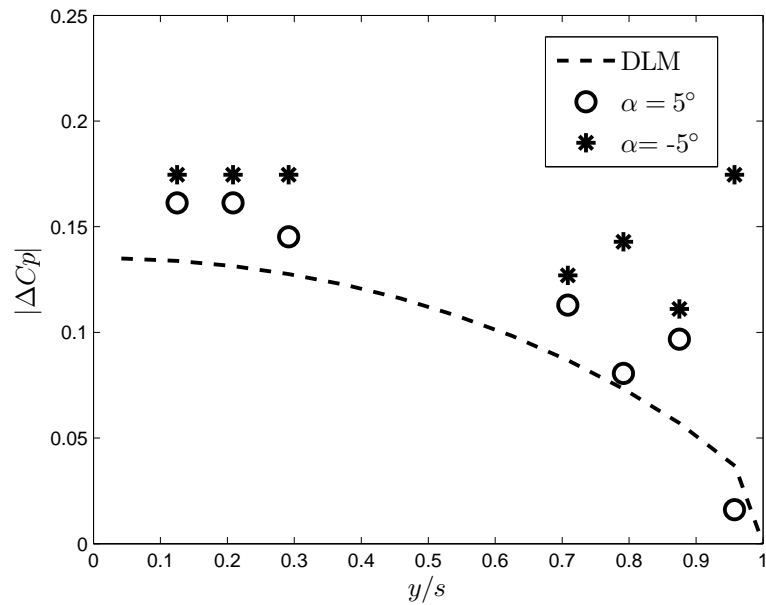


(b)  $x/c=0.4625$ ,  $\alpha = 2^\circ$ , insert no. 1

FIGURE 4.20: The magnitude of the theoretical and experimental  $\Delta C_p$  versus spanwise position,  $y/s$ , at  $x/c = 0.4625$ .  $\alpha = 2^\circ$ .

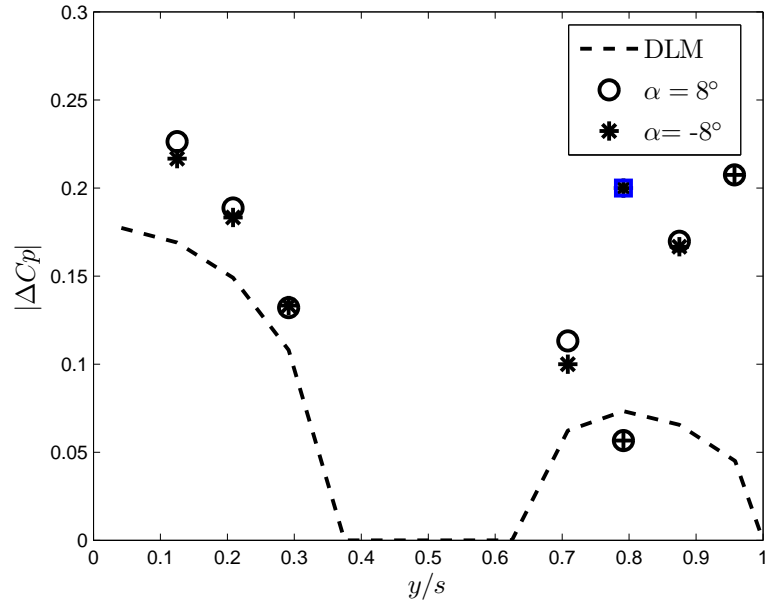


(a)  $x/c=0.4625$ ,  $\alpha = 5^\circ$ , hole

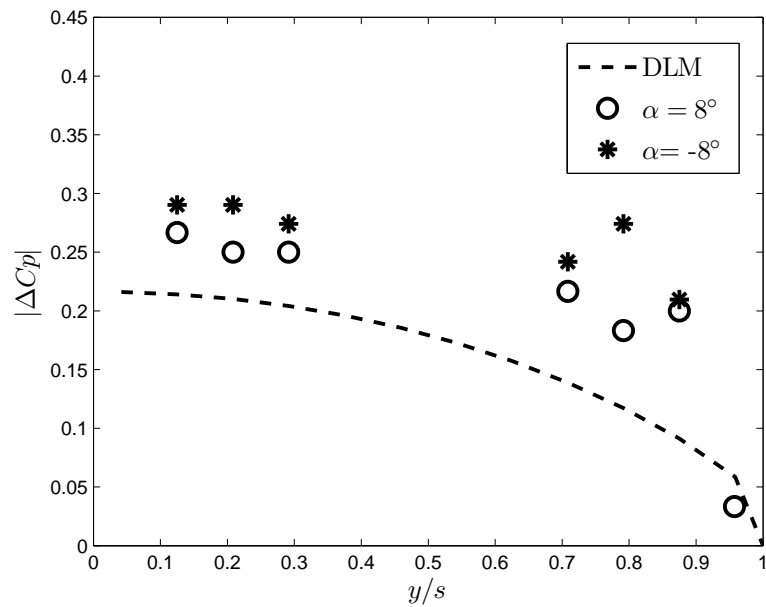


(b)  $x/c=0.4625$ ,  $\alpha = 5^\circ$ , insert no. 1

FIGURE 4.21: The magnitude of the theoretical and experimental  $\Delta C_p$  versus spanwise position,  $y/s$ , at  $x/c = 0.4625$ .  $\alpha = 5^\circ$ .

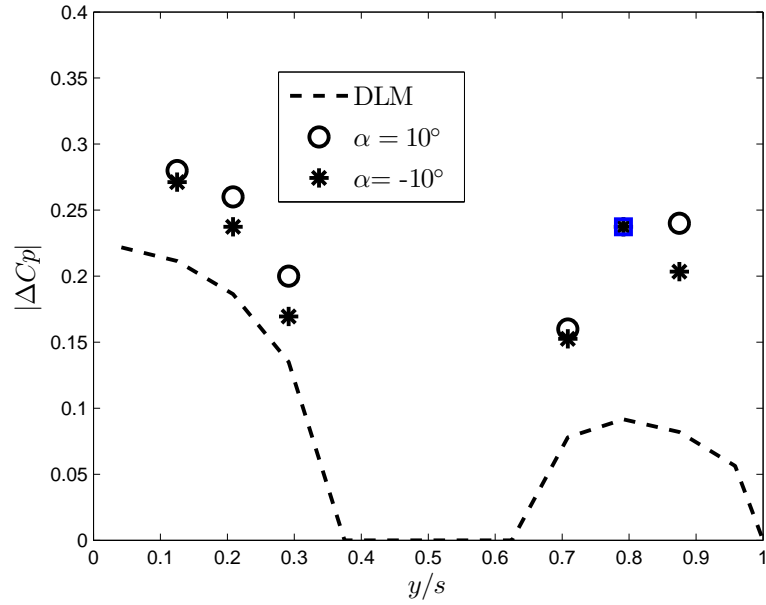


(a)  $x/c=0.4625$ ,  $\alpha = 8^\circ$ , hole

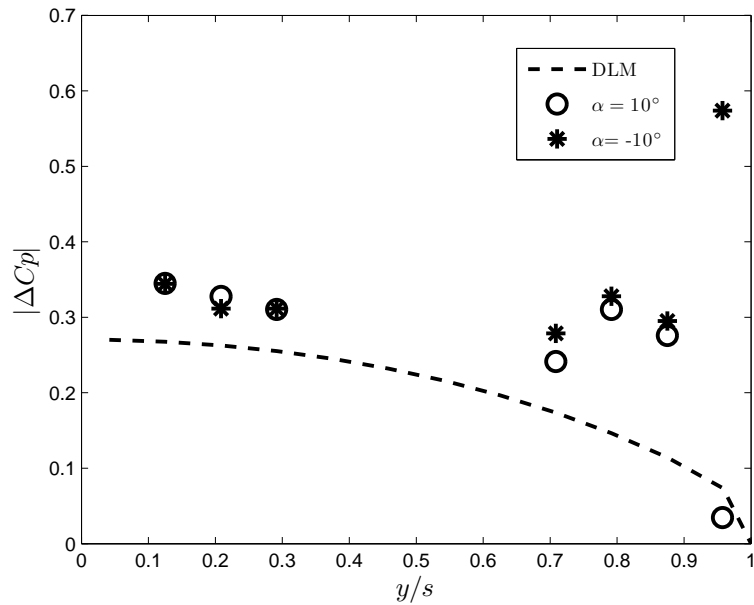


(b)  $x/c=0.4625$ ,  $\alpha = 8^\circ$ , insert no. 1

FIGURE 4.22: The magnitude of the theoretical and experimental  $\Delta C_p$  versus spanwise position,  $y/s$ , at  $x/c = 0.4625$ .  $\alpha = 8^\circ$ .



(a)  $x/c=0.4625$ ,  $\alpha = 10^\circ$ , hole



(b)  $x/c=0.4625$ ,  $\alpha = 10^\circ$ , insert no. 1

FIGURE 4.23: The magnitude of the theoretical and experimental  $\Delta C_p$  versus spanwise position,  $y/s$ , at  $x/c = 0.4625$ .  $\alpha = 10^\circ$ .

### 4.3 Conclusions from the aerodynamic experiment and computation

The results for the experimental aerodynamic model are better than the model built previously for the preliminary examination. Designing the model in Solidworks™ and machining it using a CNC mill, the model was improved. This model does have round tapered edges to prevent the problems caused by blunt edges in a previous built model. The leading edge is sharper than what is typically desired for an aerodynamic experiment but that is due to the thickness of the model. Also, as a lesson learned from the previous model, it was determined to have a wing without a hole to establish a baseline. Incorporation of the baseline experimental apparatus was best achieved using inserts. Inserts are determined to be the best, so any ambiguities in regards to pressure taps that may come from building a second model are eliminated.

Overall, the results from the model tested with a hole correlated nicely with the theory used for associating a hole in a wing. These results are much improved from the model tested in the preliminary examination. The coefficient of pressure results for steady flow along the chordwise direction changes in magnitude are large and so it is easier to measure. The results along the chordwise position agree quite well. The coefficient of pressure results for steady flow along the spanwise direction are quite small and it is not easy to measure. Near the root of the wing the results are plausible, but near the tip the data is erratic. It was determined that some of the pressure taps were functioning improperly since at  $U=0$  m/s, the pressure should be zero but it was not.

The wing without a hole or actually the same model but with an insert installed did not agree as well to the theory. Initially, the disagreement was believed to be due to misalignment. This suggests a possible misalignment between the surface and the insert. As a result, the model was retested with two additional inserts. Insert no. 2 is made out of two pieces of aluminum that are 0.010" thick and slightly larger

than the hole. The edges of these pieces were filed down so they would have smooth edges. The pieces were adhered to the surface using thin tape. Insert no. 2 was only tested along the chordwise position at  $y/s = 0.458$  across the hole because the pressure differential in this region is more important in this study. Insert no. 3 is made out of a thin vinyl adhesive covering. In each case, the trends observed by the two new inserts are similar to the first insert that are presented therefore they are not shown here. The experimental results are consistent but it is not understood why the testing with the insert does not agree as well with the theory as the model without the insert. One explanation that may explain this is the notion that a boundary layer is growing off of the mildly sharp leading edge. However, when the hole is present the jump in pressure across the hole in the chordwise direction actually breaks up the growing boundary layer.

# 5

## Aeroelastic Studies of Wings with Holes, but without Stores

In this dissertation, the structural dynamics and the aerodynamics are investigated for a thin plate wing model with and without a hole, respectively. Coupling the structural dynamics with the aerodynamics allows one to form an aeroelastic model. Experimental models are designed to test the theoretical models. For a thorough understanding of the aeroelastic behavior of wing with damage, it is best to start with a wing model without any stores(i.e. external fuel tanks and missiles). Modeling such a wing with a hole presents it own set of challenges.

### 5.1 Lagrange's equations and modal methods

The aerodynamic and structural forces are calculated independently using the doublet lattice method and the finite element method, respectively. They are coupled to form a theoretical aeroelastic model. The aeroelastic equations per se are formulated using Lagrange's equations and modal methods [1]. Lagrange's equation is expressed

in Eqn. 5.1.

$$\frac{d}{dt} \frac{\partial L}{\partial \dot{q}_i} - \frac{\partial L}{\partial q_i} = Q_i \quad (5.1)$$

$L \equiv T - U$ , Lagrangian

$T \equiv$  kinetic energy of the structure

$U \equiv$  potential energy of the structure

$Q_i \equiv$  generalized forces from the aerodynamic model

$q_i \equiv$  generalized coordinates

The Lagrangian is computed using the results obtained from structural theory. For the aeroelastic analysis, 10 out of about 1000 natural modes found in a finite element analysis using ANSYS<sup>TM</sup> are retained. The structural natural frequencies( $\omega_m$ ), structural natural modes( $z_m$ ), and the calculation of the generalized masses are used in a modal series expansion[1]. The structural modal expansion in Eqn. 5.2 contains  $q_m(t)$  as the generalized coordinates and  $z_m(x, y)$  as the natural mode.

$$z_a = \sum_m q_m(t) z_m(x, y) \quad (5.2)$$

The kinetic and potential energy expressions in Eqns. 5.3 and 5.4 include the generalized mass( $M_m$ ) and stiffness( $K_m$ ). The generalized mass is computed in Eqn. 5.5 where  $m_a$  is the mass per unit area. The stiffness matrix,  $K_m$ , equals  $\omega_m^2$  times the mass matrix when using the natural modes.

$$T = 1/2 \sum_m M_m \dot{q}_m^2 \quad (5.3)$$

$$V = 1/2 \sum_m K_m q_m^2 \quad (5.4)$$

$$M_m \equiv \int \int m_a z_m^2 dx dy \quad (5.5)$$

The generalized aerodynamic forces( $Q_{ij}$ ) on the wing are computed using the doublet lattice method by finding the pressure due to a prescribed downwash. The non-dimensional downwash in Eqn. 5.6 that is needed by the doublet lattice method(DLM) is found using the deflection and the slope of the natural mode. Generally, the deflection points of the mode do not match the aerodynamic grid, so a curve fitting technique is applied to resolve the issue.

$$\frac{w}{U} = \frac{1}{U} \frac{\partial z_a(x, y, t)}{\partial t} + \frac{\partial z_a(x, y, t)}{\partial x}. \quad (5.6)$$

#### 5.1.1 Polynomial curve fitting of the structural mode shape

The discretization needed to calculate the structural and aerodynamic loadings are different. The goal of fitting the structural mode shape is to take the structural natural mode and characterize it using a polynomial expression so the downwash can be computed for the aerodynamic model. A polynomial curve fit is implemented using a least squares method on each eigenmode found in ANSYS<sup>TM</sup> to determine the polynomial coefficients in order that the deflections can be found anywhere on the wing.

A fifth or sixth order polynomial is capable of modeling a structural mode with 21 and 28 coefficients, respectively. The sixth order polynomial that is a function of  $x$  and  $y$  is expanded in Eqn. 5.8 is used to represent the natural mode after the 28 unknown coefficients have been found. Therefore, since 10 eigenmodes are used in developing the aeroelastic equations, 280 coefficients must be found when using the

sixth order polynomial or 210 coefficients when using a fifth order polynomial.

$$z_m = F(x, y) \quad (5.7)$$

$$\begin{aligned} = & a_1 + a_2x + a_3y + a_4x^2 + a_5xy + a_6y^2 + a_7x^3 + a_8x^2y \\ & + a_9xy^2 + a_{10}y^3 + a_{11}x^4 + a_{12}x^3y + a_{13}x^2y^2 + a_{14}xy^3 \\ & + a_{15}y^4 + a_{16}x^5 + a_{17}x^4y + a_{18}x^3y^2 + a_{19}x^2y^3 + a_{20}xy^4 \\ & + a_{21}y^5 + a_{22}x^6 + a_{23}x^5y + a_{24}x^4y^2 + a_{25}x^3y^3 + a_{26}x^2y^4 \\ & + a_{27}xy^5 + a_{28}y^6 \end{aligned} \quad (5.8)$$

The unknown polynomial coefficients are computed using the data extracted from ANSYS™ and the least squares method. From each element in the finite element model, the deflection at a specific  $x, y$  is known in Eqn. 5.8 and the only unknowns are the coefficients  $a_1$ - $a_n$ . It has been determined that the ANSYS™ model needs about 1000 elements to achieve good convergence.

$$z_{m1}(x_1, y_1) = [a_1 \ a_2x_1 \ a_3y_1 \ a_4x_1^2 \ a_5x_1y_1 \ a_6y_1^2 \ \cdots] \quad (5.9)$$

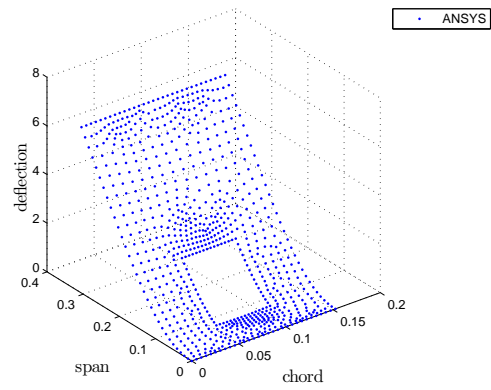
$$z_{m2}(x_2, y_2) = [a_1 \ a_2x_2 \ a_3y_2 \ a_4x_2^2 \ a_5x_2y_2 \ a_6y_2^2 \ \cdots] \quad (5.10)$$

Explaining the least square method is made easier by using 1000 elements but it can be any number. The unknown coefficients are found by expanded each mode's deflection as in Eqn. 5.10. The system of equations is placed in matrix form, Eqn. 5.11. Equation 5.11 is rewritten compactly as Eqn. 5.12. The matrix in Eqn. 5.11 is dimensioned  $1000 \times 28$ , the coefficient vector is dimensioned  $28 \times 1$ , and the  $z$  vector is dimensioned  $28 \times 1$  for a sixth order polynomial. The x-vector and z-vector are known as the coefficient and deflection vector, respectively. More generally, the matrix in Eqn. 5.11 is dimensioned as  $ND \times NC$  where "ND" is the number of elements and

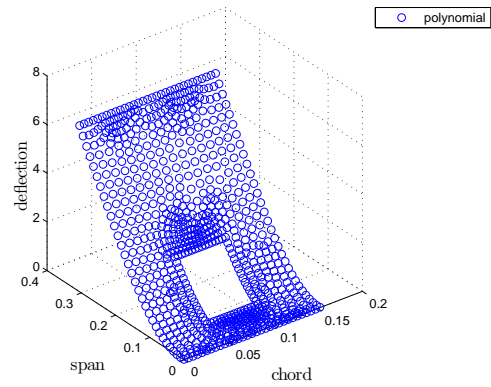
“NC” is the number of coefficients. The vector of coefficients is dimensioned as  $NC \times 1$  and the  $z$  vector is dimensioned as  $ND \times 1$ .

$$\begin{bmatrix} 1 & x_1 & y_1 & x_1^2 & \cdots \\ 1 & x_2 & y_2 & x_2^2 & \cdots \\ \vdots & & \cdots & & \\ \vdots & & \vdots & & \\ & & \cdots & & \end{bmatrix}_{ND \times NC} \times \begin{Bmatrix} a_1 \\ a_2 \\ \vdots \\ \end{Bmatrix}_{NC \times 1} = \begin{Bmatrix} z_1 \\ z_2 \\ \vdots \\ \end{Bmatrix}_{ND \times 1} \quad (5.11)$$

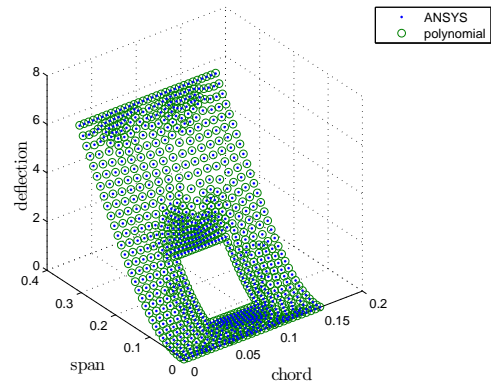
$$[A]_{ND \times NC} \{x\}_{NC \times 1} = \{Z\}_{ND \times 1} \quad (5.12)$$



(a) Fundamental mode from ANSYS™



(b) Polynomial fit of fundamental mode



(c) Polynomial fit and fundamental mode

FIGURE 5.1: Comparison of fundamental mode to polynomial fit

The initial step in determining the unknown coefficients is multiplying both sides of Eqn. 5.12 by the transpose of matrix A to produce Eqn. 5.14. The next and final step is solving for the x-vector as in Eqn. 5.15. The approach outlined is capable of curve fitting higher or lower order polynomials depending on the accuracy needed. However, the order of the polynomial should not be more than what is actually needed for good representation. The over or under prediction of a polynomial will yield misleading results so it a delicate balance on the level of approximation. The fifth and sixth order polynomials are suitable for representing the mode shapes. The fifth order polynomial is able to accurately able to reproduce the fundamental mode shape, see Fig. 5.1. The slope of the deflection is computed by taking the derivative of Eqn. 5.8 with respect to “x”. With the coefficients, the downwash needed for the doublet lattice method can be easily found.

$$[A^T]_{NC \times ND} [A]_{ND \times NC} \{x\}_{NC \times 1} = [A^T] \{Z\}_{ND \times 1} \quad (5.13)$$

$$[\tilde{A}]_{NC \times NC} \{x\}_{NC \times 1} = \{\tilde{Z}\}_{NC \times 1} \quad (5.14)$$

$$\{x\}_{NC \times 1} = [\tilde{A}]_{NC \times NC}^{-1} \{\tilde{Z}\}_{NC \times 1} \quad (5.15)$$

### 5.1.2 Aeroelastic model

The use of the structure’s natural modes simplifies the computation of the mass and stiffness matrices for the aeroelastic model by only having to compute the terms along the diagonal. The accuracy of the polynomial can be evaluated from the values along the diagonal of the mass matrix, since they should approximately equal one when normalized. The fifth order polynomial gives the best results for the diagonal

values of the matrices and for reproducing the deflections of a location on the plate in a given mode.

The generalized forces are determined by using the polynomial expression to compute the downwash as the input to the DLM to find the unknown pressures across the lifting surface. Using Eqns. 5.1-5.4, Lagrange's equation is written compactly after modal expansion in Eqn. 5.16. The term  $\frac{\rho U^2}{2} \sum_m A_{mi}(k)$  comes from computing the aerodynamic loads as a function of the nondimensional frequency( $k$ ). In Eqn. 5.16  $\rho$  and  $U$  are the freestream density and velocity, respectively.

$$\sum_m M_{mi} \ddot{q}_m + K_{mi} q_m = \frac{\rho U^2}{2} \sum_m A_{mi}(k) q_m \equiv Q_i \quad (5.16)$$

The V-g method in conjunction with the aeroelastic system derived in Eqn. 5.16 is suitable for determining the flutter boundary [1]. The V-g method is an iterative eigenvalue analysis that is based upon choosing the nondimensional frequency,  $k$ , used in calculating the aerodynamics. The V-g method is incorporated into Eqn. 5.16 by multiplying the stiffness matrix by the quantity  $1 + ig$ , where  $g$  is the fictitious damping added to find the neutrally stable solutions. Additionally, simple harmonic motion( $q = \bar{q}^{i\omega t}$ ) is assumed so  $\bar{q}$  can be factored out of Eqn. 5.16, and the problem can be totally solved in the frequency domain. The  $\omega^2$  term is divided through out Eqn. 5.16 and the eigenvalue( $\lambda = (1 + ig)/\omega^2$ ) is produced. The  $Re\lambda$  and  $Im\lambda$  are computed at every  $k$ ; therefore  $\omega^2$  and  $g$  are calculated at each iteration. Recalling that  $k = \omega b/U$  is chosen, the velocity  $U$  is computed from Eqn. 5.20 since  $\omega$  is computed from  $Re\lambda$  and the semichord( $b$ ) is known. The specific velocity where flutter occurs is when the damping,  $g$ , equals zero or some representative value of the structural damping. The Federal Aviation Administration allows  $g$  to equal 0.02 in industry for flutter clearance of fighter aircraft since all structures have some damping present[1]. The damping( $g$ ) in this dissertation is assumed to equal to zero.

$$\left\{ -[M] + \frac{1 + ig}{\omega^2}[K] - \frac{\rho b^2}{2k^2}[A(k)] \right\} \{\bar{q}\} = 0 \quad (5.17)$$

$$q = \bar{q}e^{i\omega t} \quad (5.18)$$

$$\lambda = \frac{1 + ig}{\omega^2} \quad (5.19)$$

$$k = \frac{\omega b}{U} \Rightarrow U = \omega b/k \quad (5.20)$$

## 5.2 Cantilevered rectangular aeroelastic models

Several cantilevered rectangular aeroelastic models are designed to flutter in a flow range suitable to the Duke University Subsonic Wind Tunnel using the methods outlined previously. The material properties for the polycarbonate(plexiglas) plate used to make the designed aeroelastic models are as follows:  $\rho=1217 \text{ kg/m}^3$ ,  $E=2.4e9 \text{ N/m}^2$ , and  $\nu=0.33$ . The polycarbonate wing has a thickness of 0.001588 m, a width(chordwise) of 0.1524 m(6 in), and a length(spanwise) of 0.3048 m(12 in). The aspect ratio of the wing is 2.0. The structure is fully clamped along the root chord.

The aeroelastic models are tested structurally as noted in Ch. 2 using a vibration test and/or a hammer test. A standard practice before conducting a flutter test is the determination of the natural frequencies and sometimes the mode shapes to verify the model has been built and mounted correctly[45, 2]. Ideally, the difference between theory and experiment for natural frequencies of an aeroelastic model should be within 10% [45]. This is important since it can aid in eliminating the structural

theory as a potential problem, if the structural model checks out well experimentally, but then the aeroelastic wind tunnel model test results do not correlate with the theory.

Typically, the coupling among the lower modes dominates the flutter response. The placement of a hole plays a significant role in determining the natural frequencies because the hole modifies the structural mass and stiffness. It was stated earlier that from a structural viewpoint the stiffness effects play a more dominant role when the hole is near the root, hence the natural frequencies decrease. The impact of the hole damage on flutter will be determined in the following experimental studies.

### *5.2.1 Data acquisition for flutter experiments*

The primary data of interest in flutter testing is the flutter frequency and velocity. The flutter frequency is determined experimentally using a Brüel & Kjær (B&K) type 4375 accelerometer that is fixed near the wing's root on the trailing edge. The accelerometer is placed here because of its small effect on the generalized mass due to its small displacement. The B&K type 2635 charge amplifier is used to increase the signal strength going from the accelerometer to the B&K 4 channel PULSE™ 3560-T-C front end. The acceleration versus time series data is collected and analyzed during testing using the B&K PULSE™ data acquisition system to perform a fast fourier transform(FFT) analysis in real-time. The flutter phenomena is observed visually, but the FFT's verify the onset of flutter. A careful observation of several FFTs as the velocity in the tunnel increases shows how the frequency reponse curve associated with flutter grows while the peak's width narrows and the amplitude increases. Before flutter the peak is not seen in the FFT. Simultaneously, the wind tunnel's velocity is recorded from the voltmeter connected to the pitot static tube.

### 5.2.2 Aeroelastic rectangular wing model without a hole

An aeroelastic model without a hole is designed and tested to establish a baseline. The graphical representation of the results from the V-g method applied in Eqn. 5.17 can be seen in Figs. 5.2, 5.3, and 5.4. The system becomes unstable when the damping becomes positive. The system is stable when the damping required for neutral stability is negative.

**Theoretical and experimental natural frequencies of rectangular wing**

		No Hole	
mode no.	char.	Theory	Exp
1	Bend.	3.9921 Hz	4.13 Hz
2	Tors.	16.948	17.25
3	Bend.	24.861	24.38
4	Tors.	55.326	54.25
5	Bend./Tors.	69.842	69.00

Table 5.1: The first five natural frequencies(in Hz) of the cantilevered plate without a hole. Bend. and Tors. refer to the bending and torsion mode, respectfully.

The theoretical and experimental natural frequencies can be seen in Table 5.4. During wind tunnel testing before the onset of flutter the third, fourth, and fifth structural natural frequencies are seen in the fast fourier transforms(FFTs) of the data therefore checking our results from the hammer test. The first and second natural frequencies are not clearly seen in the experimental data at the lower flow velocities in comparison to the third, fourth, and fifth frequencies. The accelerometer placed near the cantilevered root has a smaller displacement and therefore has difficulty recording the response due to the lower modes. The higher frequency modes have more acceleration in this region. However, as the flutter velocity is approached, the frequency of the critical flutter mode is easily seen in the spike that appears in the FFT of the time series data in Fig. 5.5. According to the V-g analysis, when flutter occurs the damping is zero and therefore the spike that indicates flutter should be narrow. The smaller spikes seen in Fig. 5.5 are due to noise and the

higher structural modes.

The experimental model fluttered in the wind tunnel when mounted vertically at  $0^\circ$  angle of attack at  $U_f=20.05$  m/s and  $\omega_f=11.50$  Hz. The model is mounted vertically since the effects of gravity are neglected in the theory. The cantilevered wing is designed to flutter at  $U_f=20.8$  m/s and  $\omega_f=10.38$  Hz at  $0^\circ$  angle of attack. The time series data and its fast fourier transform(FFT) used in determining the flutter frequency are shown in Fig. 5.5. The differences between the theoretical and experimental flutter velocity and frequency are 3% and 10%, respectively. Furthermore, the flutter mode is dominated by the first torsional(second natural) mode in the theoretical aeroelastic model. A comparison between theory and experiment for how the frequency of the dominant mode (the first torsional mode) changes versus flow velocity for the first torsional mode is shown in Fig. 5.6 until the onset of flutter.

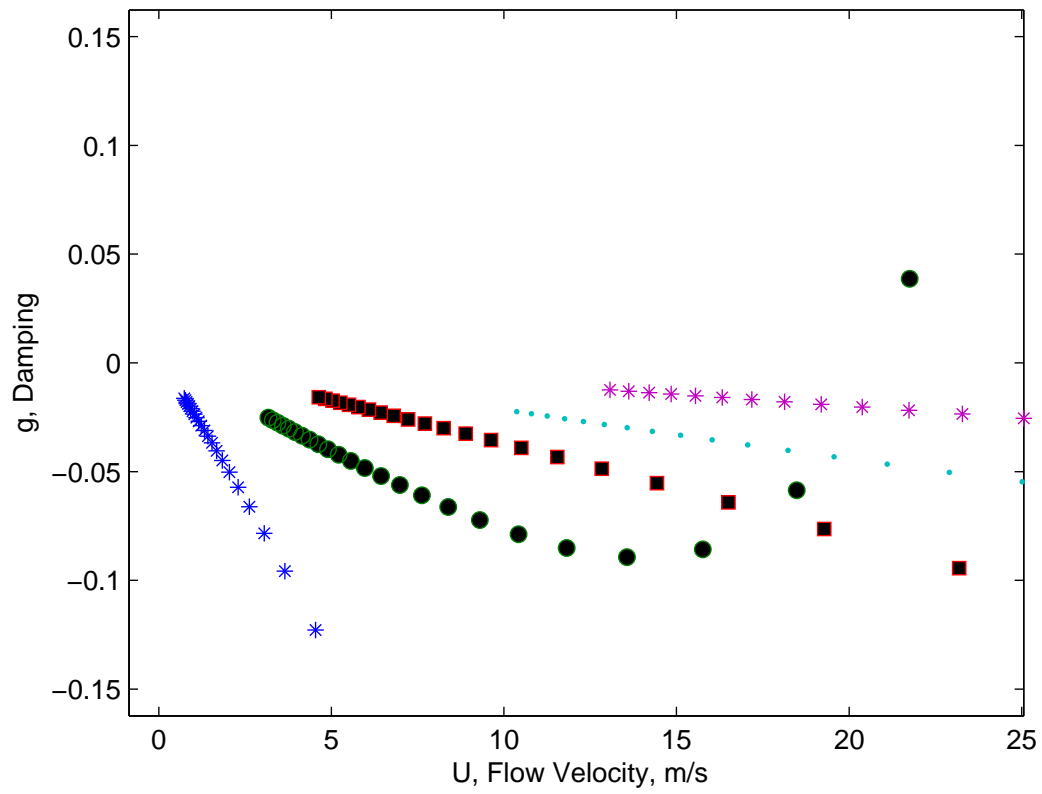


FIGURE 5.2: Damping vs. Flow Velocity for cantilevered rectangular wing without a hole

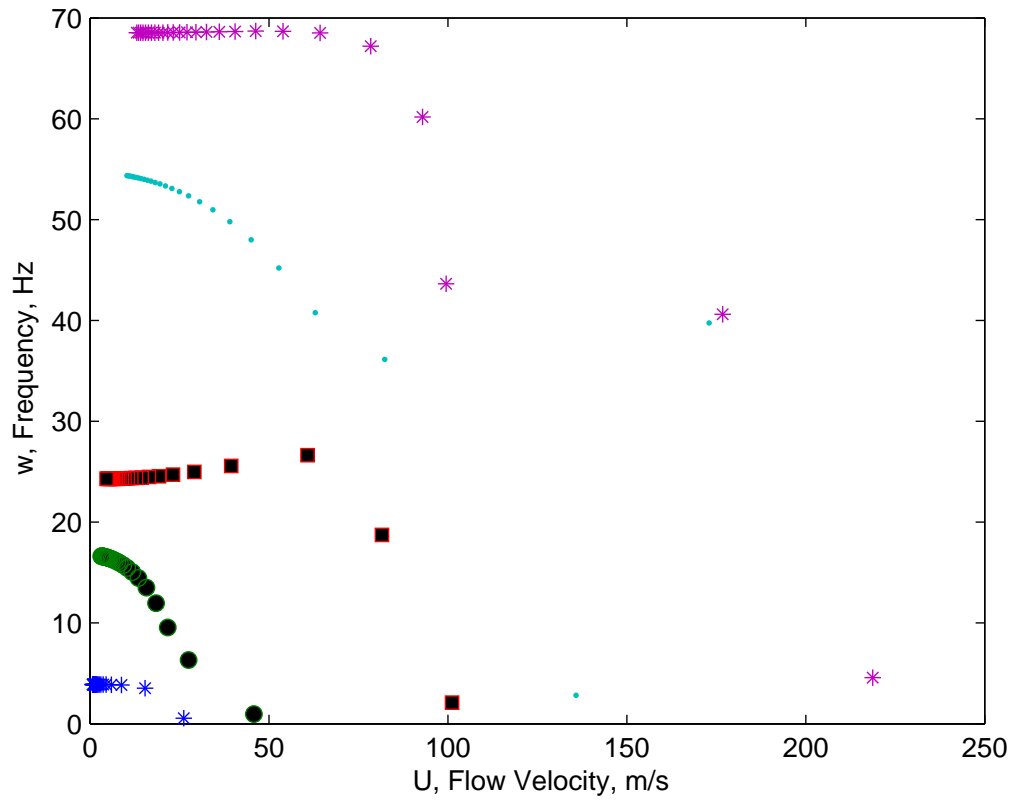


FIGURE 5.3: Frequency vs. Flow Velocity for cantilevered rectangular wing without a hole

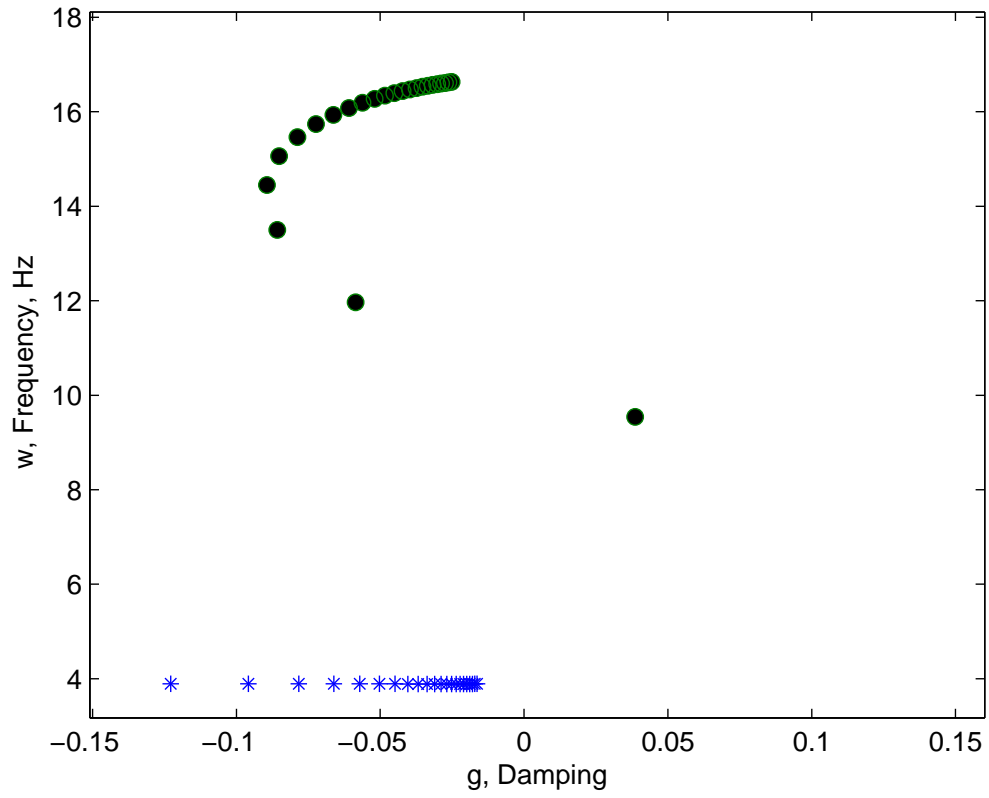
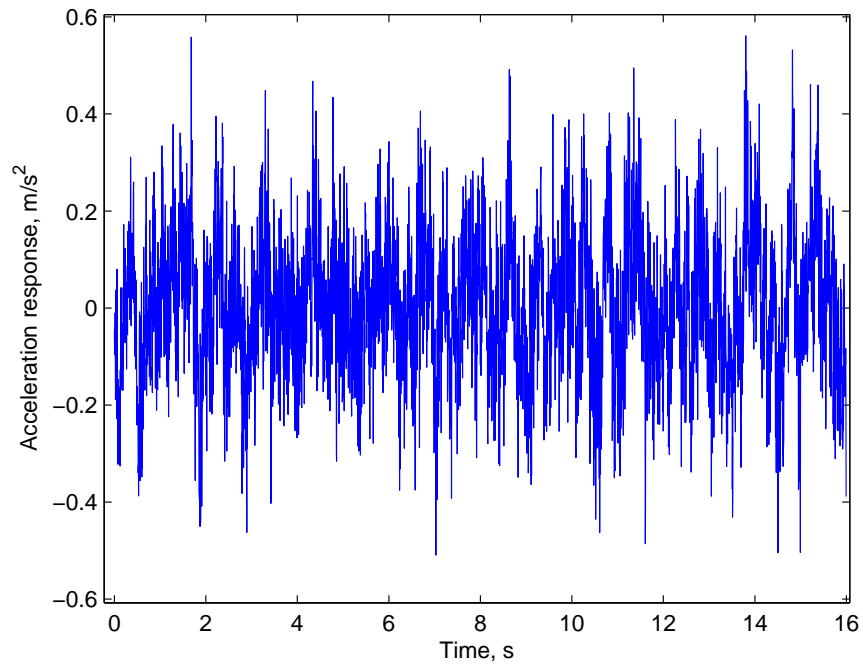
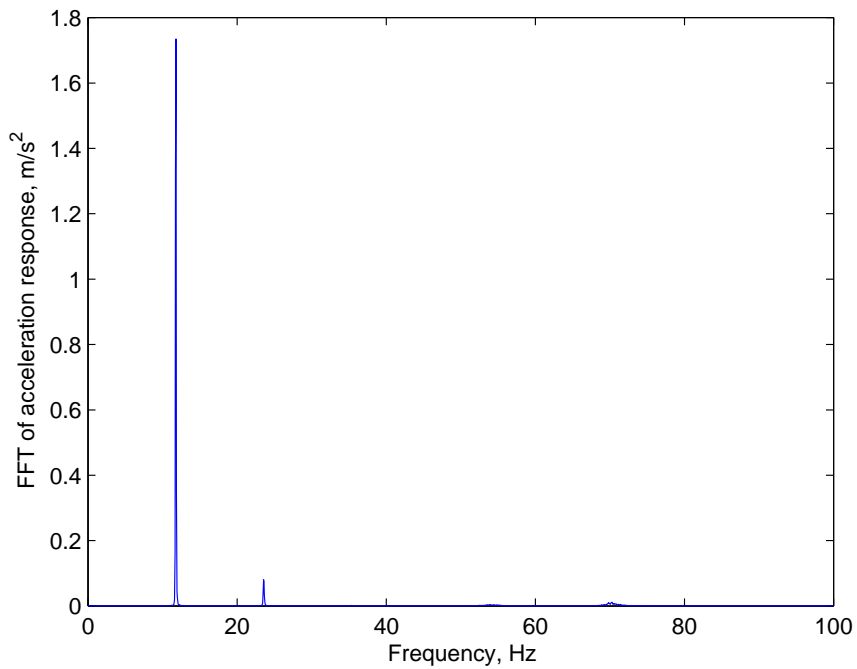


FIGURE 5.4: Frequency vs. Damping for cantilevered rectangular wing without a hole



(a) time vs acceleration at  $U = 20.05 \text{ m/s}$



(b) FFT amplitude vs frequency at  $U = 20.05 \text{ m/s}$

FIGURE 5.5: FFT analysis of flutter acceleration response measured on the trailing edge for a cantilevered rectangular wing without a hole

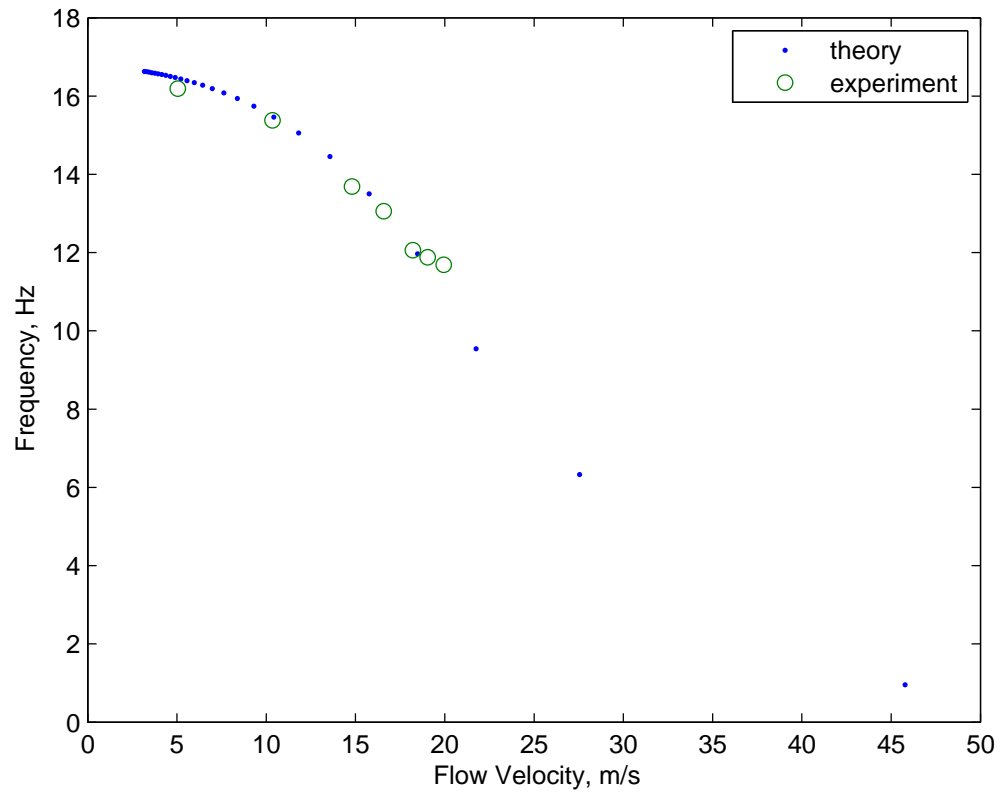


FIGURE 5.6: Correlation of Frequency vs Velocity between theory and experiment for the first torsional mode for the cantilevered rectangular wing without a hole

### 5.2.3 Aeroelastic rectangular models with a hole

The first set of designed aeroelastic cantilever rectangular wings, Case I, have a rectangular hole that measures  $a = 0.057$  m (2.25 in) and  $b = 0.095$  m (3.75 in) as dimensioned in Fig 5.7. The polycarbonate wing is identical to the model without a hole. Recall, the wing has a thickness of 0.001588 m, a width(chordwise) of 0.1524 m (6 in), and a length(spanwise) of 0.3048 m (12 in). The distance measured from the leading edge to the hole is 0.045 m. The hole size and the amount of mass removed is roughly 12% of the total wing. Each hole is the same distance from leading edge in the chordwise direction, but varies in the spanwise direction, see Figs. 5.7 and 5.8.

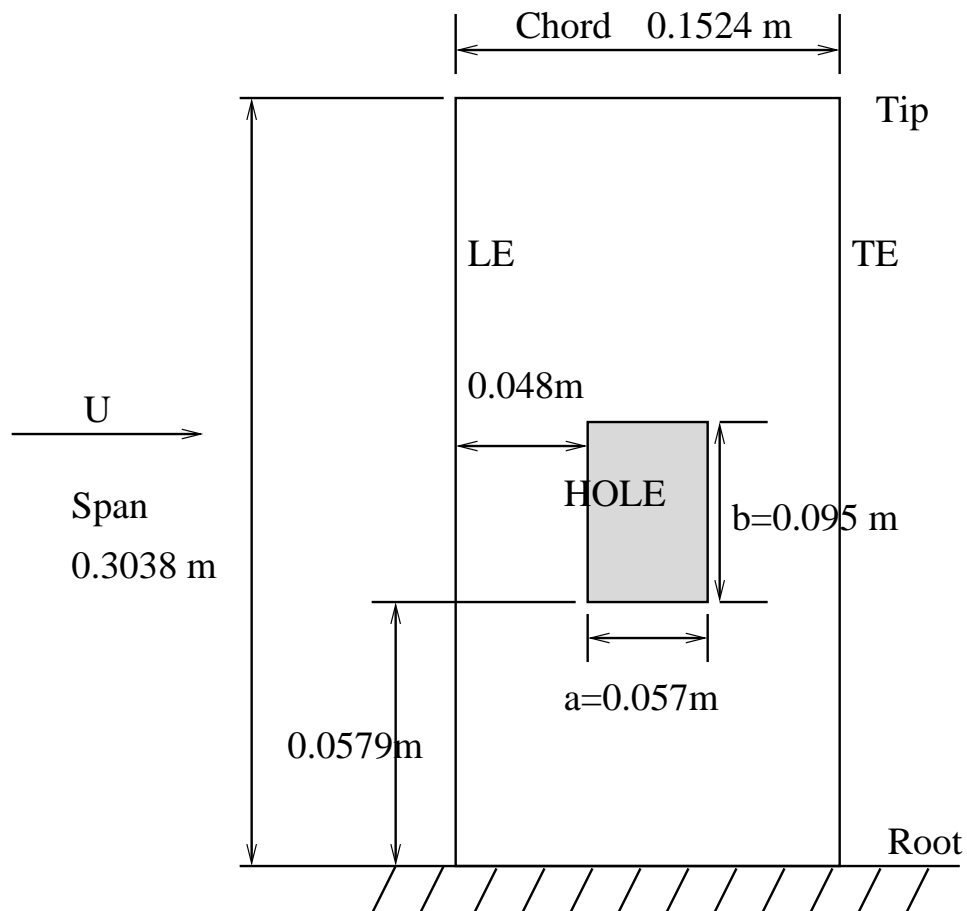


FIGURE 5.7: Dimensional drawing of rectangular wing with hole near root

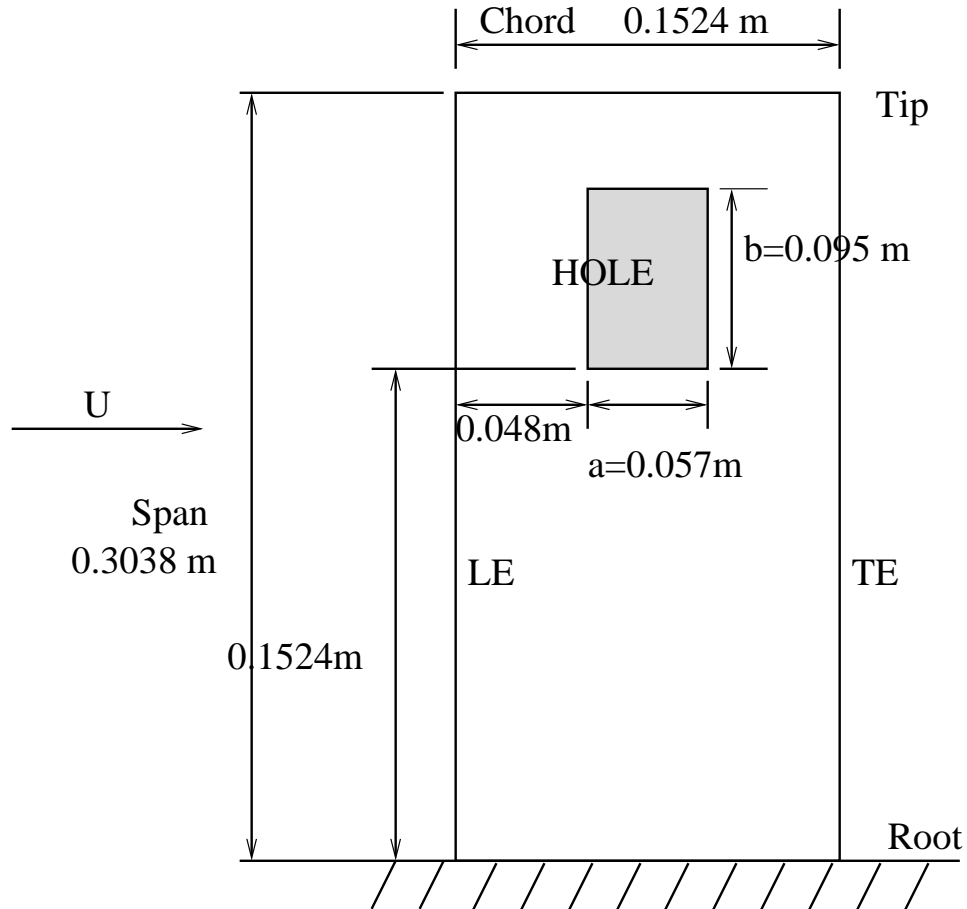


FIGURE 5.8: Dimensional drawing of rectangular wing with hole near tip

The fundamental natural frequency increases as the hole goes outward in the spanwise direction, indicating the bending stiffness is decreasing. The increase in the fundamental natural frequency can be seen theoretically and experimentally in Table 5.2. As a result, the flutter velocity increases and it can be seen theoretically and experimentally in Table 5.3. In addition, in this case where the hole size is 12% of the wing area, no flutter velocity is found that is lower than that of the wing without the hole.

**Computed cantilevered rectangular wing natural frequencies**

		No Hole		Root		Tip	
mode no.	char.	Theory	Exp	Theory	Exp.	Theory	Exp.
1	Bend.	3.9921	4.13	3.49	3.50	4.2	4.25
2	Tors.	16.948	17.25	15.08	15.5	16.02	16.13
3	Bend.	24.861	24.38	24.69	25	23. 24	23.75
4	Tors.	55.326	54.25	53.28	53.75	50.1	51.25
5	Bend./Tors.	69.842	69.00	71.99	73.65	66.25	68.0

Table 5.2: The first five natural frequencies(in Hz) of the plate with the hole at the root and tip. Bend. and Tors. refer to the bending and torsion mode

**Case I: Cantilevered rectangular wing with hole: aeroelastic theory**

	No Hole		Root		Tip	
	Theory	Exp.	Theory	Exp.	Theory	Exp.
$U_f$ in m/s	20.8	20.05	21.5	20.65	25.3	25.2
$\omega_f$ in Hz	10.3	11.50	8.5	9.18	8.3	9.4

Table 5.3: Theoretical and experimental flutter velocity and frequencies listed for various hole locations

In an effort to find a case where the flutter velocity is lower than the baseline case, the hole size was increased. The hole size and the amount of mass removed in the second set of design wings is 25% of the entire wing. Case II has a rectangular hole that measures  $a= 0.1048$  m(4.125 in) and  $b = 0.1143$  m(4.5 in). The hole's distance from the leading edge is 0.020 m. Otherwise, the rectangular plate's material properties and size are the same as the ones designed in Case I. Each hole is the same distance from the leading edge in the chordwise location, but varies in the spanwise location. The experimental results presented here are purely theoretical. These theoretical studies are done to find a case where the flutter velocity was lower than for the wing without a hole. One model was built for the case where flutter velocity lower than the baseline case, but the structure was not deemed safe for wind tunnel testing. In the spanwise direction,  $\delta_i$  is the distance from the root to the base of the hole, Fig 5.9.

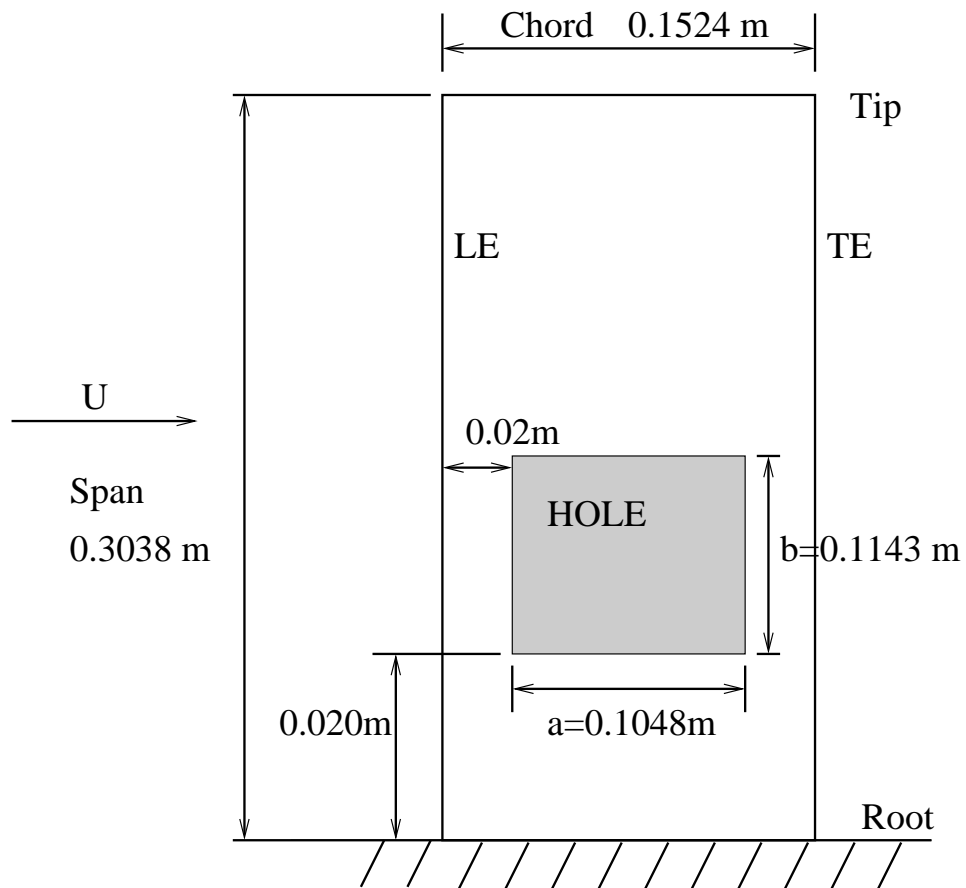


FIGURE 5.9: Clamped rectangular wing having a hole 25% of the total wing area at a distance of  $\delta = 0.020$  m, from root to the base of the rectangular hole

**Case II: Computed cantilevered rectangular wing natural frequencies**

mode no.	No Hole	Clamp	Root	Tip	Tip Max
	n/A	$\delta_1 = 0.0$ m	$\delta_2 = 0.038$ m	$\delta_3 = 0.133$ m	$\delta_4 = 0.191$ m
1	3.992 Hz	2.292 Hz	2.527 Hz	4.034 Hz	6.125 Hz
2	16.948	16.948	13.05	12.585	13.895
3	24.861	20.232	21.752	22.142	24.851
4	55.326	51.369	53.809	46.941	33.71
5	69.842	67.369	76.22	58.914	67.794
6	106.67	101.13	98.39	95.206	89.105
7	108.18	101.95	99.72	99.12	98.78
8	137.69	131.5	130.79	121.83	140.08
9	147.33	137.68	134.68	132.77	154.73
10	176.76	148.54	159.85	166.24	174.48

Table 5.4: The first ten natural frequencies of the wing with a large hole as determined by ANSYS™

**Case II: Cantilevered rectangular wing: aeroelastic theory**

	No Hole	Clamp	Root	Tip	Tip Max
	n/A	$\delta_1 = 0.0$ m	$\delta_2 = 0.038$ m	$\delta_3 = 0.133$ m	$\delta_4 = 0.191$ m
$U_f$ in m/s	20.8	18.5	19.0	32	26.2
$\omega_f$ in Hz	10.3	7.56	7.16	7.96	7.32

Table 5.5: Theoretical flutter velocity and frequency for wing with hole size 25% of the total wing area

The trend when the hole goes outward in the spanwise direction where the flutter velocity increases in Case I (hole size is 12%), is not found in Case II (hole size is 25%). In Case II, the flutter velocity is less than for the model with no hole for  $\delta_i \leq 0.038$  m, see Table 5.5. After studying the models in Cases I & II it appears that changes of the flutter velocity due to damage are dominated by the structural characteristics, in particular the bending stiffness. The bending stiffness in the plate is reduced significantly when the hole is near the root, hence the flutter velocity ( $U_f$ ) is the lowest. On the contrary, the bending stiffness is not drastically affected when the hole is near the tip and the flutter velocity is the highest. The flutter frequency ( $\omega_f$ ) is higher for the hole near the clamped root and generally decreases as the hole moves out toward the tip.

The fundamental natural frequency increases as  $\delta_i$  increases, indicating the bending stiffness is decreasing. The increase in the fundamental natural frequency can be seen theoretically and experimentally in Table 5.2. As a result, the flutter velocity increases as can be seen in Tables 5.3.

### 5.3 Aeroelastic rectangular wing models in a gust flow-field

The aeroelastic response of low aspect ratio wing models due to both periodic and random gust excitations are of interest in aeroelasticity. A better understanding of damaged wings is gained from studying the effect of a gust field in subsonic flows.

#### 5.3.1 *Experimental setup for gust generator*

Previous researchers at Duke designed and installed a low-cost, rotating slotted cylinder(RSC) to create an experimental gust field [46]. The concept for the RSC gust generators is based upon an idea by W.H. Reed III [46]. The gust generator can produce a controllable sinusoidal gust or a linear frequency sweep gust.

The rotating slot cylinder(RSC) gust generator induces “a controlled gust field in the test section by using a fixed airfoil with a rotating slotted cylinder at the airfoil’s trailing edge [46].” The RSC controls the lateral and longitudinal gust intensities. The only disadvantage is the interfering wake vortex that is created from the vortex shedding of the cylinders [46] generally positioned ahead of the wind tunnel model. A complete description of how the gust generator system works can be found in a paper by Tang, Cizmas, and Dowell [46]. For the experimental investigations in this work, two airfoils and two rotating slotted cylinders are used. A pairing of one airfoil and one cylinder is separated from the other pair by a distance of 12 inches. The damaged rectangular cantilever aeroelastic models are placed in the tunnel aft of the gust generator system.

The gust frequencies in the experiment are determined using two methods. The

first method requires emitting a laser beam through a rotating slotted cylinder and using a receptor to receive the data, and then the frequency is determined by using the HP™-5316B universal counter. The second method measures the acceleration response of the model. The gust frequency is generally the dominant frequency in the absence of nonlinearities. The time series data is collected using an accelerometer and analyzed using the Brüel & Kjaer(B&K) PULSE™ system. The frequency from both methods are nearly identical. During testing the differences were at most  $\pm 0.10$  Hz. The differences arise from the fact that PULSE™ uses two or more averages, depending on the user's specification and the counter determines the frequency without averaging.

### 5.3.2 *Gust excited nonlinearities for rectangular wings with hole*

The rectangular aeroelastic models with a hole are the same ones used earlier. Recall, the hole's location is the following: the distance  $\delta_i$  is measured from the root to the base of the hole in the spanwise(y) direction. In this work, only two models with holes are tested experimentally, one with a  $\delta_1=0.057$  m and another one with a  $\delta_2=0.152$  m.

The flutter boundary is predicted theoretically using linear aeroelastic models and validated experimentally. In linear theory, the addition of a gust field does not change the flutter prediction. Experimentally, the LCO occurred on the damaged rectangular model after the flutter boundary is exceeded. The flutter velocity and frequency for the wing with a hole 12% of the wing area at a  $\delta_1= 0.057$  m, Model A, are  $U_f= 20.65$  m/s and  $\omega_f= 9.18$  Hz. Model B is the wing with a hole at  $\delta_2=0.152$  m and it flutters at  $U_f= 25.20$  m/s and  $\omega_f= 9.40$  Hz.

The aeroelastic models are tested at various velocities below and above the flutter velocity, until the model's integrity is challenged. At the various velocities, the gust frequencies are swept from below the first structural mode to above the second

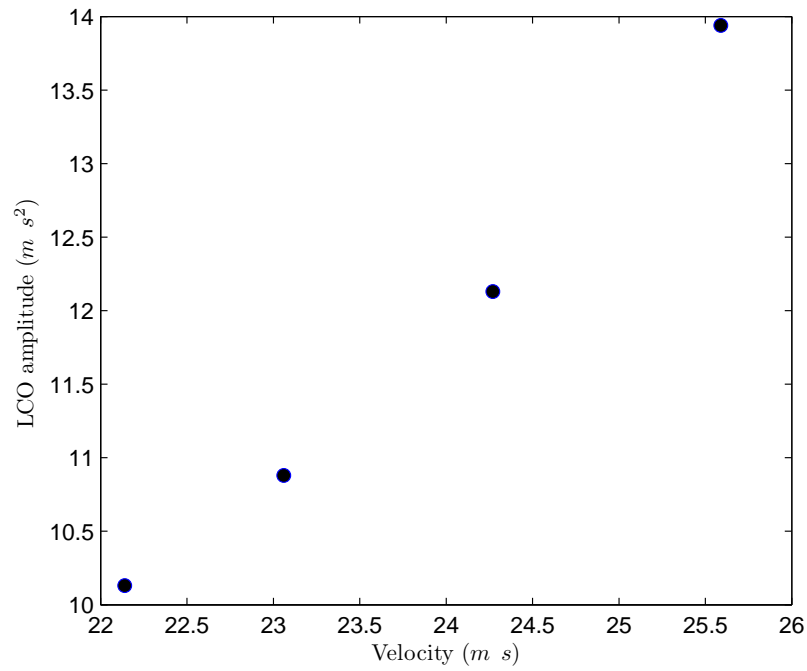
structural mode in a “tuning” exercise since the first two modes contribute the most to flutter. The tuning is a way to see how the natural frequencies change as the fluid and structure interact. The gust causes the wing to have its largest amplitude of when it is tuned with the natural frequency.

Throughout testing of damaged aeroelastic models in a gust field when nonlinearities are not present, the gust frequency dominates the fast fourier transforms(FFTs) of the wing response as seen in a representative figure, Fig. 5.11 at  $\omega_g = 13.02$  Hz. During certain experimental conditions, Model A and B appear to behave chaotically. The chaotic behavior is a significant change from the motion where the gust frequency dominated the response. Visually, the chaotic motion is observed as a broadband, multiple frequency response. In the cases where the chaotic motion occurred, the time series and its FFT are reported.

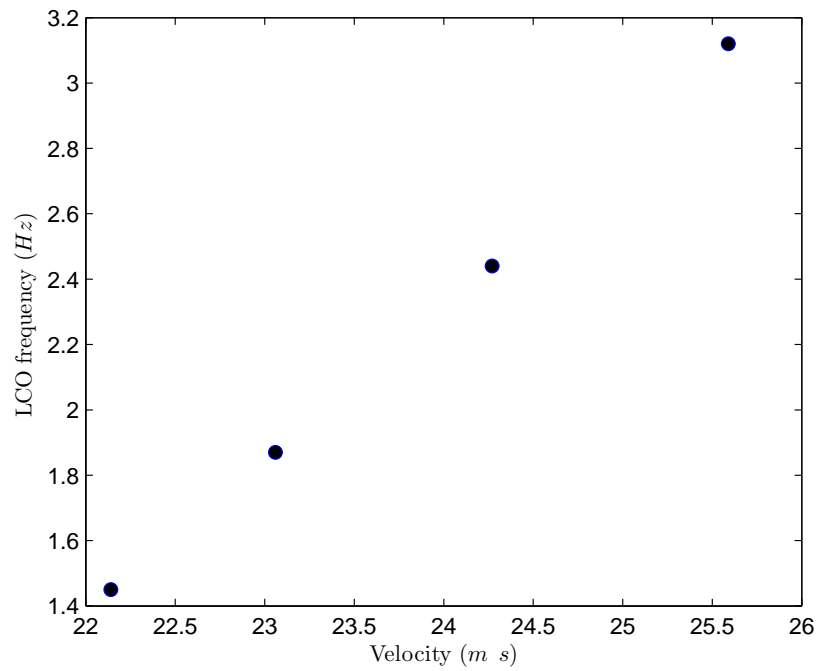
The first discovery of the chaotic behavior occurred during a frequency sweep exercise on Model A at  $U=24.80$  m/s and  $\omega_g= 10.94$  Hz as seen in Fig. 5.12. During later testing at the same flow velocity but with an  $\omega_g=5.77$  Hz, which is nearly half of 10.94 Hz, the chaotic behavior was present again as shown in Fig. 5.13. This suggests that a particular gust frequency and its harmonics excited other modes in Model A. To determine if the chaotic behavior is hole location dependent, Model B was tested with similar conditions, and the results are shown in Figs. 5.14 and 5.15. Independent of hole location, the chaotic behavior in Figs. 5.12 and 5.14 are similar for the same flow conditions to those shown in Figs. 5.13 and 5.15.

The chaotic behavior for Model A and B appears to be similar for a flow velocity that is separated by about 2 m/s but for the same gust frequencies. The similarity of behavior is seen in Figures 5.16&5.19, 5.17&5.20, and 5.18&5.21.

Studying damaged wings in a periodic gust field at a flow velocity above the flutter boundary have exposed nonlinear interactions. However in the broader field of aeroelasticity, a broadly similar phenomena have been discovered theoretically

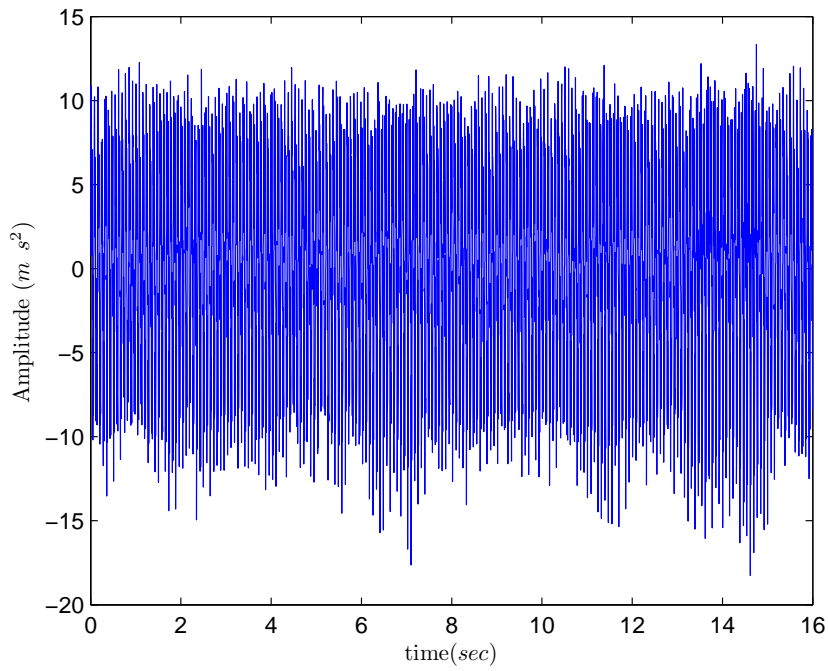


(a) LCO Amplitude vs. Flow Velocity

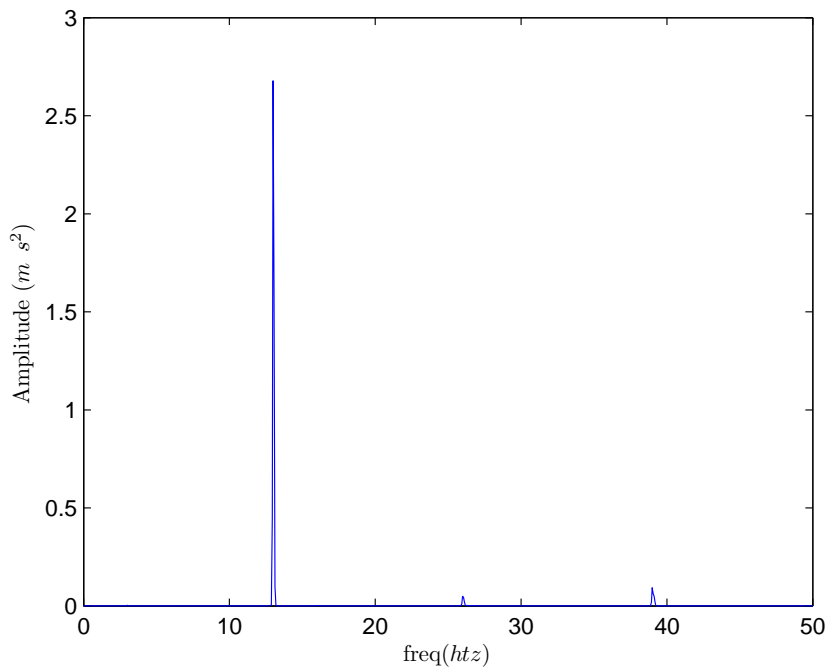


(b) LCO Frequency vs. Flow Velocity

FIGURE 5.10: LCO amplitudes and frequency vs flow velocity for Model A with hole near root( $\delta_1=0.057$  m)

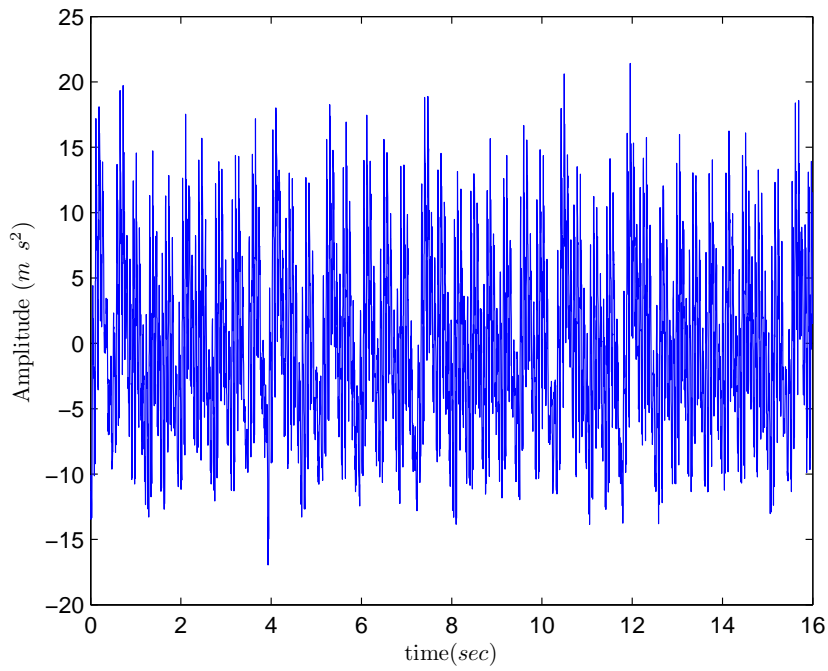


(a) **Amplitude vs. Time**

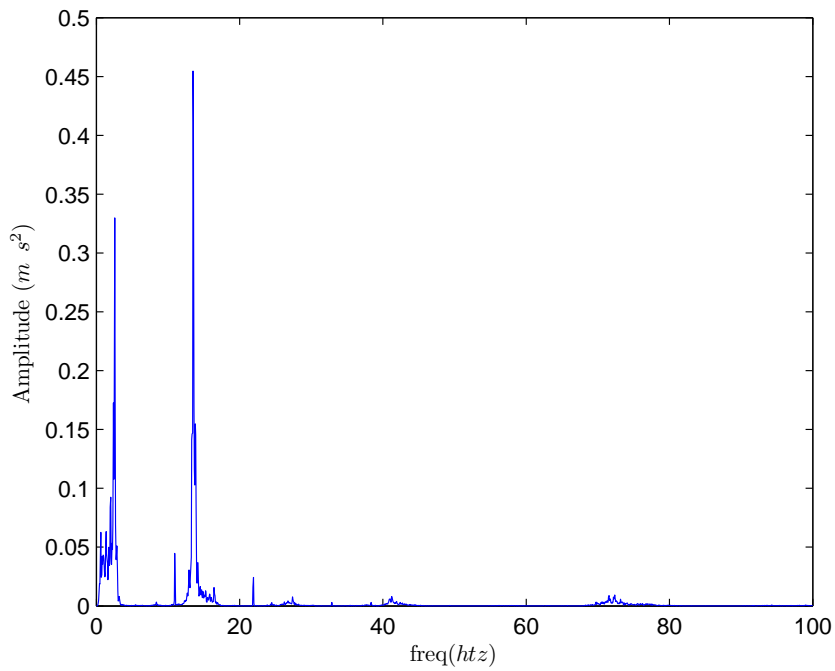


(b) **Amplitude vs. Frequency**

FIGURE 5.11: Plots of time series and FFT's of gust dominated motion for Model A with hole near root ( $\delta_1=0.057$  m) for  $U= 24.80$  m/s and  $\omega_g= 13.02$  Hz

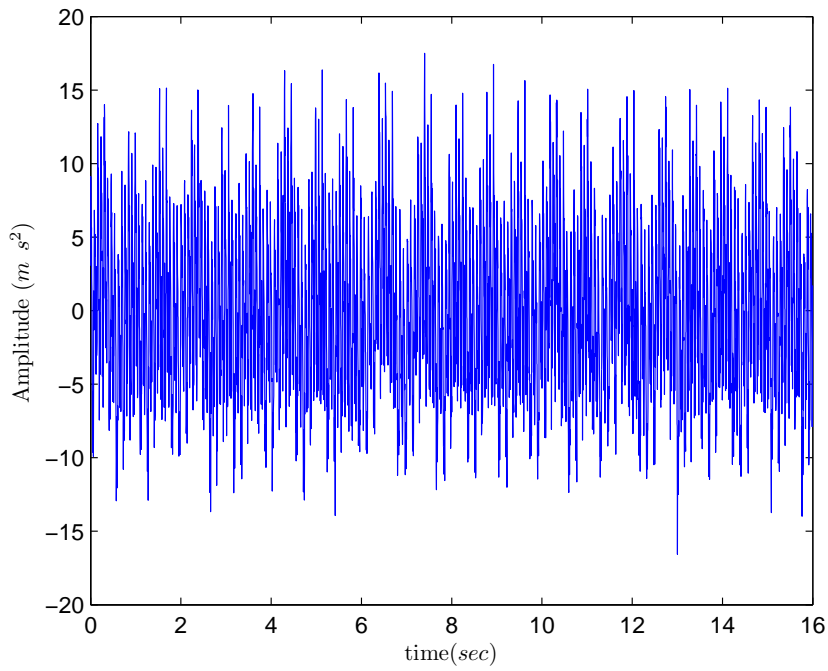


(a) **Amplitude vs. Time**

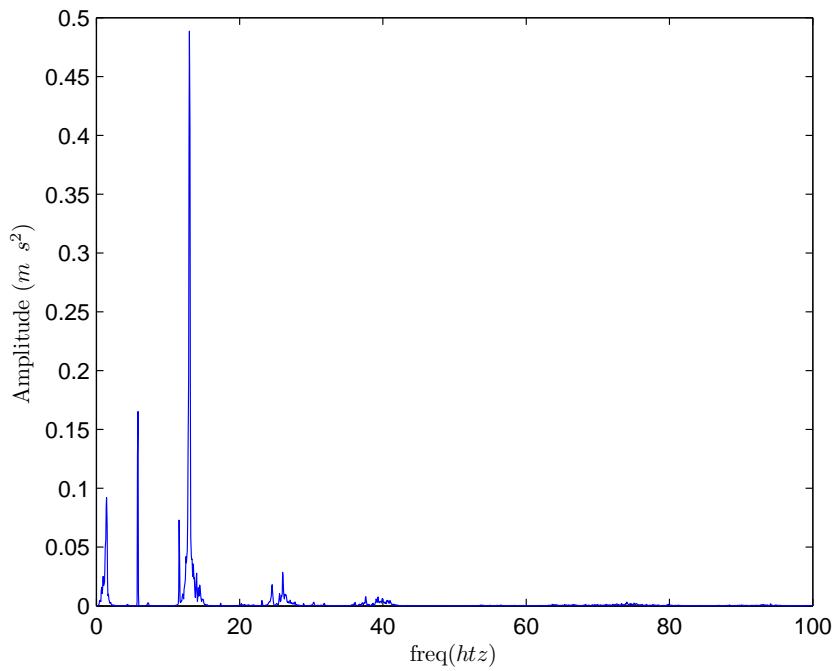


(b) **Amplitude vs. Frequency**

FIGURE 5.12: Plots of time series and FFT's of chaotic motion for Model A with hole near root( $\delta_1=0.057$  m) for  $U= 24.80$  m/s and  $\omega_g= 10.94$  Hz

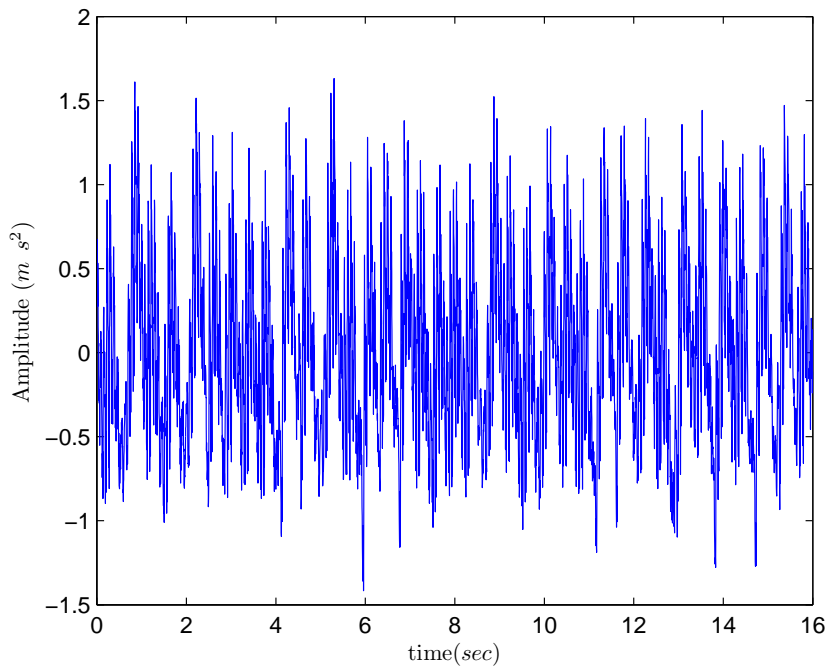


(a) **Amplitude vs. Time**

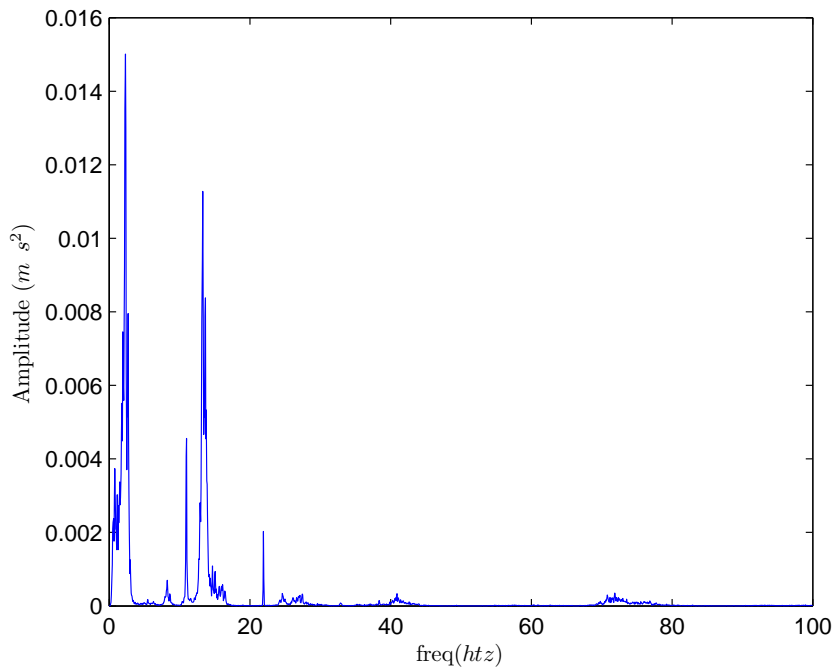


(b) **Amplitude vs. Frequency**

FIGURE 5.13: Plots of time series and FFT's of chaotic motion for Model A with hole near root ( $\delta_1=0.057$  m) for  $U= 24.80$  m/s and  $\omega_g= 5.77$  Hz

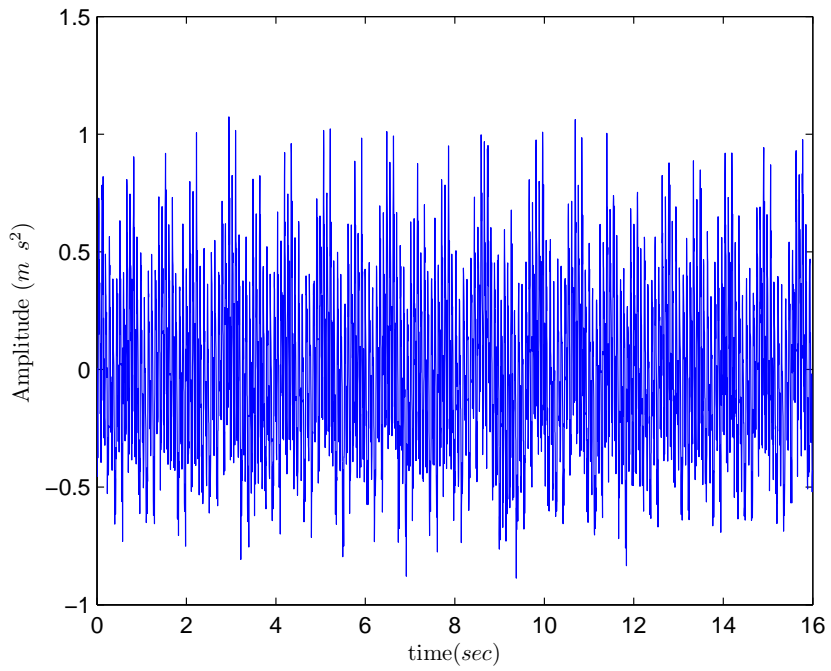


(a) **Amplitude vs. Time**

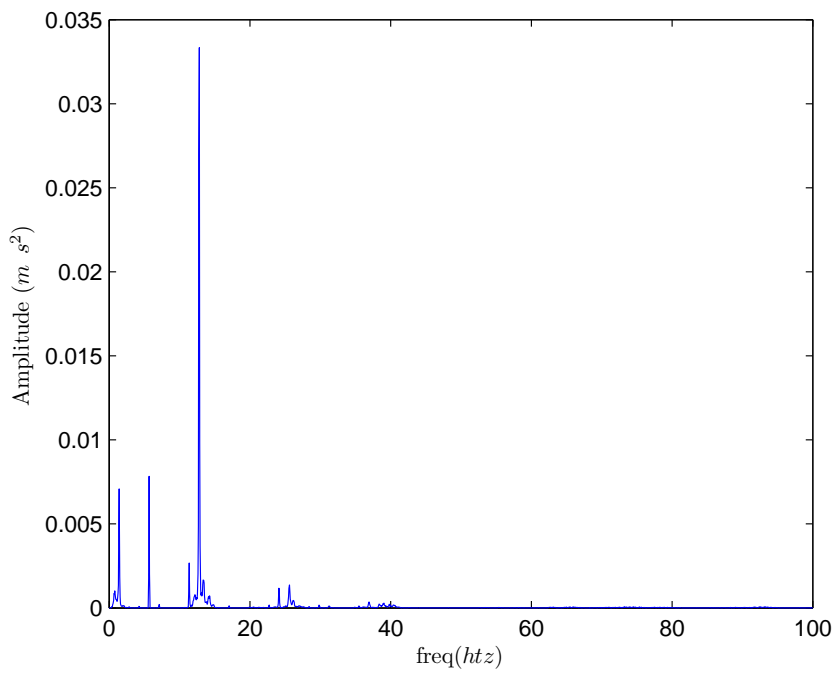


(b) **Amplitude vs. Frequency**

FIGURE 5.14: Plots of time series and FFT's of chaotic motion for Model B with hole near tip( $\delta_2=0.152$  m) for  $U= 24.85$  m/s and  $\omega_g= 10.95$  Hz

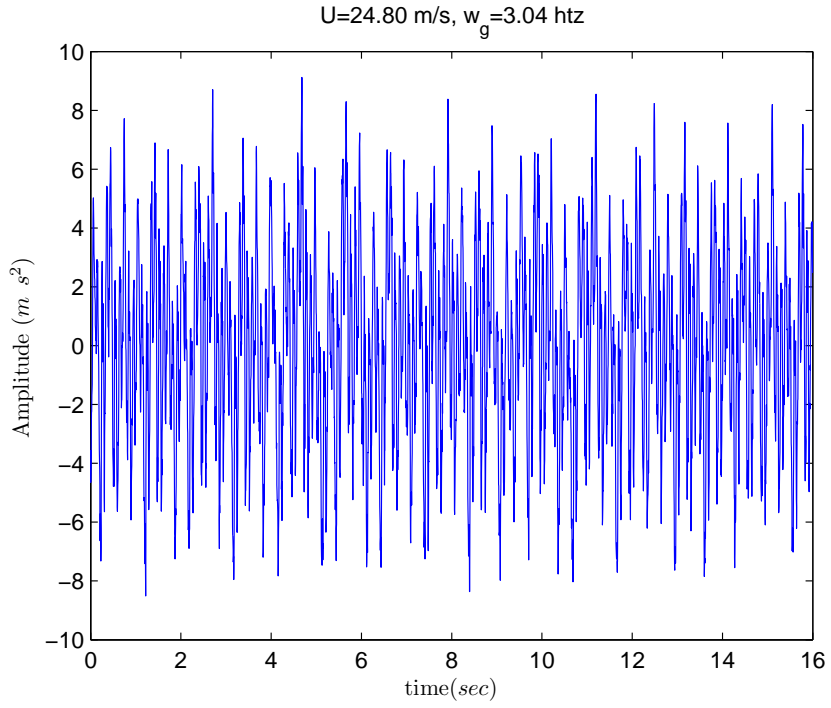


(a) **Amplitude vs. Time**

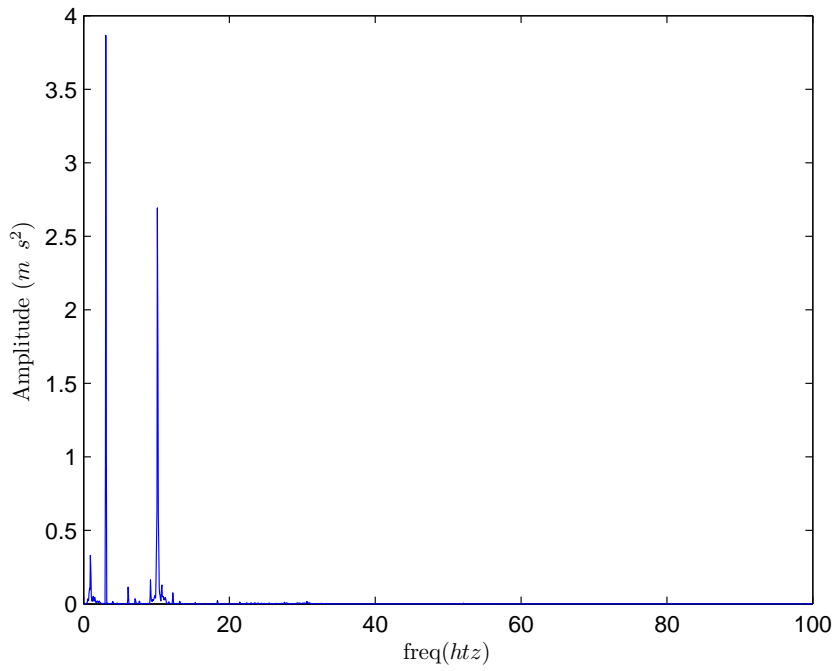


(b) **Amplitude vs. Frequency**

FIGURE 5.15: Plots of time series and FFT's of chaotic motion for Model B with hole near tip( $\delta_2=0.152$  m) for  $U= 24.85$  m/s and  $\omega_g= 5.69$  Hz

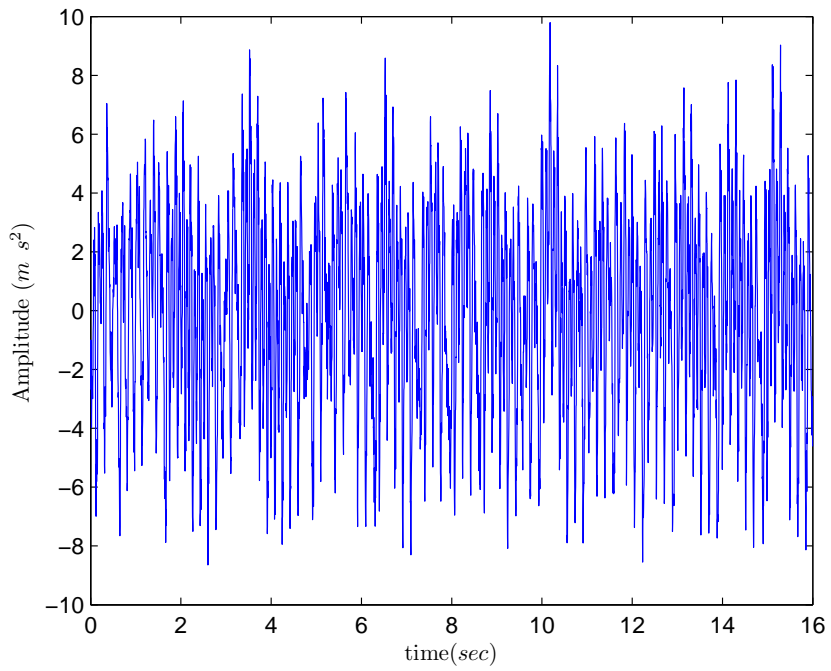


(a) **Amplitude vs. Time**

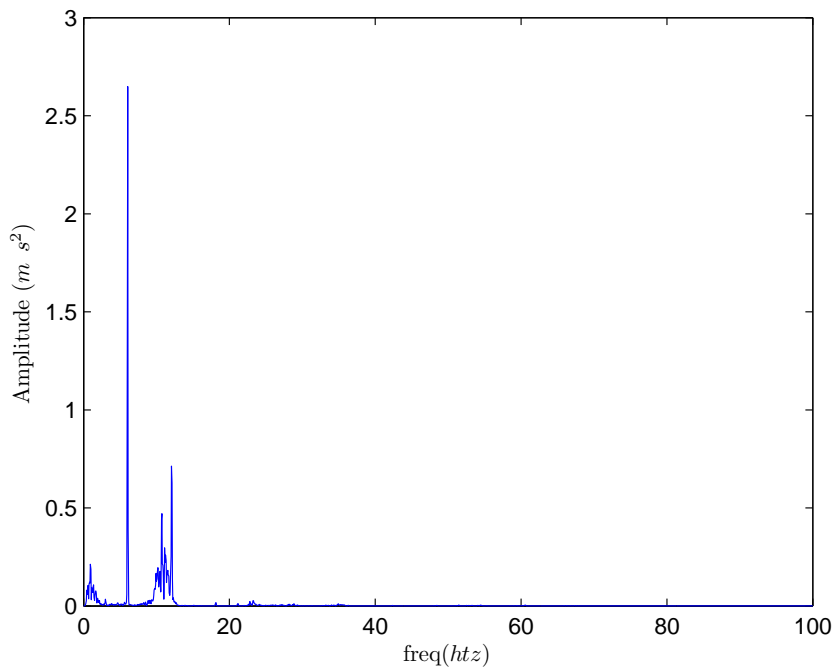


(b) **Amplitude vs. Frequency**

FIGURE 5.16: Plots of time series and FFT's of chaotic motion for Model B with hole near tip( $\delta_2=0.152$  m) for  $U= 24.80$  m/s and  $\omega_g= 3.04$  Hz

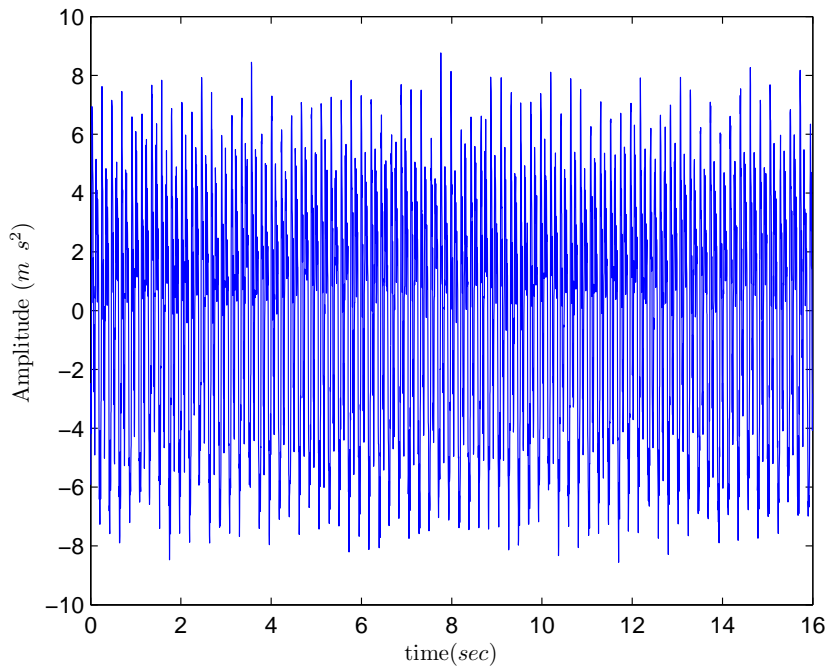


(a) **Amplitude vs. Time**

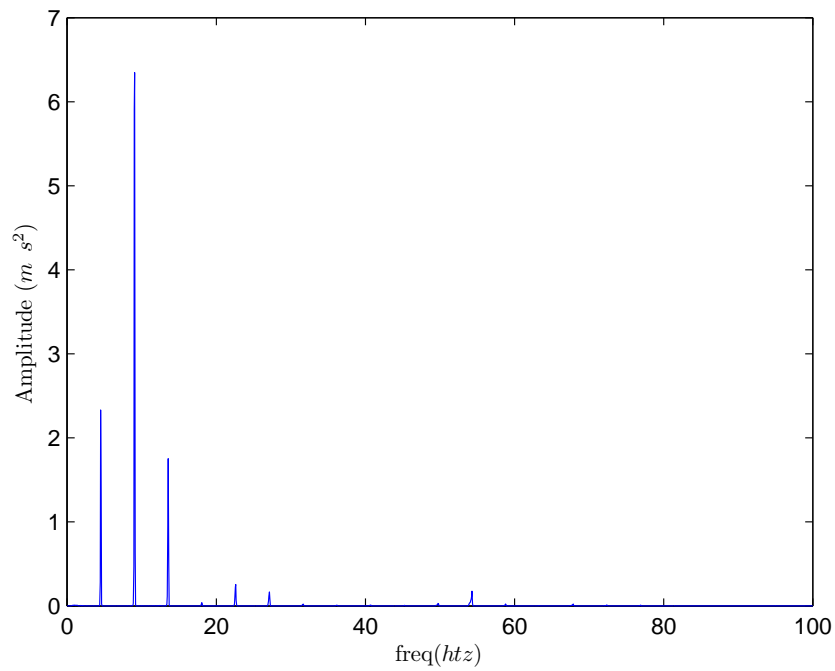


(b) **Amplitude vs. Frequency**

FIGURE 5.17: Plots of time series and FFT's of chaotic motion for Model B with hole near tip( $\delta_2=0.152$  m) for  $U= 24.80$  m/s and  $\omega_g= 6.04$  Hz

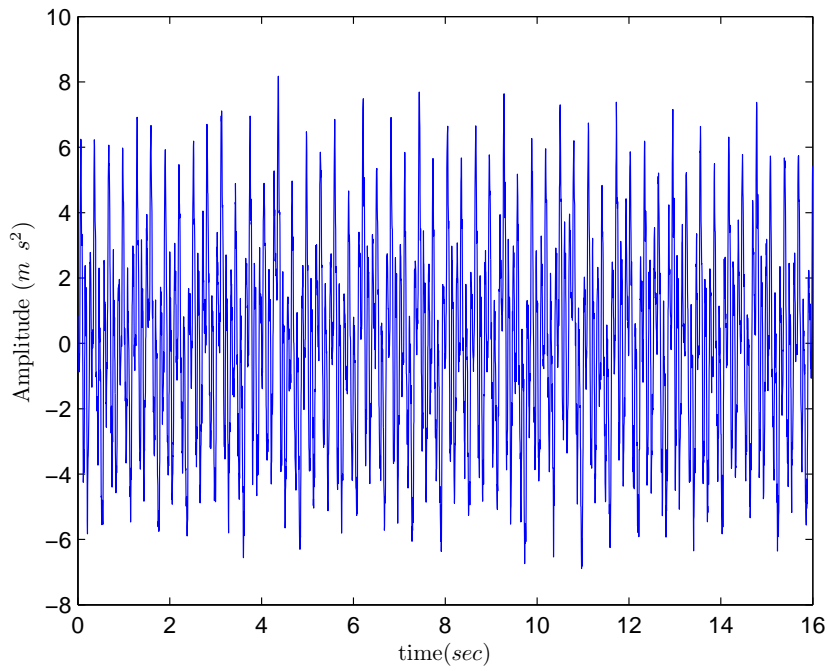


(a) **Amplitude vs. Time**

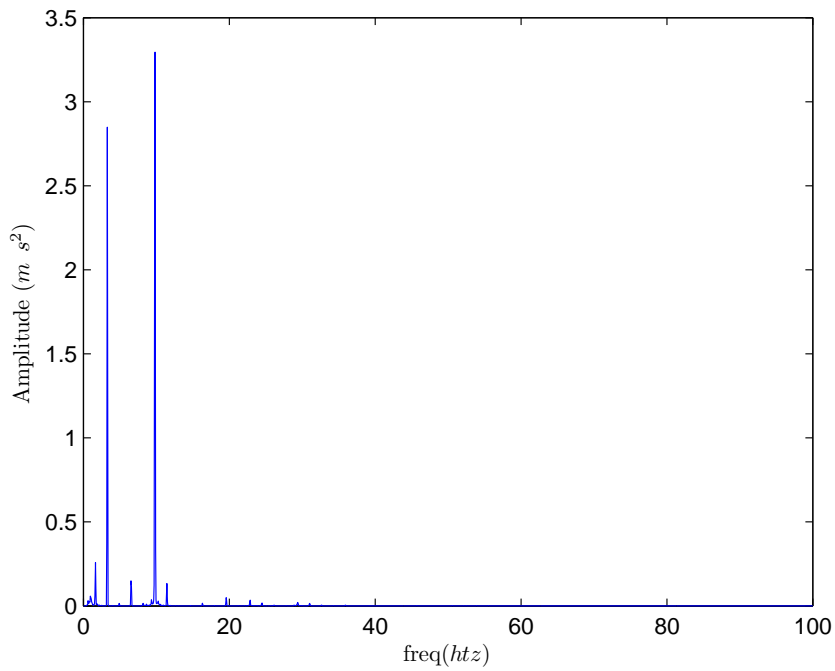


(b) **Amplitude vs. Frequency**

FIGURE 5.18: Plots of time series and FFT's of chaotic motion for Model B with hole near tip( $\delta_2=0.152$  m) for  $U= 24.80$  m/s and  $\omega_g= 9.02$  Hz

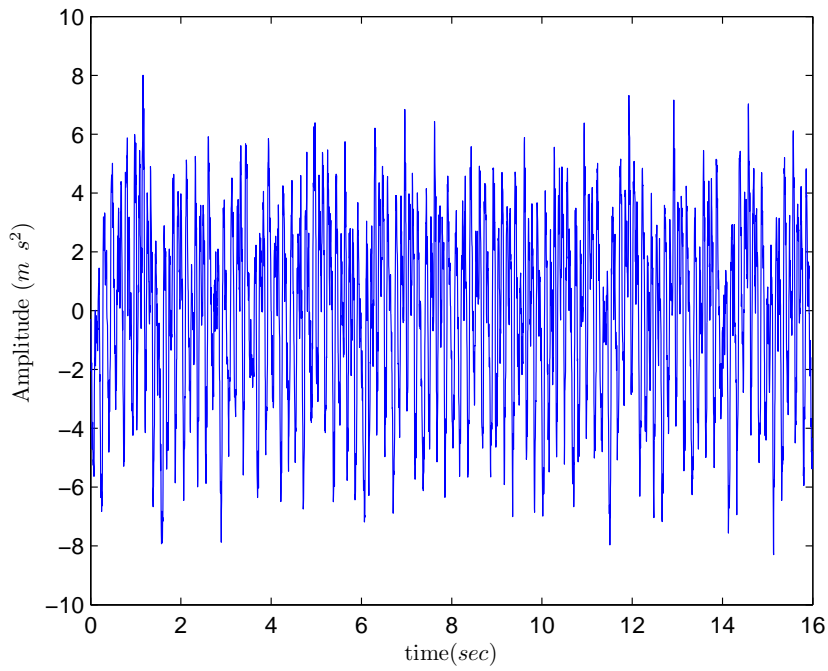


(a) **Amplitude vs. Time**

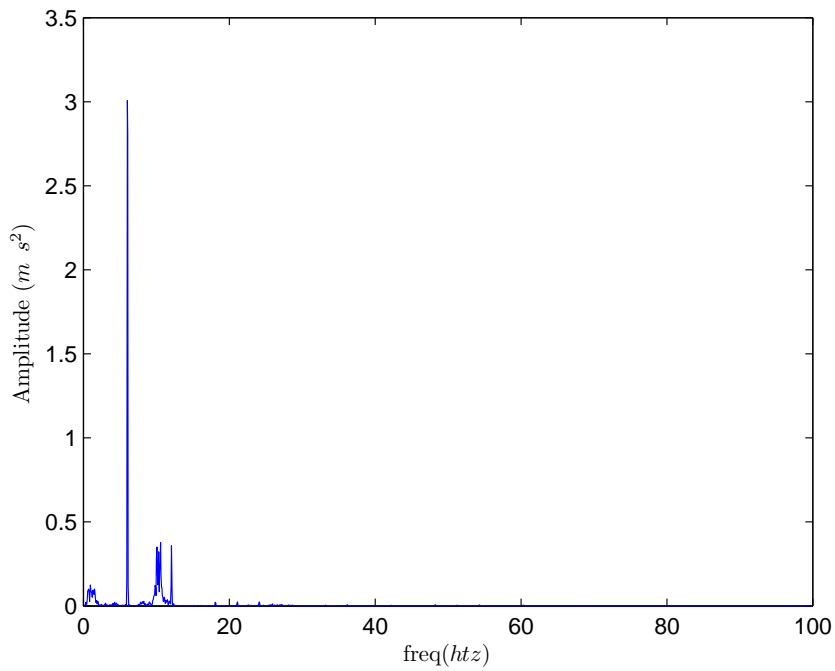


(b) **Amplitude vs. Frequency**

FIGURE 5.19: Plots of time series and FFT's of chaotic motion for Model B with hole near tip( $\delta_2=0.152$  m) for  $U= 26.52$  m/s and  $\omega_g= 3.04$  Hz

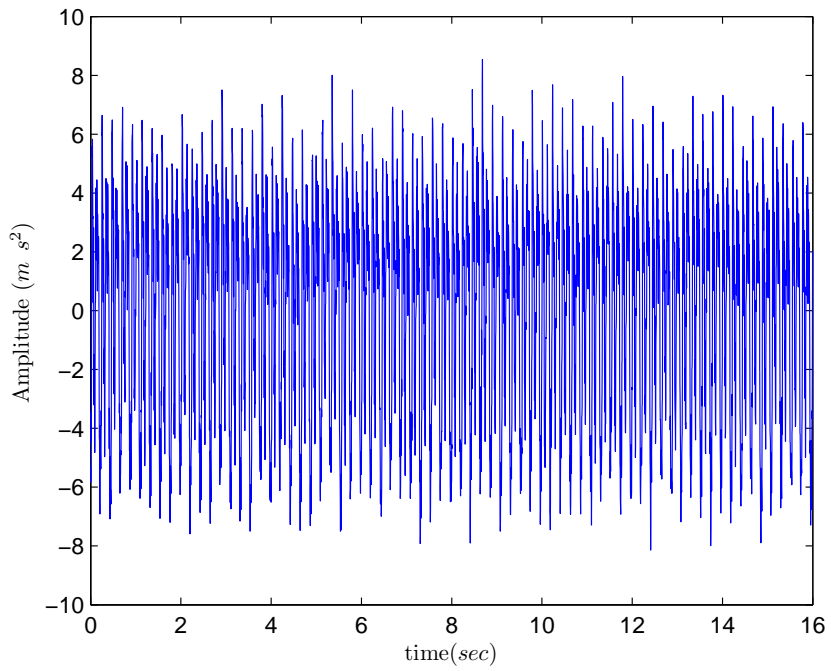


(a) **Amplitude vs. Time**

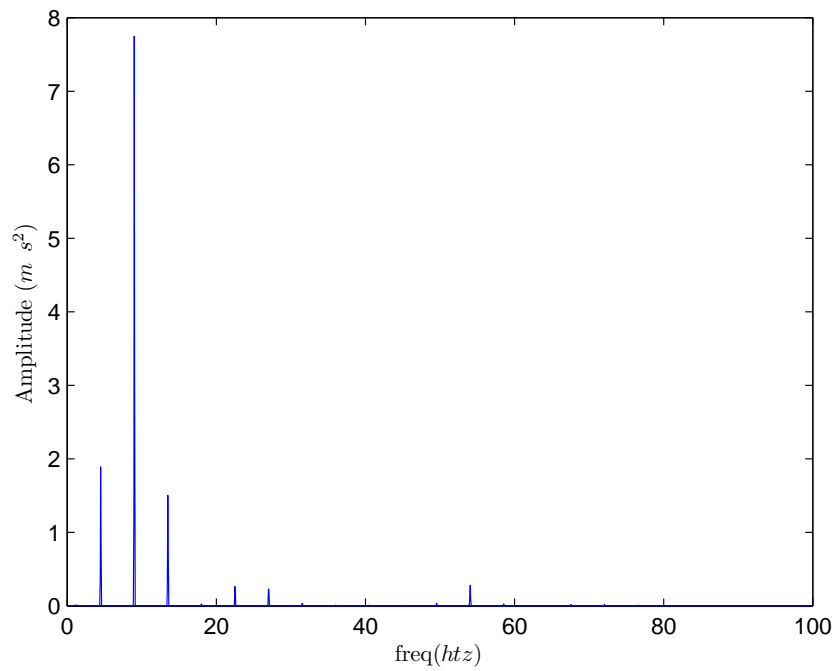


(b) **Amplitude vs. Frequency**

FIGURE 5.20: Plots of time series and FFT's of chaotic motion for Model B with hole near tip( $\delta_2=0.152$  m) for  $U= 26.52$  m/s and  $\omega_g= 6.04$  Hz



(a) **Amplitude vs. Time**



(b) **Amplitude vs. Frequency**

FIGURE 5.21: Plots of time series and FFT's of chaotic motion for Model B with hole near tip( $\delta_2=0.152$  m) for  $U= 26.52$  m/s and  $\omega_g= 9.02$  Hz

by Raveh [47] on a NACA0012 airfoil in the transonic regime. Raveh notes that a nonlinear interaction arises between the flow fields induced by the self excited aerodynamic instability, buffet, and the flow field when an airfoil oscillation is added to a buffeting flow field. The findings of Raveh are analogous to what is found here if one takes the gust to be like the prescribed airfoil motion and flutter to be like the buffeting flow field [47].

The models are tested in the wind tunnel at a chord-based Reynolds( $Re_c$ ) number between  $1.55 \times 10^5 - 3.50 \times 10^5$  which corresponds to a flow velocity between 15 m/s-34 m/s for a chord length of 0.1524 m. The higher range of the Reynolds numbers are at the low end of the beginning of the transition flow on the boundary layer of laminar and transitional flow [48]. Tang noted that some vortex shedding occurs from the apparatus used for generating gusts which adds disturbances to the flow [46]. The growth of a boundary layer on the test model may be a possible explanation for the nonlinear behavior observed in the gust flow field. Also, broadly related is an experimental investigation by Poirel on the aeroelastic typical section model of a NACA0012 airfoil where limit cycle oscillations occur in the range of chord-based Reynolds numbers,  $4.5 \times 10^4 \leq Re_c \leq 1.3 \times 10^5$  [49]. Poirel also notes that outside of these  $Re_c$ 's no oscillations are present [49].

#### 5.4 Aeroelastic analysis of cropped delta wing with hole

The F-16, a well known fighter aircraft, has a cropped delta wing planform [14, 15, 17, 16]. The dimensions of the cropped delta wing in this work are geometrically proportional to the F-16 [14, 15]. Only one cropped delta wing model has been designed after doing extensive analysis on the rectangular wing. In addition, the limitations due to machinability aided in the placement of the hole after investigating the impact of hole location theoretically.

#### 5.4.1 *Cropped delta wing structure*

The cropped delta wing (CDW) is modeled as a plate in ANSYS™ similarly to the other geometries analyzed. The material properties for the plexiglas plate are as follows:  $\rho=1217 \text{ kg/m}^3$ ,  $E=2.4\text{e}9 \text{ N/m}^2$ , and  $\nu = 0.33$ . The plexiglas has a thickness of 0.001588 m, a width(chord) of 0.254 m, and a length(span) of 0.225 m. The wing's leading edge makes a  $39.169^\circ$  angle with the y-axis as seen in the dimensional representation in Fig. 5.22. The hole in this model is along the “midchord” line and is located closer to the clamped root. The ANSYS™ results are shown in Table 5.6 for the CDW model with and without a hole. The coordinates of the hole vertices beginning in ascending order going (x1-x4,y1-y4) are the following: (0.1307 m,0.0422 m),(0.1857 m,0.0422 m),(0.2036 m,0.1125 m),(0.1625 m,0.1125 m).

The theoretical calculations are validated using a vibration test. Theoretically, the first two natural frequencies decrease for the model with the hole in comparison to the model without the hole. From the third mode and up, the theoretical values increase for the model with the hole in comparison to the model without the hole. The agreement between the theory and experiment for both cases is generally good. The sixth mode could not be found experimentally using one shaker and one accelerometer. For the experimental verification of the higher modes, often additional shakers and accelerometers are needed.

Using the V-g method previously discussed, the plexiglas cropped delta wing without a hole is designed to flutter at 37 m/s and  $\omega_f=24.5 \text{ Hz}$ . This model fluttered during wind tunnel testing at 32.2 m/s and  $\omega_f=25.19 \text{ Hz}$ . The plexiglas cropped delta wing model similarly sized with a hole is designed to flutter at  $U_f=39 \text{ m/s}$  and  $\omega_f=21 \text{ Hz}$  at zero degrees angle of attack. The model with the hole fluttered during wind tunnel testing at  $U_f=41 \text{ m/s}$  and  $\omega_f=22.98 \text{ Hz}$  at zero degrees angle of attack.

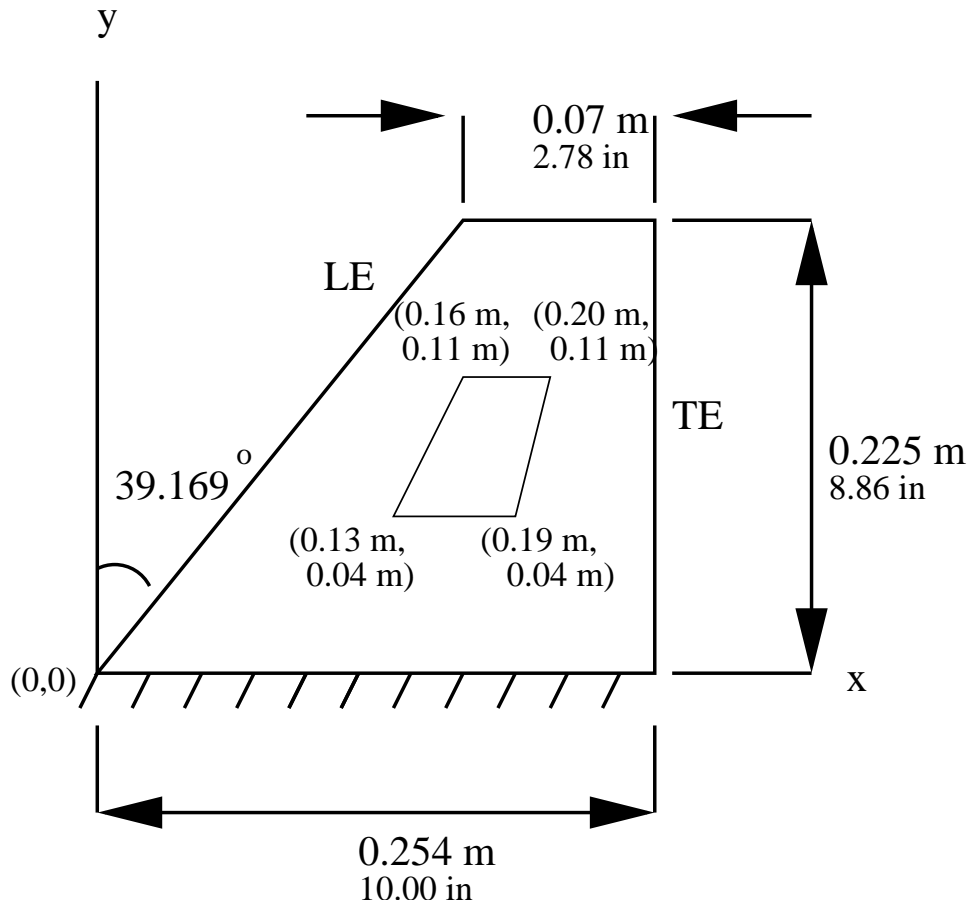


FIGURE 5.22: Dimensional representation of the cropped delta wing

Mode No.	ANSYS	Experiment	ANSYS	Experiment
	no hole	no hole	hole	hole
1	9.60 Hz	9.75 Hz	8.74 Hz	8.65 Hz
2	35.31	33.25	33.20	32.25
3	50.73	52.00	49.42	47.95
4	87.69	81.25	85.18	81.70
5	132.66	128.50	129.62	134.85
6	140.07	143.00	147.00	*
7	169.71	179.00	164.82	168.65

Table 5.6: The first seven natural frequencies as determined by ANSYS™ and the experiment for the cropped delta wing with and without a hole.

## 5.5 Conclusions from aeroelastic studies

Existing methods for modeling the aeroelastic behavior of undamaged wings without stores seem applicable to modeling damaged wings when the damage is simply a hole. In reality, if a wing is damaged by ballistics then an impulsive force would be involved that could have an effect on exciting the aeroelastic response as well. In addition, if the missile totally penetrated the wing then protruded pieces of the wing could cause severe aerodynamic shedding. The shedding may behave as a periodic air loading on the wing, broadly related to the ice problem studied by Kruger, Endruhan, and Stearman [4].

The standard methods used for aerolastic modeling includes using a finite element structural model, the doublet lattice method for aerodynamic loadings, Lagrange's equations, and the V-g method. They generally do a good job of flutter prediction. A question is what component in the aeroelastic modeling has the greatest impact on the flutter response of a damaged wing. The damage leads to a loss in structural and aerodynamics loadings which depends on the hole size. The present research indicates that the structural loss due to damage is more important than the change in aerodynamics behavior in aeroelastic modeling. Mass and stiffness play an important role in the aeroelastic behavior of a damage wing. Depending on the hole's location, the mass or stiffness effects will play a greater role than the other. Finally, after a hole is so large, structurally the integrity is challenged from its own inertial loadings before adding any external loads.

The flutter velocity for a damaged wing was found to be higher than an undamaged wing depending on the size of the hole(damage). This goes against intuition but this observation helped in better understanding the effects of mass and stiffness on flutter velocity. The fundamental natural frequency increases experimentally and theoretically as the hole goes outward in the spanwise direction, indicating the bend-

ing stiffness is decreasing. As a result, the flutter velocity increases and it can be seen theoretically and experimentally.

# 6

## Aeroelastic Studies of Wing-Store Configuration

Flutter and limit cycle oscillations(LCO) have been seen during flight tests on fighter aircraft loaded with stores(i.e. fuel tanks and missiles) [14, 15, 16]. It is difficult to evaluate all possible scenarios for which flutter and LCO may occur during flight testing because the many possible configurations of stores depend on the mission being flown. Further, flight testing is expensive, time-consuming, and can be dangerous. Therefore, good theoretical models are needed for flutter and LCO predictions to reduce the amount of flight testing or increase the productivity of any flight test program by identifying the most critical wing/store configurations.

In the present study, the impact of a store has been added to the rectangular and cropped delta wing models previously designed. The store is modeled as a slender rigid body mounted to the wing at one support. The support is rigidly attached to the wing so the store's motion is governed by the wing's motion. The store's aerodynamics are modeled using slender body theory [2].

## 6.1 Modeling the wing-store structure

The wing-store structure is modeled using the finite element method in the commercial software ANSYS™. The store has an overall length of 0.1228 m, see Figure 6.1. The ends of the store are paraboloids with a length of 0.0155 m and 0.0183 m, respectively. The store's mass is 0.0134 kg. The general configuration of the wing-store model can be seen Fig. 6.2a. The store is rigidly attached to the wing at one point,  $x_s, y_s$ .

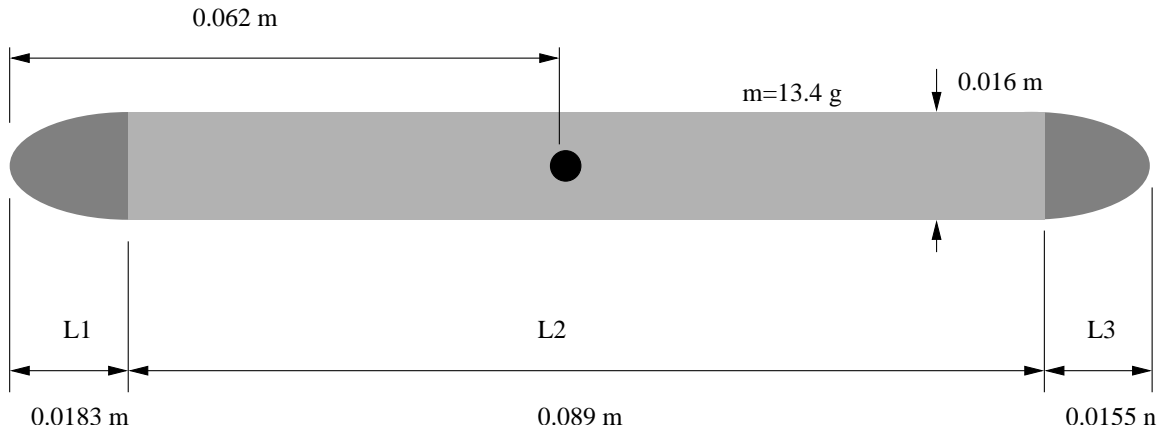


FIGURE 6.1: Physical dimensions of store in the aeroelastic models

The wing-store structural model includes only kinetic energy terms associated with the store. There is no potential energy associated with the rigidly attached store. The store's kinetic energy is  $T^\beta = \frac{1}{2}(M_1 \dot{Z}_1^2 + J_\beta \dot{\beta}^2)$  where  $Z_1$  is the displacement of the plate at the appointment point,  $M_1$  is the mass of the store,  $J_\beta$  is the polar moment of inertia, and  $\beta$  is  $dZ(x_s, y_s)/dx$

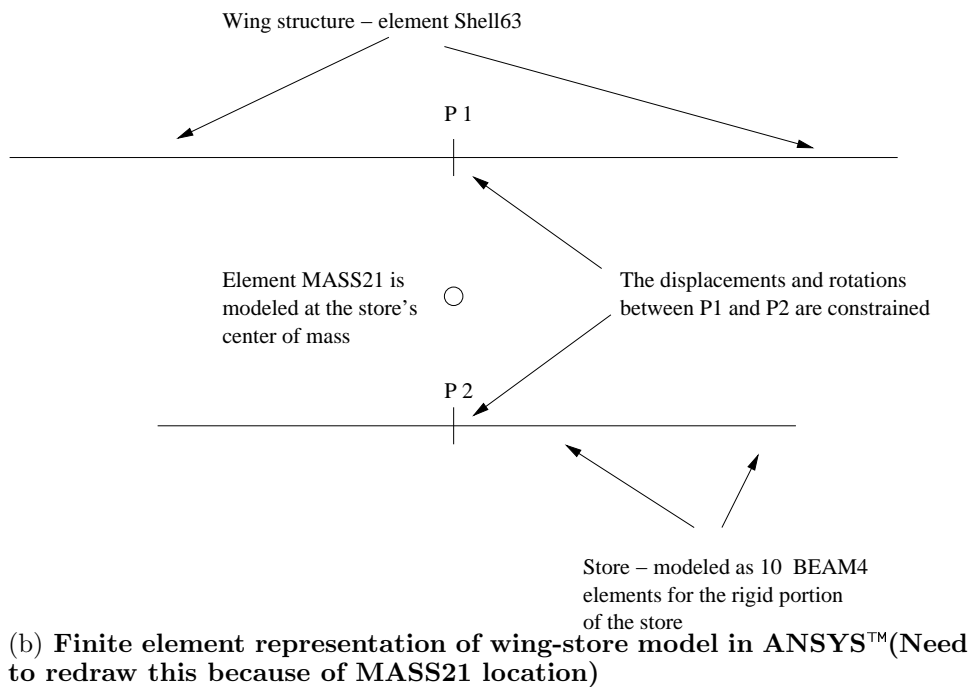
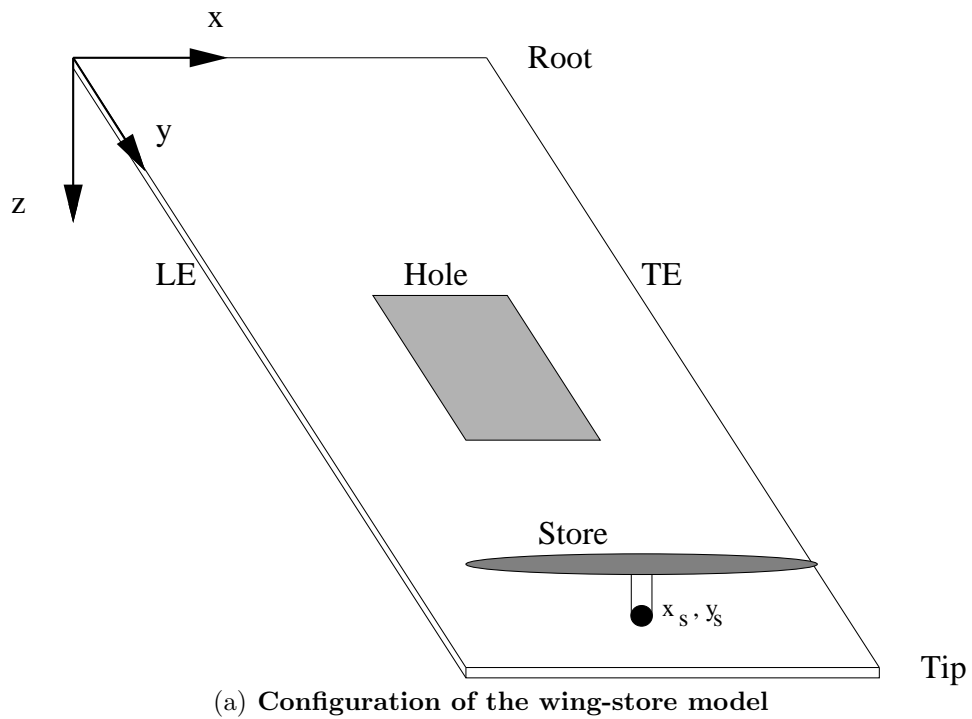


FIGURE 6.2: The experimental and theoretical representation of the wing-store model

The store is rigidly connected to the plate at the coordinate position  $(x_s, y_s)$  as in Figure 6.2a. The rigid store itself is modeled using a series of BEAM4 elements with the mass distributed evenly along the length of the store. The store is rigidly connected to the plate using the MPC184 element. “The MPC184 element is a multipoint constraint element used to apply kinematic constraints between nodes[33].” The constraints for the wing-store model enforce that the displacement and rotation of the store at  $P2$  is equal to that of the plate at  $P1$ . The MASS21 element models the store’s support between the plate and the beam elements. The wing is modeled as before using SHELL63 element. The Block Lanczos Method is used to solve the eigenvalue problem because of the constraint imposed between two elements[33].

#### *6.1.1 Structural verification of wing-store model*

The wing-store structural characteristics found using the finite element method were verified experimentally using the hammer test, vibration test, and a strobe light test. The hammer and vibration tests were described in an earlier chapter. The strobe light test was implemented to verify the second(first torsion) natural mode on the wing-store models with a hole.

The strobe light test is useful for observing the mode shape experimentally. The strobe light test requires a strobe light and a modal exciter. The electromagnetic actuator(shaker) is best suited to provide the modal excitation. The excitation of the shaker is controlled using the Brüel & Kjær (B&K) PULSE™ system. PULSE™ is setup similar to the vibration test except that the shaker generates one excitation frequency instead of a range of frequencies. The excitation frequency of the shaker is set close to the natural frequency of the structure. Additionally, the strobe light frequency is set to match the excitation of the shaker. In a dark room, the motion of the wing-store combination appears to be frozen or nearly frozen when struck by the strobe light while being excited by the shaker at one frequency at near the the

Table 6.1: Natural frequencies as determined by ANSYS™ and the experiment for the rectangular wing-store model with the hole near the tip.

	store		No store	
Mode No.	ANSYS	Experiment	ANSYS	Experiment
1	3.35 Hz	3.25 Hz	4.25 Hz	4.25 Hz
2	15.36	14.50	16.02	16.13
3	21.28	21.50	23.24	23.75
4	48.26	46.75	50.1	51.25
5	57.87	61.00	66.25	68.00
6	77.73	88.75	94.84	

natural frequency. The structure may appear to move slightly in bending, torsion, or a combination of bending and torsion when configured properly.

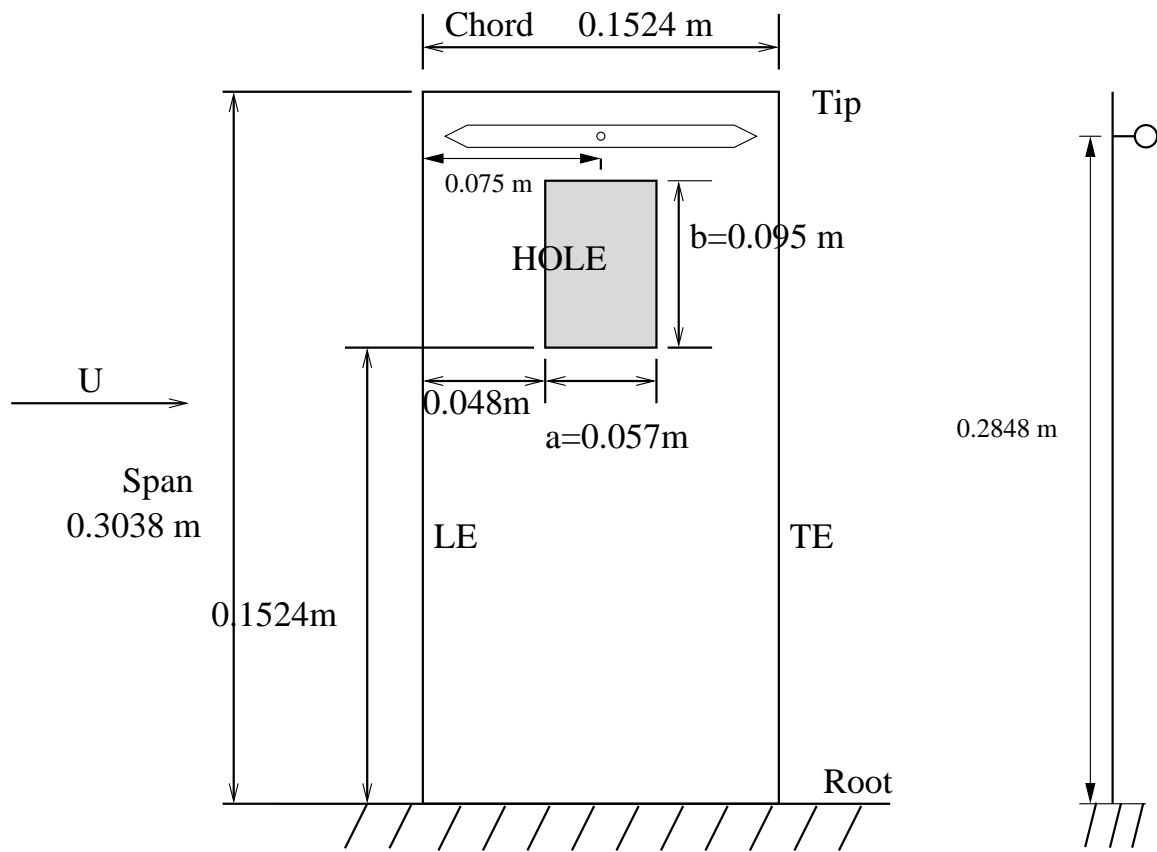


FIGURE 6.3: Cantilevered rectangular wing-store model with hole near tip

Table 6.2: Natural frequencies as determined by ANSYS™ and the experiment for the rectangular wing-store model with the hole near the root.

Mode No.	store		No store	
	ANSYS	Experiment	ANSYS	Experiment
1	2.86 Hz	2.75 Hz	3.49 Hz	3.50 Hz
2	14.55	13.25	15.08	15.50
3	22.39	22.50	24.69	25.00
4	51.28	46.75	53.28	53.75
5	63.67	66.75	71.99	73.63
6	91.52	84.25	100.47	-

The store is attached at wing location ( $x_s=0.075$  m,  $y_s=0.2848$  m) on two cantilevered rectangular wing models with a hole. The natural frequencies in Table 6.1 for the wing-store model with the hole near the tip (see Fig.6.3) decrease from the corresponding results for the case without the store. The difference between theory and experiment is less than 10% for the first five structural modes on the rectangular model with the hole near the tip. In the case where the hole is near the root (see Fig. 6.4) the natural frequencies in Table 6.2 also decrease from the case without the store. The difference between theory and experiment is less than 10% for the first five structural modes on the rectangular model with the hole near the root.

The store is attached at ( $x_s=0.208$  m,  $y_s=0.200$  m) on the cantilevered cropped delta wing-store model with a hole. Recall the cropped delta wing has a chord 0.254 m, and a span of 0.225 m. The wing-store's natural frequencies in Table 6.3 decrease from the case without the store. Theory and experiment agree well for the first three natural modes. For the fourth structural mode(second torsion), the experimental value differs by about 15% from the theoretical value. The fifth and sixth modes could not be excited in the experiment.

The store adds only inertia to the wing-store system. The stiffness of the plate remains unchanged for the wing-store system because the store cannot add stiffness based on how it attaches to the plate. The changes in natural frequencies of the

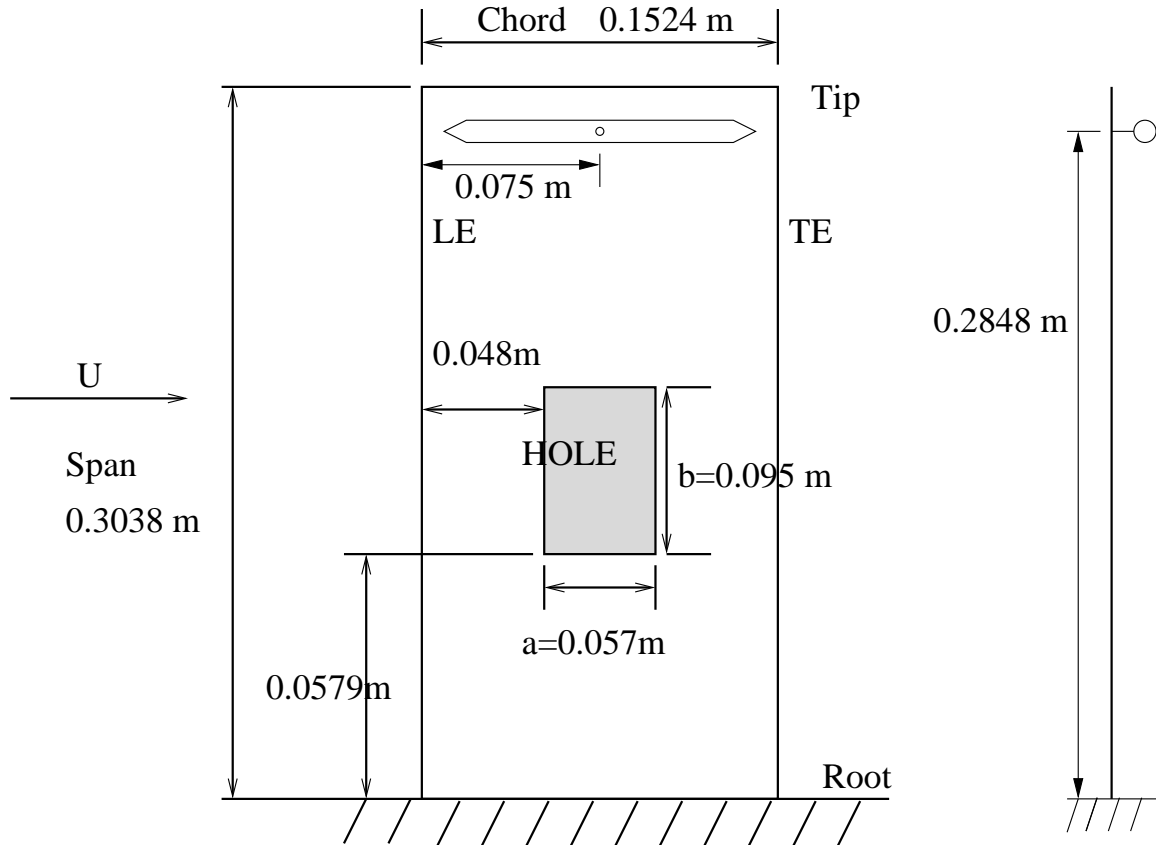


FIGURE 6.4: Cantilevered rectangular wing-store model with hole near root

wing-store combination remains relatively unchanged for all models if the store is inboard because the motion is largest in this region. As the store goes outboard, the natural frequencies decrease because of the mass effects. The largest change in natural frequencies occurs when the store is near the tip and therefore the store was placed in this region. Beam theory predicts the natural frequencies will drop because of the “mass effect” if the stiffness does not change. The theoretical and experimental results for the cantilevered rectangular and cropped delta wing-store models behave qualitatively according to beam theory as in Tables 6.1-6.3. The wing-store models clearly indicated a dropped in frequency with the addition of a store near the tip. The theory and experiment correlate well for at least the first five structural modes for the various wing-store configurations. The second (first torsion) mode is not as

Table 6.3: Natural frequencies as determined by ANSYS™ and the experiment for the cropped delta wing-store model with a hole.

	No store		store	
Mode No.	ANSYS	Experiment	ANSYS	Experiment
1	8.74 Hz	8.65 Hz	6.28 Hz	5.95 Hz
2	33.20	32.25	30.12	27.00
3	49.42	47.95	40.41	39.50
4	85.18	81.70	70.92	60.0
5	129.62	135.85	89.64	*
6	141.30	*	115.65	107.5

close but there is still good agreement considering the difference is less than 10%.

## 6.2 Slender body aerodynamics

The aerodynamics of a store body may be modeled using slender body theory if the fineness ratio criteria established by Blisplinghoff et. al[2] are satisfied. The fineness ratio is defined as the length of body divided by the width of the body. In the case of a cylinder the width is the diameter. The fineness ratio of a body must be greater than seven for slender body theory to be applicable based on experimental and theoretical investigations[2]. The fineness ratio for the designed store in Fig. 6.1 is 7.6875 therefore making slender body theory applicable for modeling the store’s aerodynamics. Often fins are attached to the store but not in this study. Fins on a store would further change the aerodynamics. The fins on the store are lifting surfaces and there is an interaction that occurs between the wing and the fins. The fins aerodynamics can be computed using a non-planar version of the doublet lattice method. However, the planar version of the doublet lattice method used in this dissertation does not have the capability to handle fins.

The support is designed to allow the store to move with the plate. The store’s deflection( $z_a$ ) is a combination of the plunge and pitch motion that is translated from the plate. In Eqn. 6.1,  $h(t) = \psi_m(x_s, y_s)$  is the deflection of the structural natural

mode( $\psi_m$ ) at the attachment point of the store( $x_s, y_s$ ). The slope of the structural natural mode at the attachment point is represented by  $\alpha(t) = \frac{d\psi_m(x_s, y_s)}{dx}$ .

$$z_a = -h(t) - \alpha(t) [x - x_b] \quad (6.1)$$

The  $x$ -coordinate of the pitch axis is noted as  $x_b$  in Eqn. 6.1. The store's downwash is calculated by substituting Eqn. 6.1 into Eqn. 6.2

$$w_a(x, t) = U \frac{\partial z_a}{\partial x} + \frac{\partial z_a}{\partial t} \quad (6.2)$$

$$dI_z = \rho S dx \left[ U \frac{\partial z_a}{\partial x} + \frac{\partial z_a}{\partial t} \right] \quad (6.3)$$

The  $z$ -component of the fluid momentum's differential associated with the store is expressed in Eqn. 6.3, [2]. The product of density( $\rho$ ) and cross sectional area( $S(x)$ ) in Eqn. 6.3 is the virtual mass per unit length of a cylinder that is modeled as the store. The differential of lift in Eqn. 6.4 is the force distribution on the store along the body length in the  $z$ -direction where  $D/Dt = U\partial/\partial x + \partial/\partial t$  is the substantial time derivative.

$$\frac{dL}{dx} = -\frac{D}{Dt} \left[ \frac{dI_z}{dx} \right] = -\rho \frac{Ds}{Dt} \left[ U \frac{\partial z_a}{\partial x} + \frac{\partial z_a}{\partial t} \right] - \rho S \left[ U \frac{D}{Dt} \left( \frac{\partial z_a}{\partial x} \right) + \frac{D}{Dt} \left( \frac{\partial z_a}{\partial t} \right) \right] \quad (6.4)$$

### 6.3 Aeroelastic behavior of wing-store combination

The structural dynamics and the aerodynamics for the wing and store combination are modeled using finite elements, the doublet lattice method, and slender body theory, respectively. The structural and aerodynamic models are coupled using Lagrange's equations.

In a linear analysis, the principle of superposition allows adding individual force components to find the total force. The aerodynamic forces of the wing-store combination are computed using the doublet lattice method for the wing and slender body theory for the store. The generalized force for the store is computed by integrating Eqn. 6.4 in  $x$  along the body's length,  $Q_i = \int \frac{dL}{dx} dx$ . The definition of virtual work for Lagrange's equation is  $\delta W = \sum_i^n Q_i \delta z_i$ . Therefore, the virtual work due to the store aerodynamics can be placed in the following form  $\delta W = \sum \int \frac{dL}{dx} \delta z_i dx$  where  $\delta z_i = -\delta\psi_m(x_s, y_s) - (x - x_b) \delta \frac{d\psi_m(x_s, y_s)}{dx}$ . The results after substitution yields a lift and moment expression created by each mode and these can be added to the aerodynamic loadings on the wing in each mode. The derived lift and moment expression are identical to the ones found by Blisplinghoff et. al[2].

### 6.3.1 Results from wing-store aeroelastic analysis

The store's impact for the present aeroelastic wing-store models is larger on the structural dynamics than the aerodynamics. The magnitude of the generalized forces caused by the wing-store combination is affected little by the store's aerodynamics. The store's aerodynamics would have been greater if the store included fins. The store's impact on the wing's structure is largely due to the influences cause by the additional mass that is added by the store. In Tables 6.4 and 6.5, the aeroelastic flutter velocity and frequency for the wing with hole and store are reported. The cropped delta wing model results are reported in Table 6.6.

#### **Cantilevered rectangular wing-store model with hole near root**

	No store(hole)		Store(hole)	
	Theory	Exp.	Theory	Exp.
$U_f$ in m/s	21.5	20.65	20.25	19.05
$\omega_f$ in Hz	8.5	9.18	8.36	7.00

Table 6.4: Theoretical and experimental flutter velocity and frequencies

**Cantilevered rectangular wing-store model with hole near tip**

	No store(hole)		Store(hole)	
	Theory	Exp.	Theory	Exp.
$U_f$ in m/s	25.3	25.2	22.7	23.52
$\omega_f$ in Hz	8.3	9.4	7.18	8.63

Table 6.5: Theoretical and experimental flutter velocity and frequencies

**Cantilevered cropped delta wing-store model with a hole**

	No store(hole)		Store(hole)	
	Theory	Exp.	Theory	Exp.
$U_f$ in m/s	39	41	36.8	37.19
$\omega_f$ in Hz	21	22.98	18.3	16.50

Table 6.6: Theoretical and experimental flutter velocity and frequencies

## 6.4 Conclusions from wing-store analysis and experiment

Overall, the methods explored to determined the flutter boundaries for a wing with a store and a hole are valid for configurations examined. The agreement between theory and experiment is generally good. The store provides more changes in the structural models than the aerodynamics of the store in the absence of fins. In particular the store adds mass and not stiffness to the system.

# 7

## Summary

### 7.1 Conclusions

In this dissertation, each major area associated with modeling flutter for a wing with a hole was investigated independently theoretically and experimentally. It was shown that existing methods for modeling the structural dynamics, the aerodynamics, and the aeroelastic behavior can be used to design successful wind tunnel models for a lifting surface with a hole.

The wings with a hole examined in the various models were modeled as a plate-like structure using the finite element method(FEM) in the commercial software ANSYS™. Various shape plates with a hole in different locations were accurately modeled using FEM according to the results from the structural dynamics test independent of materials. The difference between theory and experiment for the first five natural modes were no larger than 10% for all models evaluated except for one model. The exception was the cropped delta wing with a store and a hole. In this model, the fourth mode is off by about 15%.

The aerodynamics for a wing with a hole was investigated theoretically using the doublet lattice method. A novel approach was implemented to account for the

pressure difference across the wing with a hole. The approach made it easier to calculate the aerodynamic loading using the doublet lattice method. Writing the doublet lattice aerodynamic code in house provided a lot of insight into understanding the approximations used by Rodden and et. al in the quartic approximation and the substitution of the vortex lattice method. The aerodynamics for a wing with a hole was tested using an experiment in steady flow at various angles of attack. The experimental aerodynamic model with a hole correlated nicely with the coefficient of pressure predicted according to theory in the chordwise direction at a constant span location. The coefficient of pressure in the spanwise direction agreed closer with the theory in the spanwise direction near the leading edge. As the pressure taps went further back on the wing, the results were not as good due to the instrumentation inability to measure such a small pressure difference in the spanwise direction.

The aeroelastic equations of motion derived using Lagrange's equation to couple the FEM structural model and the aerodynamic model worked well. The comparison between theory and experiment for a wing with a hole is good and that the methods examined are valid. This is useful because the methods used here are typical to the ones used in industry to determine flutter.

## 7.2 Future Work

The main objective was accomplished in the dissertation. However, during the research other interesting questions arose that will be of great potential benefit to the engineering community in research and in practice. A short list of future research areas that will be beneficial follows.

- Conduct a time domain analysis
- Consider the non planar version of the doublet lattice method
- Determine the aerodynamic and aeroelastic behavior using a commercial code

During this research, the problem was analyzed in the frequency domain instead of the time domain with the doublet lattice method. It is well noted that the calculation of aerodynamic loads in the frequency domain is computationally efficient. However self-excited periodic aerodynamic loading caused by the hole is worth considering. These periodic aerodynamic loads are sometimes called buffet. Computations performed in the time domain can model the nonlinear behavior of these self-excited aerodynamic oscillations. The time domain model is also capable of computing the nonlinear behavior caused by gust and the time domain computation may be able to account for the impulsive forces at impact. One time domain model that may be a good starting point is the vortex lattice method if the researcher is able to devise a way not to violate the vortex theorems that provides the basis of the code. However, a computational fluid dynamics(CFD) code for the Navier-Stokes equations will be required to describe buffet.

The aerodynamic loads in this work were determined using the planar version of the doublet lattice method. The planar version of the doublet lattice method has a few limitations. The non-planar version of the doublet lattice method is capable of modeling more than the wing, e.g. it can model the fins on the missiles and it can model the wind tunnel walls. Modeling the fins on the missiles could provide insight on the interaction between the wing's lifting surface and the stores. Modeling the wind tunnel walls could provide insight into a wall correction factor.

In industry, aerodynamic and aeroelastic analyses are often done using commercial codes except for specific applications where an in-house code is used for advance technologies specific to a company. The aerodynamic and aeroelastic analysis of wing could be done with a widely used commercial code, like MSC<sup>TM</sup> Nastran. The commercial codes are very powerful. However, there exist occasions where a user is not fully aware of the assumptions in such codes and therefore make bad calculations. The code developer is usually aware of the assumptions, but they are not the ones

generally using the code to make calculations to design an airplane. However, it is encouraging that a commercial code was able to generate the structural model for a plate with a hole and correlate well with the experiment.

# Appendix A

## Appendix

### A.1 Aerodynamics of a wing with a hole

Incorporating the aerodynamics of a wing with a hole can be performed using the doublet lattice method. The simplified approach outlined in Chapter 4 comes from the following derivation. Recall, that for an entire wing the pressure jump is proportional to the local doublet strength,  $\bar{w}_j = \sum_{j=1}^n D_{ij} \bar{p}_j$ . In order to find the pressure across the wing with the hole, initial thoughts would be to rearrange the aerodynamic influence coefficient matrix,  $D$ , to find the find pressure on the wing, see Eqn. A.1.

$$\begin{Bmatrix} w_{wing} \\ w_{hole} \end{Bmatrix} = \begin{bmatrix} A_{wing \text{ on } wing} & A_{wing \text{ on } hole} \\ A_{hole \text{ on } wing} & A_{hole \text{ on } hole} \end{bmatrix} \begin{Bmatrix} p_{wing} \\ p_{hole} \end{Bmatrix} \quad (\text{A.1})$$

The  $w_{wing}$  is prescribed and  $p_{hole}$  is known to equal zero. The pressure is not zero across the wing, but it equals zero across the hole. In this dissertation, the  $w_{hole}$  is not needed. Equation A.1 can be rearranged into the following expressions, Eqns. A.2 and A.3.

$$\begin{Bmatrix} w_{hole} \end{Bmatrix} = [A_{hole \text{ on } wing}] \begin{Bmatrix} p_{wing} \end{Bmatrix} + [A_{hole \text{ on } hole}] \begin{Bmatrix} p_{hole} \end{Bmatrix} \quad (\text{A.2})$$

$$\{ w_{wing} \} = [A_{wing \ on \ wing}] \{ p_{wing} \} + [A_{wing \ on \ hole}] \{ p_{hole} \} \quad (A.3)$$

Equation A.3 clearly demonstrates that the pressure on the wing can be calculated alone since the wash on the wing is known. Therefore, the novel approach with the substitution to account for the hole in the wing is valid and is implemented more readily computationally using the expression as seen below from Chapter 4.

$$\begin{Bmatrix} w_1 \\ 0 \\ \vdots \\ w_{n-1} \\ w_n \end{Bmatrix} = \begin{bmatrix} D_{11} & D_{12} & \cdots & D_{1(n-1)} & D_{1n} \\ 0 & 1 & 0 & 0 & 0 \\ \cdots & \cdots & \cdots & \cdots & \cdots \\ \vdots & \vdots & \vdots & \vdots & \vdots \\ D_{n1} & & \cdots & & D_{nn} \end{bmatrix} \times \begin{Bmatrix} p_1 \\ p_2 \\ \vdots \\ p_{n-1} \\ p_n \end{Bmatrix} \quad (A.4)$$

## A.2 Overview of aeroelastic analysis

The aeroelastic analysis is organized according to the flow charts in Figs. A.1 and A.2. The computational aeroelastic code is written in MatLab™ except for the portion used to calculate the structural dynamics behavior in ANSYS™. Only the main finite element code and the aeroelastic codes are included as a sample.

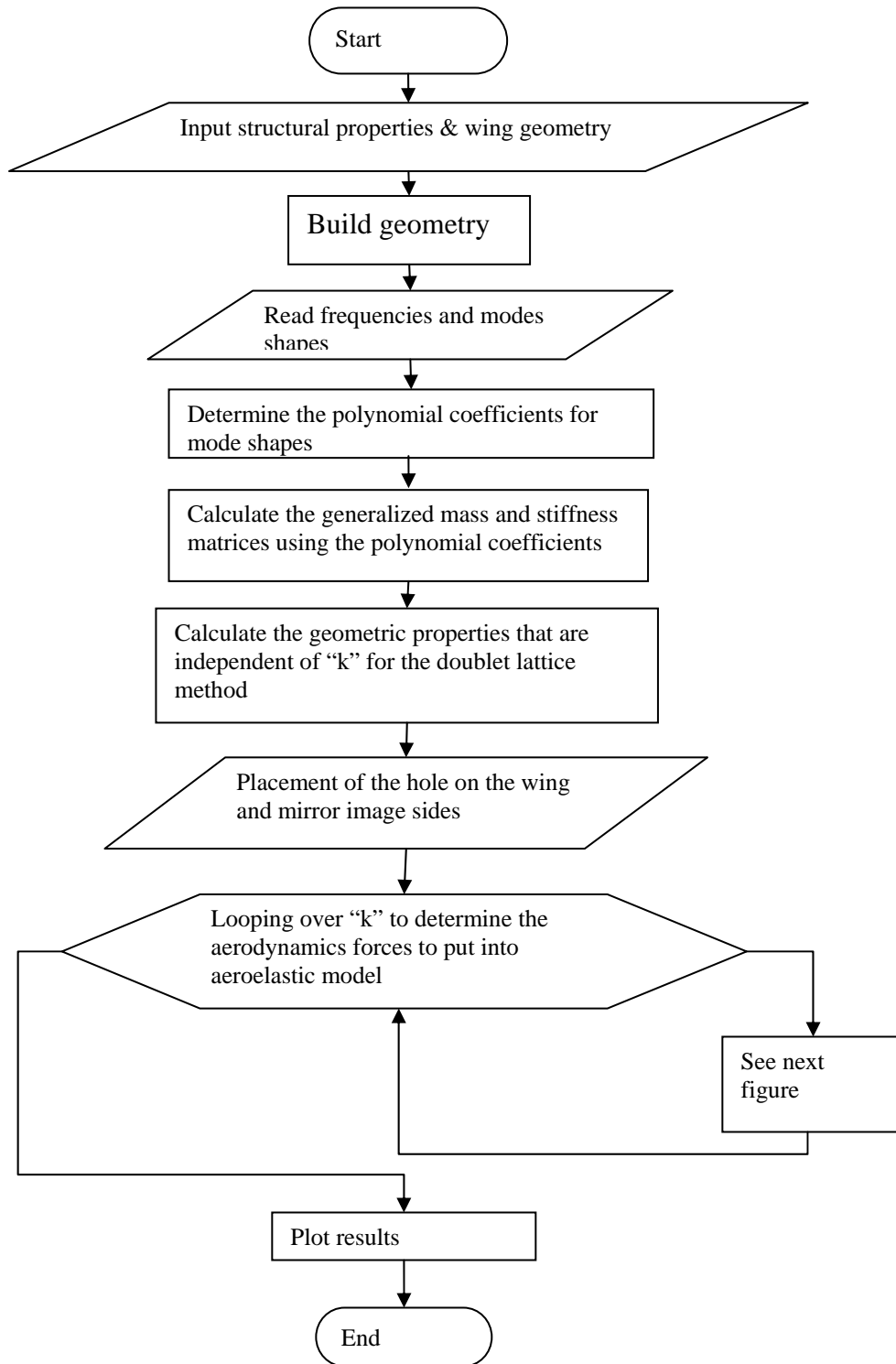


FIGURE A.1: Flowchart of flutter code

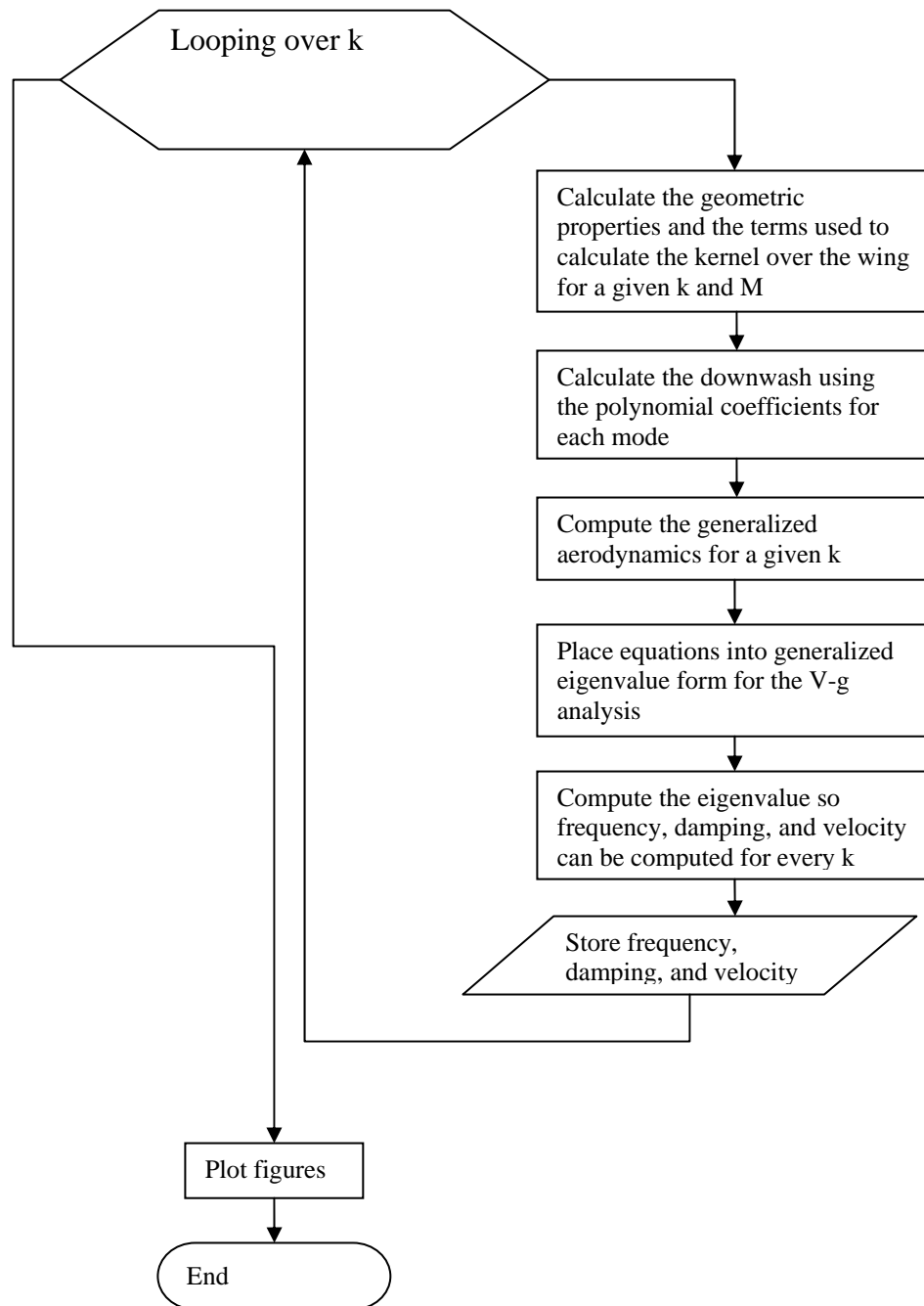


FIGURE A.2: Flowchart of flutter code with an emphasis on the aeroelastic portion

### A.3 Sample ANSYS™ file

This is a sample ANSYS™ finite element code to calculate the structural behavior of a cropped delta wing plate with a hole. Other geometries and materials can be analyzed by making minor modifications to the code

```

/BATCH
%! Ansys code to calculate the natural frequencies for a CDW
  cantilevered plate!
/Show                               %! Turns on the GUI version of
  ANSYS
%/menu, on
/PREP7
ET,1,SHELL63
R,1,.001588,0.001588,0.001588,0.001588,,, %! Thickness in m
MPTEMP,1,0                            %! Temperature is neglected
MPDATA,EX,1,,2.54e9                    %! Young's modulus in Pa
MPDATA,PRXY,1,,0.33                    %! Poisson's Ratio
MPDATA,DENS,1,,1190                     %! Density in kg/m^3
PTXY,0,0,0.254,0,0.254,0.225,0.183,0.22 %!(X,Y) Coordinates
  of the Cropped Delta Wing Vertices - 10 in chordPOLY
                                          %!(
      Actually makes the area
PTXY,0.101,0.01,0.161,0.01,0.161,0.071,0.101,0.071 %!
  Coordinates of hole vertices
POLY                                     %! makes the Hole
ASBA,1,2                                 %! Hole-Subtracts Area 2 from
  Area 1
LLIST                                    %! Shows me the lines and there
  reference #
ALIST                                    %! Shows the areas there
  reference #
LESIZE,1,,,30,,,,,0                    %! Meshing Commands
LESIZE,2,,,30,,,,,0
LESIZE,3,,,30,,,,,0
LESIZE,4,,,30,,,,,0
LESIZE,5,,,15,,,,,0                    %! Hole-LESIZE is the Element
  Size
LESIZE,6,,,15,,,,,0                    %! Hole-
LESIZE,7,,,15,,,,,0                    %! Hole-
LESIZE,8,,,15,,,,,0                    %! Hole

SMRT,1
AMESH,ALL

```

```

FINISH                                %! Defining the Boundary
    Conditions along root chord
/SOL
FLST,2,1,4,ORDE,1                    %! Picks the Bottom Linw
FITEM,2,1
/GO
DL,P51X,,ALL,0                        %! Boundary Condition for 0
    displacement
FINISH

/SOLU                                  %! Enters the Solution Processor
ANTYPE,2                               %! Modal Analysis
MODOPT,SUBSP,10                       %! Subspace, 10 modes
EQSLV,FRONT                           %! Frontal Solver
MXPAND,10                              %! Expand 10 modes
SOLVE
FINISH

/POST1                                 %! List Solutions
SET,LIST
!/VIEW,1,1,3,3                        %! Change to oblique view to see
    mode shape
SET,FIRST                              %! Displays first mode shape
PLDISP
PLNSOL,UZ,1                            %! Makes contour plot of out-of-
    plane disp.
ANMODE,10,0.1,,0                     %! Animate mode shape
SET,LIST
num_mod1=10
xywrite=1                              %!collecting the natural modes
    and frequencies
*GET,NMAX,NODE,,NUM,MAX               %!Get the Max Number for Nodes in
    problem

/PREP7
*if,xywrite,eq,1,then
*DIM,xycoord,ARRAY,NMAX*num_mod1,2,1,, %!NMAX will be the number
    of rows, to find x,y coordinates
*vlen,NMAX,1
*do,i_,1,num_mod1,1
*vget,xycoord((i_-1)*NMAX+1,1),node,1,LOC,x,,2
*vget,xycoord((i_-1)*NMAX+1,2),node,1,LOC,y,,2
*enddo
*endif

```

```

/POST1
*DIM, freq ,ARRAY,num_mod1,1,1,,
*Dim, modval ,ARRAY,NMAX*num_mod1,1,1,,
*do, i_ ,1 ,num_mod1,1
*GET, freq (i_ ,1) ,MODE,i_ ,FREQ
subset ,1 ,i_
*vlen ,NMAX,1
*vget , modval (( i_ -1)*NMAX+1,1) ,node ,1 ,u ,z ,0
*enddo

*cfopen ,wmodes
*if ,xywrite ,eq,1 ,then
*vwrite ,xycoord (1,1) ,xycoord (1,2) ,modval (1,1)
(1x,7E20.10)
*else
*vwrite ,modval (1,1)
(1x,7E20.10)
*endif
*cfclose ,wmodes
*cfopen ,wfreq
*vlen ,num_mod1,1
*vwrite ,freq (1,1)
(1x,7E20.10)
*cfclose ,wfreq
%!FINISH

```

## A.4 The aeroelastic code in MatLab™

The aeroelastic code written in MatLab is extensive. There are a number of sub-routines needed for the code included to work. The code included is the main file needed to calculate flutter.

```

% Determining the Eqns. of Motion using LaGranges Eq. for a V-g
% flutter analysis
% Structural Data coming from ANSYS.m, fitmodeshape.m, dflec.m
% Aerodynamic Data coming from DLM4d.m
clear all
close all
%% Structural Properties of Wing used in ANSYS
wrho = 1217; % density of wing in kg/m^3
MOE = 2.54e9; % Modulus of Elasticity in N/
% m^2
th = 0.001588; % thickness of wing in m

```

```

Ach      = 0.2032;           % Ansys chord length in "m"
      that is used to scale to aero mesh
MA       = wrho*th;         % mass/area of wing in kg/m^2
%% Building the Wing Geometry.
U        = 20;              % freestream velocity in m/s
alpha    = 1*pi/180;        % Angle of Attack in rads
rho      = 1.225;          % fluid density in kg/m^3
Mach     = U/340;          % Mach=0 to get the
      undeformed Wing
Beta     = (1-Mach^2)^(1/2);
ch       = 0.1524;         % Chord, x-direction(
      nondimensionalize by chord)
Sp       = 0.3048;         % actually Semi-Span, depends
      on geobackup.m
b        = ch/2;           % Semi Chord,
m        = 16;             % divisions in the chord, x-
      direction
n        = 16;             % divisions in the span, y-
      directio
LEang    = 0;              % 48.54*pi/180;    % LEang
      =48.54*pi/180;
TEang    = 0;              % TEang=34.50*pi/180; %
tiplen   = ch;            % tip length, tiplen=ch for
      rect. wing
LE       = Sp/cos(LEang) ; % Leading Edge
TE       = Sp/cos(TEang) ; % Trailing Edge
dypanel  = (Sp/n);
yvar     = [0];
Num      = m*n;           % Num of panels on semiwing
for a=1:n
      yvar=[yvar, (Sp/n*a) ]; % yvalue of panel division
end
yvar=sort(yvar);

%% Builds the Geometry for the wing w/o Prandtl Glaurent
      Transformation undeformed-used with Doublet Lattice
[ dxleft , dxright , Area ,XXv1,XXv2,YYv1,YYv2, len , lam , colXX , colYY ,TT,
  ARP,XXv1a,XXv1b,XXv1c,YYv1a,YYv1b,YYv1c] = geo4d(ch,1,yvar ,
  dypanel ,Sp,LEang,TEang,m,n,tiplen);
ARl=(Sp)^2/(sum(Area)); % Calculation of the Aspect Ratio
% Builds the Builds the Geometry for the wing wPrandtl Glaurent
      Transformation is undeformed-used with Vortex Lattice
[ pdxleft , pdxright , pArea ,pXXv1,pXXv2,pYYv1,pYYv2, plen , plam , pcolXX ,
  pcolYY ,TT,ARP,pXXv1a,pXXv1b,pXXv1c,pYYv1a,pYYv1b,pYYv1c] =
  geo4d(ch ,Beta , yvar , dypanel ,Sp,LEang,TEang,m,n,tiplen);

```

```

%% Using the modes/natural freq from ANSYS to determine the
   Structural
% deflection at at any x,y, z=f(x,y)
data1=load('-ascii','~/UNSTEADY/wfreq121807');           % Linux
data2=load('-ascii','~/UNSTEADY/wmodes121807');         % Linux
wn1=data1(3);                                           % 1st nat.
    freq. (htz)
wn2=data1(4);                                           % 2nd nat.
    freq. (htz)
wn3=data1(5);                                           % 3rd nat.
    freq. (htz)
wn4=data1(6);                                           % 4th nat.
    freq. (htz)
wn5=data1(7);                                           % 5th nat.
    freq. (htz)
wn6=data1(8);
wn7=data1(9);
wn8=data1(10);
wn9=data1(11);
wn10=data1(12);
nummod=data1(1,1);                                     % number of
    modes
gridpts=data1(2,1);                                    % number of
    finite elements for each mode
chek=nummod*gridpts;                                   % number of
    points in data 2
matman=nummod*3*2;                                     % use in
    matrix manipulation, 3 comes for x,y,z
%Separate the x,y,z for each mode
aa=1;  ab=2;  ac=3;
bb=1;                                                 % counter
AA=zeros(gridpts,matman);
for ii=1:nummod
    for jj=1:gridpts
        AA(jj,aa)=data2(bb,1);                         % x-coord
        AA(jj,ab)=data2(bb,2);                         % y-coord
        AA(jj,ac)=data2(bb,3);                         % z-coord
        bb=bb+1;
    end
    aa=aa+3;
    ab=ab+3;
    ac=ac+3;
end

```

```

% reorganizing the data into each mode
mode1=AA(:,1:3);    mode2=AA(:,4:6);    mode3=AA(:,7:9);
    mode4=AA(:,10:12);
mode5=AA(:,13:15); mode6=AA(:,16:18);    mode7=AA(:,19:21);
    mode8=AA(:,22:24);
mode9=AA(:,25:27); mode10=AA(:,28:30);

N_EXP=21;
[CFSM1]=fitmodeshape(gridpts,N_EXP,mode1(:,1),mode1(:,2),mode1
(:,3)); % mode 1 coefficients
[CFSM2]=fitmodeshape(gridpts,N_EXP,mode2(:,1),mode2(:,2),mode2
(:,3)); % mode 2 coefficients
[CFSM3]=fitmodeshape(gridpts,N_EXP,mode3(:,1),mode3(:,2),mode3
(:,3)); % mode 3 coeffficeints
[CFSM4]=fitmodeshape(gridpts,N_EXP,mode4(:,1),mode4(:,2),mode4
(:,3)); % mode 4 coefficients
[CFSM5]=fitmodeshape(gridpts,N_EXP,mode5(:,1),mode5(:,2),mode5
(:,3)); % mode 5 coefficients
[CFSM6]=fitmodeshape(gridpts,N_EXP,mode6(:,1),mode6(:,2),mode6
(:,3));
[CFSM7]=fitmodeshape(gridpts,N_EXP,mode7(:,1),mode7(:,2),mode7
(:,3));
[CFSM8]=fitmodeshape(gridpts,N_EXP,mode8(:,1),mode8(:,2),mode8
(:,3));
[CFSM9]=fitmodeshape(gridpts,N_EXP,mode9(:,1),mode9(:,2),mode9
(:,3));
[CFSM10]=fitmodeshape(gridpts,N_EXP,mode10(:,1),mode10(:,2),
mode10(:,3));

ac1=CFSM1;
ac2=CFSM2;
ac3=CFSM3;
ac4=CFSM4;
ac5=CFSM5;
ac6=CFSM6;
ac7=CFSM7;
ac8=CFSM8;
ac9=CFSM9;
ac10=CFSM10;

clear AA data2

M1=0; M2=0; M3=0; M4=0; M5=0; M6=0; M7=0; M8=0; M9=0; M10=0;
Q1=0; Q2=0; Q3=0; Q4=0; Q5=0; Q6=0; Q7=0; Q8=0; Q9=0; Q10=0;

```

```

%% Determine the generalized masses to input in the mass and
stiff. Matrices
for ii=1:TT
M1=M1+MA*( zdefl(N_EXP,ac1,colXX(ii),colYY(ii)))^2*Area(ii);
M2=M2+MA*( zdefl(N_EXP,ac2,colXX(ii),colYY(ii)))^2*Area(ii);
M3=M3+MA*( zdefl(N_EXP,ac3,colXX(ii),colYY(ii)))^2*Area(ii);
M4=M4+MA*( zdefl(N_EXP,ac4,colXX(ii),colYY(ii)))^2*Area(ii);
M5=M5+MA*( zdefl(N_EXP,ac5,colXX(ii),colYY(ii)))^2*Area(ii);
M6=M6+MA*( zdefl(N_EXP,ac6,colXX(ii),colYY(ii)))^2*Area(ii);
M7=M7+MA*( zdefl(N_EXP,ac7,colXX(ii),colYY(ii)))^2*Area(ii);
M8=M8+MA*( zdefl(N_EXP,ac8,colXX(ii),colYY(ii)))^2*Area(ii);
M9=M9+MA*( zdefl(N_EXP,ac9,colXX(ii),colYY(ii)))^2*Area(ii);
M10=M10+MA*( zdefl(N_EXP,ac10,colXX(ii),colYY(ii)))^2*Area(ii)
;
end

MM=[M1,0,0,0,0,0,0,0,0,0;...
0,M2,0,0,0,0,0,0,0,0;...
0,0,M3,0,0,0,0,0,0,0;...
0,0,0,M4,0,0,0,0,0,0;...
0,0,0,0,M5,0,0,0,0,0;...
0,0,0,0,0,M6,0,0,0,0;...
0,0,0,0,0,0,M7,0,0,0;...
0,0,0,0,0,0,0,M8,0,0;...
0,0,0,0,0,0,0,0,M9,0;...
0,0,0,0,0,0,0,0,0,M10];

KM=[(2*pi*wn1)^2*M1,0,0,0,0,0,0,0,0,0;...
0,(2*pi*wn2)^2*M2,0,0,0,0,0,0,0,0;...
0,0,(2*pi*wn3)^2*M3,0,0,0,0,0,0,0;...
0,0,0,(2*pi*wn4)^2*M4,0,0,0,0,0,0;...
0,0,0,0,(2*pi*wn5)^2*M5,0,0,0,0,0;...
0,0,0,0,0,(2*pi*wn6)^2*M6,0,0,0,0;...
0,0,0,0,0,0,(2*pi*wn7)^2*M7,0,0,0;...
0,0,0,0,0,0,0,(2*pi*wn8)^2*M8,0,0;...
0,0,0,0,0,0,0,0,(2*pi*wn9)^2*M9,0;...
0,0,0,0,0,0,0,0,0,(2*pi*wn10)^2*M10];

Kinv=inv(KM);

%% Calculating the Geometric properties that independent of the
freq for time reasons
xoi=zeros(TT); xom=zeros(TT); xoo=zeros(TT); yoi=zeros(TT); yom=
zeros(TT); yoo=zeros(TT); r1i=zeros(TT); r1m=zeros(TT); r1o=
zeros(TT);
R1i=zeros(TT); R1m=zeros(TT); R1o=zeros(TT); u1i=zeros(TT); u1m=
zeros(TT); u1o=zeros(TT);

```

```

xoa=zeros(TT);xob=zeros(TT); xoc=zeros(TT);
yoa=zeros(TT);yob=zeros(TT); yoc=zeros(TT);
r1a=zeros(TT);r1b=zeros(TT); r1c=zeros(TT);
R1a=zeros(TT);R1b=zeros(TT); R1c=zeros(TT);
ula=zeros(TT);ulb=zeros(TT); ulc=zeros(TT);

for mm=1:TT
    for nn=1:TT
        %% Step 1: calculate xo,yo, r1
        xoi(mm,nn)=colXX(mm)-XXv1(nn); % xo-
            inner
        xoa(mm,nn)=colXX(mm)-XXv1a(nn);
        xom(mm,nn)=colXX(mm)-((XXv1(nn)+XXv2(nn))/2); % xo-
            midhadle
        xob(mm,nn)=colXX(mm)-XXv1b(nn);
        xoc(mm,nn)=colXX(mm)-XXv1c(nn);
        xoo(mm,nn)=colXX(mm)-XXv2(nn); % xo-
            outer

        yoi(mm,nn)=colYY(mm)-YYv1(nn); % yo-
            inner
        yoa(mm,nn)=colYY(mm)-YYv1a(nn);
        yom(mm,nn)=colYY(mm)-colYY(nn); %((
            YYv1(nn)+YYv2(nn))/2); % yo-middle
        yob(mm,nn)=colYY(mm)-YYv1b(nn);
        yoc(mm,nn)=colYY(mm)-YYv1c(nn);
        yoo(mm,nn)=colYY(mm)-YYv2(nn); % yo-
            outer

        r1i(mm,nn)=abs(yoi(mm,nn)); % r1-
            inter
        r1a(mm,nn)=abs(yoa(mm,nn));
        r1m(mm,nn)=abs(yom(mm,nn)); % rl-
            middle
        r1b(mm,nn)=abs(yob(mm,nn));
        r1c(mm,nn)=abs(yoc(mm,nn));
        r1o(mm,nn)=abs(yoo(mm,nn)); % rl-
            outer

        %% Step 2: calculate u1, R1
        R1i(mm,nn)=sqrt((xoi(mm,nn))^2+Beta^2*(r1i(mm,nn))^2)
        ;
        R1a(mm,nn)=sqrt((xoa(mm,nn))^2+Beta^2*(r1a(mm,nn))^2)
        ;
    end
end

```

```

R1m(mm, nn)=sqrt (( xom(mm, nn) ) ^2+Beta ^2*( r1m(mm, nn) ) ^2)
;
R1b(mm, nn)=sqrt (( xob(mm, nn) ) ^2+Beta ^2*( r1b(mm, nn) ) ^2)
;
R1c(mm, nn)=sqrt (( xoc(mm, nn) ) ^2+Beta ^2*( r1c(mm, nn) ) ^2)
;
R1o(mm, nn)=sqrt (( xoo(mm, nn) ) ^2+Beta ^2*( r1o(mm, nn) ) ^2)
;
u1i(mm, nn)=U1a( xoi(mm, nn) , r1i(mm, nn) ,Mach , R1i(mm, nn) ,
Beta );
u1a(mm, nn)=U1a( xoa(mm, nn) , r1a(mm, nn) ,Mach , R1a(mm, nn) ,
Beta );
u1m(mm, nn)=U1a( xom(mm, nn) , r1m(mm, nn) ,Mach , R1m(mm, nn) ,
Beta );
u1b(mm, nn)=U1a( xob(mm, nn) , r1b(mm, nn) ,Mach , R1b(mm, nn) ,
Beta );
u1c(mm, nn)=U1a( xoc(mm, nn) , r1c(mm, nn) ,Mach , R1c(mm, nn) ,
Beta );
u1o(mm, nn)=U1a( xoo(mm, nn) , r1o(mm, nn) ,Mach , R1o(mm, nn) ,
Beta );

end
end

%% —— Declaration of code of what cells to place the hole in
for damage
msta=89; % 1st cell on right half of wing
where hole appears
choleR=[]; % array to declare for cell
for ii=1:6 % # of rows in x-dir to delete cells
for jj=1:5 % # of columns in y dir to delete
cels
choleR=[choleR ; msta ];
msta=msta+1;
end
msta=msta+(16-5); % how to jump to the next row
end
choleL=choleR+256; % hole deletion on the left (image)
side
chole=[choleR ;choleL ]; % entire cell deletion for model

%% Calculating the Aerodynamic Influence Coefficient Matrix using
the
%% quartic Doublet Lattice

```

```

freq=[ ]; ftdata1=[]; ftdata2=[];
  for k=.01:.10:2.51% 5.57           % looping over
      nondimensional freq., k
%for k=.1850:0.025:.1851
%k = 0.10; %k =0 for steady flow
    w = k*U/b;
    freq= [freq , w];
    DI = zeros(TT);
    Drs = zeros(TT);

    for mm=1:TT
        for nn=1:TT
            %% Step 3, 4, 5: calculates I1,K, Ktilda
            % Step 3 is handled by the function file IUK
            % Step 4 is the calculation K which is handled
            % intinsically in
            % calculating Ktilda in Step 5
            k1i=w*r1i(mm,nn)/U;      % reduced frequency-inner
            k1a=w*r1a(mm,nn)/U;
            k1m=w*r1m(mm,nn)/U;      % reduced frequency-middle
            k1b=w*r1b(mm,nn)/U;
            k1c=w*r1c(mm,nn)/U;
            k1o=w*r1o(mm,nn)/U;      % reduced frequency-outer
            % Ktilda using the approximation
            Ktilda_i=ktilda(w,xoi(mm,nn),yoi(mm,nn),U,k1i,Mach);
            Ktilda_a=ktilda(w,xoa(mm,nn),yoa(mm,nn),U,k1a,Mach);
            Ktilda_m=ktilda(w,xom(mm,nn),yom(mm,nn),U,k1m,Mach);
            Ktilda_b=ktilda(w,xob(mm,nn),yob(mm,nn),U,k1b,Mach);
            Ktilda_c=ktilda(w,xoc(mm,nn),yoc(mm,nn),U,k1c,Mach);
            Ktilda_o=ktilda(w,xoo(mm,nn),yoo(mm,nn),U,k1o,Mach);%
            - ...
            %0*ktilda(0,xoo(mm,nn),yoo(mm,nn),U,0,Mach);

            %% Step 6: Calculates A,B,C
            e=(1/2)*len(nn)*cos(lam(nn));
            A=(Ktilda_i-2*Ktilda_m+Ktilda_o)/(2*e^2);
            B=(Ktilda_o-Ktilda_i)/(2*e);
            C=Ktilda_m;
            A1=-(1/(6*e^2))*(Ktilda_i-16*Ktilda_a+30*Ktilda_b-16*
                Ktilda_c+Ktilda_o);
            B1=(1/(6*e))*(Ktilda_i-8*Ktilda_a+8*Ktilda_c-Ktilda_o
                );
            C1=Ktilda_b;
            D1=-(2/(3*e^3))*(Ktilda_i-2*Ktilda_a+2*Ktilda_c-
                Ktilda_o);

```

```

E1=(2/(3*e^4))*(Ktilda_i-4*Ktilda_a+6*Ktilda_b-4*
    Ktilda_c+Ktilda_o);

%%Step 7: Calculate I_ij requires calculating eta and
    zeta
eta=colYY(mm)-((YYv1(nn)+YYv2(nn))/2);% is eta sub
    knot in paper
zeta=0; % zeta =0 since gamma(s) =0, and the sin(0)
    =0 for the planar case
I_ij=IIJ(A,B,C,e,eta); % IIJ is a function file
dx=(dxright(nn)+dxleft(nn))/2;

%% The next lined is where I apply the infamous
    TRICKha
DI(mm,nn)=(1/(pi*8))*I_ij*dx;
F=(1/(yob(mm,nn)-e)-1/(yob(mm,nn)+e)); % eqn 32,
    Rodden 1972
D1rs=(dx/(8*pi))*(((yob(mm,nn))^2*A1+yob(mm,nn)*B1+C1
    +(yob(mm,nn))^3*D1+...
    (yob(mm,nn))^4*E1)*F+(yob(mm,nn)*A1+0.5*B1
    +0.5*(3*(yob(mm,nn))^2*D1)+2*(yob(mm,nn))^3*E1
    )*log((yob(mm,nn)-e)^2/(yob(mm,nn)+e)^2)+...
    2*e*(A1+2*yob(mm,nn)*D1+(3*(yob(mm,nn))^2+(1/3)*e
    ^2)*E1));
Drs(mm,nn)=D1rs;

    end
end
%end % looping over nondimensional freq., k

%Allocating memory for wing deflection
def1=zeros(TT,1); def2=zeros(TT,1); def3=zeros(TT,1); def4=zeros(
    TT,1); def5=zeros(TT,1);
def6=zeros(TT,1); def7=zeros(TT,1); def8=zeros(TT,1); def9=zeros(
    TT,1); def10=zeros(TT,1);
%dxx1=zeros(TT,1); dxx2=zeros(TT,1); dxx3=zeros(TT,1); dxx4=zeros(
    TT,1); dxx5=zeros(TT,1);
dw1=zeros(TT,1); dw2=zeros(TT,1); dw3=zeros(TT,1); dw4=zeros(TT
    ,1); dw5=zeros(TT,1);
dw6=zeros(TT,1); dw7=zeros(TT,1); dw8=zeros(TT,1); dw9=zeros(TT
    ,1); dw10=zeros(TT,1);

for ii=1:TT % deflections & down wash in each mode
    def1(ii)=zdefl(N_EXP,ac1,colXX(ii),colYY(ii));
    def2(ii)=zdefl(N_EXP,ac2,colXX(ii),colYY(ii));

```

```

def3(ii)=zdefl(N_EXP,ac3,colXX(ii),colYY(ii));
def4(ii)=zdefl(N_EXP,ac4,colXX(ii),colYY(ii));
def5(ii)=zdefl(N_EXP,ac5,colXX(ii),colYY(ii));
def6(ii)=zdefl(N_EXP,ac6,colXX(ii),colYY(ii));
def7(ii)=zdefl(N_EXP,ac7,colXX(ii),colYY(ii));
def8(ii)=zdefl(N_EXP,ac8,colXX(ii),colYY(ii));
def9(ii)=zdefl(N_EXP,ac9,colXX(ii),colYY(ii));
def10(ii)=zdefl(N_EXP,ac10,colXX(ii),colYY(ii));

gustc=-1.0;      % To turn on gust, gustc=1.0 and to turn off
                 % gust, gustc=0
wg1=10;         % Frequency of gust in htz
wg2=2*wg1;      % frequency of gust in htz
dwgust(ii)=gustc*(1.61*(pi/180)*exp(-1i*wg1*2*pi*((colXX(ii)-
b)/b)/U)-0.2*(pi/180)*exp(-1i*wg2*2*pi*((colXX(ii)-b)/b)/U
));

% Incorporated the effect of gust response
dw1(ii)=1i*w/U*zdefl(N_EXP,ac1,colXX(ii),colYY(ii))+dzdx1(
N_EXP,ac1,colXX(ii),colYY(ii))+...
dwgust(ii);
dw2(ii)=1i*w/U*zdefl(N_EXP,ac2,colXX(ii),colYY(ii))+dzdx1(
N_EXP,ac2,colXX(ii),colYY(ii))+...
dwgust(ii);
dw3(ii)=1i*w/U*zdefl(N_EXP,ac3,colXX(ii),colYY(ii))+dzdx1(
N_EXP,ac3,colXX(ii),colYY(ii))+...
dwgust(ii);
dw4(ii)=1i*w/U*zdefl(N_EXP,ac4,colXX(ii),colYY(ii))+dzdx1(
N_EXP,ac4,colXX(ii),colYY(ii))+...
dwgust(ii);
dw5(ii)=1i*w/U*zdefl(N_EXP,ac5,colXX(ii),colYY(ii))+dzdx1(
N_EXP,ac5,colXX(ii),colYY(ii))+...
dwgust(ii);
dw6(ii)=1i*w/U*zdefl(N_EXP,ac6,colXX(ii),colYY(ii))+dzdx1(
N_EXP,ac6,colXX(ii),colYY(ii))+...
dwgust(ii);
dw7(ii)=1i*w/U*zdefl(N_EXP,ac7,colXX(ii),colYY(ii))+dzdx1(
N_EXP,ac7,colXX(ii),colYY(ii))+...
dwgust(ii);
dw8(ii)=1i*w/U*zdefl(N_EXP,ac8,colXX(ii),colYY(ii))+dzdx1(
N_EXP,ac8,colXX(ii),colYY(ii))+...
dwgust(ii);
dw9(ii)=1i*w/U*zdefl(N_EXP,ac9,colXX(ii),colYY(ii))+dzdx1(
N_EXP,ac9,colXX(ii),colYY(ii))+...

```

```

        dwgust(ii);
        dw10(ii)=1i*w/U*zdefl(N_EXP,ac10,colXX(ii),colYY(ii))+dzdx1(
            N_EXP,ac10,colXX(ii),colYY(ii))+...
        dwgust(ii);
end

for aa=1:length(chole)
    que=chole(aa);
    Drs(que,:)=0;
    Drs(que,que)=1;
    dw1(que)=0;
    dw2(que)=0;
    dw3(que)=0;
    dw4(que)=0;
    dw5(que)=0;
    dw6(que)=0;
    dw7(que)=0;
    dw8(que)=0;
    dw9(que)=0;
    dw10(que)=0;
end

Cp1=2*0.5*Drs\dw1; %Coefficient of
    pressure due to downwash generated in mode 1
Cp2=2*0.5*Drs\dw2; %Coefficient of
    pressure due to downwash generated in mode 2
Cp3=2*0.5*Drs\dw3; %Coefficient of
    pressure due to downwash generated in mode 3
Cp4=2*0.5*Drs\dw4; %Coefficient of
    pressure due to downwash generated in mode 4
Cp5=2*0.5*Drs\dw5; %Coefficient of
    pressure due to downwash generated in mode 5
Cp6=2*0.5*Drs\dw6;
Cp7=2*0.5*Drs\dw7;
Cp8=2*0.5*Drs\dw8;
Cp9=2*0.5*Drs\dw9;
Cp10=2*0.5*Drs\dw10;
tdefl=[def1,def2,def3,def4,def5,def6,def7,def8,def9,def10];
    %place all deflection in matrix for computing
    generalized forces
ptotal=[Cp1,Cp2,Cp3,Cp4,Cp5,Cp6,Cp7,Cp8,Cp9,Cp10]; %
    place all pressures in matrix for computing generalized forces
% Generalized Forces
Qij=zeros(10,10);
for ii=1:10

```

```

    for jj=1:10
        for bb=1:TT
            Qij(ii,jj)=Qij(ii,jj)+tdefl(bb,ii)*ptotal(bb,jj)*Area
                (bb);
        end
    end
end

% return
%% putting the Equations of Motion in generalized eigenvalue
form
const=((1/2)*rho*b^2);
lamb=eig(Kinv*(MM+(const/k^2)*Qij));
[EVR,EVE]=eig(Kinv*(MM+(const/k^2)*Qij));           % EVR-
    EigenVectoR , EVE-EigenValuE
V1=1/sqrt(abs(real(lamb(1))));                       % omega for
    first mode
V2=1/sqrt(abs(real(lamb(2))));
V3=1/sqrt(abs(real(lamb(3))));
V4=1/sqrt(abs(real(lamb(4))));
V5=1/sqrt(abs(real(lamb(5))));
V6=1/sqrt(abs(real(lamb(6))));
V7=1/sqrt(abs(real(lamb(7))));
V8=1/sqrt(abs(real(lamb(8))));
V9=1/sqrt(abs(real(lamb(9))));
V10=1/sqrt(abs(real(lamb(10))));
g1=imag(lamb(1))/real(lamb(1));                      % damping for
    first mode
g2=imag(lamb(2))/real(lamb(2));
g3=imag(lamb(3))/real(lamb(3));
g4=imag(lamb(4))/real(lamb(4));
g5=imag(lamb(5))/real(lamb(5));
g6=imag(lamb(6))/real(lamb(6));
g7=imag(lamb(7))/real(lamb(7));
g8=imag(lamb(8))/real(lamb(8));
g9=imag(lamb(9))/real(lamb(9));
g10=imag(lamb(10))/real(lamb(10));
U1=V1*b/k;                                           % Velocity
U2=V2*b/k;
U3=V3*b/k;
U4=V4*b/k;
U5=V5*b/k;
U6=V6*b/k;
U7=V7*b/k;
U8=V8*b/k;

```

```

U9=V9*b/k;
U10=V10*b/k;
ftdata1=[ftdata1;k,V1,V2,V3,V4,V5,g1,g2,g3,g4,g5,U1,U2,U3,U4,U5];
ftdata2=[ftdata2;k,V6,V7,V8,V9,V10,g6,g7,g8,g9,g10,U6,U7,U8,U9,
U10];
% AA=MM#const*(1/2)*Qij;
% BB=KM;
% [VV,DD]=eig(AA,BB); % VV is a matrix of
% eigenvalues along diag, DD matrix of eigenvector
% lambda=diag(VV); % retrieving the
% eigenvalues
% omega2=1./real(lambda); % frequency^2
% determine froming find the eigenvalues of the generalized
% system
% gg=1*imag(lambda)./real(lambda); % ficticious damping
% that is due to the V-g method
% UF=sqrt(omega2)*b/k; % Flutter Speed but b
% may be need to be dimensionlize
% walpha=wn2; % 1st Torsional
% frequency, that will be used to normalized UF/(walpha*b)
%ftdata=[ftdata;k,real(lambda)',imag(lambda)',omega2',gg',UF',
wn2];
%ftdata=[ftdata;k,omega2',gg',UF',wn2];

end
% Saving the results in a data file incase I need to view the
aeroelastic
%save temp.txt A -ascii

```

# Bibliography

- [1] E. H. Dowell, R. Clark, D. Cox, H. C. Curtiss Jr., J. W. Edwards, K. C. Hall, D. A. Peters, R. Scanlan, E. Simiu, F. Sisto, and T. W. Strganac. *A Modern Course in Aeroelasticity*. Solid Mechanics and its Applications. Kluwer Academic Publishers, Dordrecht, The Netherlands, fourth edition, 2004.
- [2] R. L. Bisplinghoff, H. Ashley, and R. L. Halfman. *Aeroelasticity*. Dover Publications, Inc., New York, first edition, 1996.
- [3] M. Kim, M. Vahdati, and M. Imregun. Aeroelastic stability analysis of bird-damaged aeroengine fan assembly. *Aerospace Science and Technology*, 5(7):469–482, 2001.
- [4] M.S. Kruger, C.W. Endruhn, and R.O Stearman. A New Look at Galloping. AIAA Paper 2005-2178, 2005.
- [5] P.J. Attar, E. H. Dowell, and J.R. White. Modeling the LCO of a Delta Wing Using a High Fidelity Structural Model. *Journal of Aircraft*, 45(2):1209–1217, September–October 2005.
- [6] D.M. Tang, J.K. Henry, and E.H. Dowell. Limit-Cycle Oscillations of Delta Wing Models in Low Subsonic Flow. *AIAA Journal*, 37(11):1355–1362, November 1999.
- [7] D.M. Tang, P.J. Attar, and E.H. Dowell. Flutter/LCO Analysis and Experiment for Wing-Store Model. *AIAA Journal*, 44(7):1662–1675, 2006.
- [8] D.M. Tang and E.H. Dowell. Flutter and Limit Cycle Oscillations for a Wing-Store Model with Freeplay. *Journal of Aircraft*, 43:487–603, March–April 2006.
- [9] E. Albano and W.P. Rodden. A Doublet-Lattice Method for Calculating Lift Distributions on Oscillating Surfaces in Subsonic Flows. *AIAA Journal*, 7(2):279–285, February 1969.

- [10] D.M. Tang, E.H. Dowell, and K.C. Hall. Limit Cycle Oscillations of a Cantilevered Wing in Low Subsonic Flow. *AIAA Journal*, 37(3):364–371, March 1999.
- [11] D.M. Tang and E.H. Dowell. Experimental/Theoretical Correlation Study of Gust Response for a Wing-Store Model with Freeplay. *Journal of Sound and Vibration*, 295(3-5):659–684, 2006.
- [12] D.M. Tang and E.H. Dowell. Flutter and Limit-Cycle Oscillations for a Wing-Store Model with Freeplay. *Journal of Aircraft*, 43(2):387–503, 2006.
- [13] R.E. Gordnier. Computation of Limit-Cycle Oscillations of a Delta Wing. *Journal of Aircraft*, pages 1206–1208, November-December 2003.
- [14] C.M. Denegri Jr. Limit Cycle Oscillation Flight Test Results of a Fighter with External Stores. *Journal of Aircraft*, 37(5):761–769, September–October 2000.
- [15] R.W. Bunton and C.M. Denegri Jr. Limit Cycle Oscillation Characteristics of Fighter Aircraft. *Journal of Aircraft*, 37(5):916–918, September–October 2000.
- [16] C.M. Denegri Jr., J.A. Dubben, and D.L. Maxwell. In-Flight Wing Deformation Characteristics During Limit-Cycle Oscillations. *Journal of Aircraft*, 42(2):500–508, March–April 2005.
- [17] C.M. Denegri Jr. and M.R. Johnson. Limit Cycle Oscillation Prediction Using Artificial Neural Networks. *Journal of Guidance, Control, and Dynamics*, 24(5):887–895, September–October 2001.
- [18] M.R. Johnson and C.M. Denegri Jr. Comparison of Static and Dynamic Neural Networks for Limit Cycle Oscillation Prediction. *Journal of Aircraft*, 40(1):194–203, January–February 2003.
- [19] A.W. Leissa. Vibration of Plates. NASA Technical Report SP-160, 1969.
- [20] M. A. Biot and L. Arnold. Study of Vulnerability of Aircraft to Damage Induced Flutter. Ballistic Research Laboratories 743, October 1950.
- [21] G. Chen and R.O. Stearman. A Damage Induced Aeroelastic Failure Mode Involving Combination and Parametric Resonant Instabilities of Lifting Surfaces. In *A Collection of Technical Papers Part 2: Structural Dynamics and Design Engineering*, AIAA/ASME/ASCE/AHS 23rd Structures, Structural Dynamics and Material Conference, May 1982.

- [22] D. S. Scott. Potential Flow Modeling of A Through-Hole Type Damage in a Lifting Surface Utilizing A Kernel Function Procedure. Master's thesis, The University of Texas at Austin, May 1979.
- [23] R.O. Stearman and J.H. Chang. The Effects of Warhead-Induced Damage on the Aeroelastic Characteristics of Lifting Surfaces. AFOSR TR-80-1039, July 1980.
- [24] M.L. Stearman. Wind-tunnel Studies of the Effects of Simulated Damage on the Aerodynamics Characteristics of Airplanes and Missiles. NASA TM-84588, December 1982.
- [25] L.P. Erm. Survey on the Aerodynamics of Battle-Damaged Combat Aircraft. DSTO Aeronautical and Maritime Research Laboratory DSTO-GD-0184, June 1998.
- [26] K.W. Robinson and J.G. Leishman. Effects of Ballistic Damage on the Aerodynamics of Helicopter Rotor Airfoils. *Journal of Aircraft*, 35(5):695–703, 1998.
- [27] P.M. Render, S. De Silva, A. Walton, and M. Mani. Experimental Investigation into the Aerodynamics of Battle Damaged Airfoils. *Journal of Aircraft*, 44(2):539–549, 2007.
- [28] K.H. Wang and D.J. Inman. Crack-induced Effects on Aeroelasticity of an Unswept Composite Wing. *AIAA Journal*, 45(3):542–551, 2007.
- [29] E. Albano and W.P. Rodden. A Doublet-Lattice Method for Calculating Lift Distributions on Oscillating Surfaces in Subsonic Flows. *AIAA Journal*, 7(2):279–284, February 1969.
- [30] M. Blair. A Compilation of the Mathematics Leading to the Doublet-Lattice Method. Wright Laboratory TR-95-3022, November 1994.
- [31] R.D. Cook, D.S. Malkus, and M.E. Plesha. *Concepts and Applications of Finite Element Analysis*. John Wiley and Sons, New York, third edition, 1989.
- [32] A.C. Ugural. *Stresses in Plates and Shell*. McGraw Hill Companies, Inc., Boston, second edition, 1999.
- [33] Swanson Analysis Systems Inc. ANSYS User Manual, release 6.1, 2002.
- [34] L. Meirovitch. *Principles and Techniques of Vibrations*. Prentice Hall, New Jersey, first edition, 1997.

- [35] Bruel & Kjaer. System Data: IDA Hardware Configurations for PULSE X, March 26, 2006. Available at [www.bksv.com/pdf/Bu0228.pdf](http://www.bksv.com/pdf/Bu0228.pdf).
- [36] H.J. Conyers. Experimental Study of Flutter of Cropped Delta Wing, 2006.
- [37] D.A. Anderson, J.C. Tannehill, and R.H. Pletcher. *Computational Fluid Mechanics and Heat Transfer*. Series in Computational Methods in Mechanics and Thermal Sciences. Hemisphere Publishing Corporation, first edition, 1984.
- [38] J. Katz and A. Plotkin. *Low Speed Aerodynamics*. Cambridge University Press, New York, second edition, 2001.
- [39] W.P. Rodden, J.P. Giesing, and T.P. Kalman. Refinement of the Nonplanar Aspects of the Subsonic Doublet-Lattice Lifting Surface Method. *Journal of Aircraft*, 9(1):69–73, January 1972.
- [40] W.P. Rodden, P.F. Taylor, and S.C. McIntosh Jr. Further Refinement of the Subsonic Doublet-Lattice Method. *Journal of Aircraft*, 35(5):720–727, September-October 1998.
- [41] M.T. Landahl. Kernel Function for Nonplanar Oscillating Surfaces in a Subsonic Flow. *AIAA Journal*, 5(5):1045–1046, May 1967.
- [42] M. Abramowitz and L.A. Stegun. *Handbook of Mathematical Functions*. National Bureau of Standards Applied Mathematics, seventh edition, 1968.
- [43] S.G. Hedman. Vortex Lattice Method for Calculation of Quasi Steady Loadings on Thin Elastic Wings. British Aeronautical Research Council 105, October 1965.
- [44] H.C. Garner, E.W.E. Rogers, W.E.A. Acum, and E.C. Maskell. Subsonic Wind Tunnel Wall Corrections. Advisory Group for Aerospace Research and Development(AGARD) 109, October 1966.
- [45] E.H. Dowell. *Aeroelasticity of Plates and Shells*. NOORDHOFF INTERNATIONAL PUBLISHING, Leyden, 1975.
- [46] D.M. Tang, P.G.A. Cizmas, and E.H. Dowell. Experiments and analysis for a gust generator in a wind tunnel model. *Journal of Aircraft*, 33(1):139–148, 1996.
- [47] D.E. Raveh. A Numerical Study of an Oscillating Airfoil in Transonic Flows with Large Shock Waves Oscillations. *Journal of Aircraft*, Submitted for 2008.

- [48] H. Schlichting. *Boundary-Layer Theory*. McGraw-Hill Book Company, sixth edition, 1968.
- [49] D. Poirel, Y. Harris, and A. Benaissa. Self-Sustained Aeroelastic Oscillations of a NACA 0012 Airfoil at Low-to-Moderate Reynolds Numbers. *Journal of Fluids and Structures*, 24(1):700–719, 2008.
- [50] P.C. Chen, D. Sarhaddi, and D.D. Liu. Limit Cycle-Oscillations Studies of a Fighter with External Stores. *AIAA*, page 1727, April 1998.
- [51] J.C. Rowan and T.A. Burns. Aeroelastic Loads Predictions using Finite Element Aerodynamics. *Journal of Aircraft*, 12(11):890–898, 1975.
- [52] R.L. Harder and R.N. Desmarais. Interpolation Using Surface Splines. *Journal of Aircraft*, 9:189–191, 1972.
- [53] C.R. Rao and H. and Toutenburg. *Linear Models: Least Squares and Alternatives*. Springer Series in Statistics. Springer, second edition, 1999.
- [54] T. Kim, R.O. Stearman, and E.J. Powers. Non-Classical Flow-Induced Responses of a Lifting Surface Due to Localized Disturbances. 6th International Modal Analysis Conference, February 1988.
- [55] E. H. Dowell. Private communication. July 2005.
- [56] R.O Stearman and et. al. The Influence of Ballastic Damage on the Aeroelastic Characteristics of Lifting Surfaces. AFOSR TR-80-0220, May 1979.
- [57] H.J. Conyers. Effect of Wing Damage on Aeroelastic Behavior, 2007. Preliminary Examination.
- [58] Bruel & Kjaer PULSE User’s Manual: Getting Started, September 2003.

# Biography

I was born in Sumter, SC on December 1, 1981 to Harrison and Hallie Conyers. I have an older brother, Harrison Jr. I was raised in Manning, SC where I attended Manning High School. In 2000, I was awarded the USDA/1890 National Scholarship to attend North Carolina Agricultural and Technical State University in Greensboro, NC.

While at North Carolina A& T, I was initiated into Tau Beta Pi Engineering Honors Society, Phi Kappa Phi Honors Society, and Alpha Phi Alpha Fraternity, Inc. I received a Bachelor of Science in Bioenvironmental Engineering in May 2004 from North Carolina Agricultural and Technical State University. In addition, I was awarded the NC A&TSU College of Engineering NAMASKAR Award. It is awarded annually to a member of the graduating class who displays exceptional academics, leadership, and community service.

Immediately upon graduation, I entered the Mechanical Engineering and Material Science(MEMS) Program at Duke University in the Fall of 2004. I received my Masters of Science in MEMS at Duke University in September 2006. In 2006, I won the North Carolina Space Grant Graduate Research Fellowship and I was recognized as Honorable Mention for the 2006 NSF Graduate Research Fellowship.